

UNIVERSIDADE DE SÃO PAULO  
ESCOLA POLITÉCNICA

**GUIDO BOIDI**

**An experimental assessment of surface micro irregularities (porosity and texture) effects on tribological behaviour under lubricated conditions**

São Paulo  
2019

GUIDO BOLDI

**An experimental assessment of surface micro irregularities (porosity and texture) effects on tribological behaviour under lubricated conditions**

Thesis submitted to the University of São Paulo for the Degree of Doctor of Science

Area:

Design and Manufacture - Mechanical Engineering

Supervisor:

Prof. Dr. Izabel Fernanda Machado

São Paulo

2019

Autorizo a reprodução e divulgação total ou parcial deste trabalho, por qualquer meio convencional ou eletrônico, para fins de estudo e pesquisa, desde que citada a fonte.

Este exemplar foi revisado e corrigido em relação à versão original, sob responsabilidade única do autor e com a anuência de seu orientador.

São Paulo, \_\_\_\_\_ de \_\_\_\_\_ de \_\_\_\_\_

Assinatura do autor:

Guido Boidi

Assinatura do orientador:

Isabel Ferreira Tralada

#### Catálogo-na-publicação

Boidi, Guido

An experimental assessment of surface micro irregularities (porosity and texture) effects on tribological behaviour under lubricated conditions / G. Boidi - versão corr. - São Paulo, 2019.

118 p.

Tese (Doutorado) - Escola Politécnica da Universidade de São Paulo. Departamento de Engenharia Mecânica.

1. Tribologia 2. Sinterização 3. Porosidade 4. Textura Superficial 5. Relação deslizamento-rolamento I. Universidade de São Paulo. Escola Politécnica. Departamento de Engenharia Mecânica II. t.

## ABSTRACT

Energy saving, improving system efficiency and using alternative energy sources are common strategies adopted nowadays for reducing human detrimental impact on environment. In particular, tribologists strive to reduce friction in rubbing parts using coatings, advanced lubricants or modifying surface topography. In this context surface texture has been significantly studied in recent years, although this procedure usually implies extra manufacturing operations and costs. On the other hand, sintered materials contain themselves surface cavities that could potentially act as surface texture and, consequently, lead to friction reduction. This research aims to extend the current knowledge on the tribological influence of micro surface irregularities (pores and laser texture) under lubricated experimental tests and explore the use of these features for tribological applications. Samples were manufactured using both sintering and texturing processes to obtain different surface characteristics. Three different porosity conditions were produced for sintered steels, whereas grooves and dimples configurations were designed for textured steel samples. After that, experimental tests were performed under varying sliding-rolling conditions (from prevalent rolling to prevalent sliding) especially using non-conformal contact. Speed was also varied during frictional tests to cover a wide range of operational conditions and verify the effects of surface features under different lubrication regimes. Friction tests were carried out with two tribometers using configurations of pin-on-disk, roller-on-disk and ball-on-disk. Film thickness was measured by an ultra-thin optical interferometry rig using a methodology properly designed for rough samples. Samples with smooth surfaces were utilized as a reference bench to be compared to material with surface modification (texture or porosity). Main results showed that the decrease of porosity led to friction reduction in the sintered steel. Material with reduced porosity performed even better than reference smooth samples. In addition, the dimple configuration promoted friction reduction, whereas grooves generally performed similarly or worse than reference material. Even if textured dimples and small porosity on sintered material were produced by different techniques, they presented similar geometrical characteristics and consequently they both reduced friction compared to reference samples. As part of the outcome, main results were mapped to better understand the effect of each surface feature on tribological performance. Furthermore, a preliminary phenomenological model was proposed to predict frictional response of surface with micro cavities (pores or texture) from reference steel results. Main findings suggest that the effect of tailored surface cavities could be somehow compared to randomly distributed ones, even if produced by very different manufacturing techniques.

**Keywords:** Tribology. Sintering. Porosity. Surface texture. Slide-to-roll ratio.

## RESUMO

Os impactos negativos no meio ambiente causados pelo ser humano são atualmente mitigados por políticas de redução de energia, aumento de eficiência e utilização de fontes de energias alternativas. Os tribologistas visam reduzir o atrito entre componentes em movimento utilizando recobrimentos de elevada dureza, óleos aditivados ou modificando a topografia dos materiais. Nesse contexto, a textura superficial pode possibilitar redução de atrito em determinadas condições, mas esse processo exige operações de manufatura e custos adicionais. Por outro lado, os materiais sinterizados apresentam porosidade superficial após o processo de manufatura, que poderia atuar como textura superficial e conseqüentemente levar à redução do atrito. Com base nisso, esta pesquisa visa ampliar o conhecimento atual sobre a influência tribológica das micro irregularidades superficiais (porosidade e textura) em testes experimentais lubrificados e explorar o uso de superfícies não-isotrópicas para aplicações tribológicas. As amostras foram produzidas usando tanto a sinterização como a texturização laser para obter cavidades superficiais com diferentes características. Três diferentes condições de porosidade foram estudadas em aço sinterizado, enquanto configurações de bolsos circulares e canais foram texturizadas em amostras de aço cromo. Em seguida, testes experimentais foram realizados variando as condições de deslizamento-rolamento (de rolamento predominante para deslizamento predominante), especialmente usando contato não-conforme. Diferentes velocidades foram utilizadas durante os testes tribológicos para cobrir uma ampla gama de condições operacionais e estudar os efeitos das irregularidades superficiais em diferentes regimes de lubrificação. Os testes para avaliação do coeficiente de atrito foram realizados utilizando dois tribômetros usando as configurações de pino-disco, rotula-disco e esfera-disco. A espessura de filme foi medida utilizando um equipamento de interferometria óptica usando uma metodologia direcionada para amostras com rugosidade superficial elevada. Amostras com superfícies polidas foram utilizadas como material de referência para comparação com amostras contendo alterações superficiais (textura ou porosidade). Os principais resultados mostraram que a diminuição da porosidade levou a redução de atrito em aço sinterizado. As amostras com porosidade reduzida apresentaram melhores desempenhos que o material de referência (não-poroso). Além disso, a configuração de bolsos circulares promoveu redução de atrito, enquanto os canais tiveram um desempenho semelhante ou pior que o material de referência. Embora os bolsos texturizados e os poros de dimensões reduzidas no material sinterizado foram produzidos com diferentes técnicas de manufatura, eles apresentaram características geométricas similares e, conseqüentemente, levaram a redução de coeficiente de atrito em comparação com as amostras de referência. Os principais resultados foram mapeados para melhor entender o efeito de cada micro irregularidade superficial no desempenho tribológico. Além disso, um modelo fenomenológico preliminar foi proposto para prever a resposta em termos de coeficiente de atrito das superfícies com micro cavidades (porosidade ou textura)

com base nos resultados do aço de referência. Os principais resultados sugerem que o efeito das cavidades superficiais projetadas (textura) e daquelas distribuídas aleatoriamente (porosidade) podem ser de alguma forma comparadas, mesmo sendo as modificações produzidas através de técnicas de fabricação muito diferentes.

**Palavras chaves:** Tribologia. Sinterização. Porosidade. Textura Superficial. Relação deslizamento-rolamento.

## Preface

This research thesis was carried out between September 2015 and September 2019 at the Surface Phenomena Laboratory (LFS) at Escola Politécnica (EP), University of São Paulo (USP), São Paulo, Brazil. One year of research (from April 2018 to April 2019) was performed in Tribology group of the Imperial College London, London, United Kingdom. Furthermore, part of the research was inserted in the Project FDTE 1519 (Losses reduction due to friction in automotive transmissions), developed between Escola Politécnica of the University of São Paulo, FCA (Fiat Chrysler Automóveis Brasil Ltda) and FDTE (Foundation for the Technological Development of Engineering). The research activities developed both in Brazil and in the United Kingdom were funded by the São Paulo Research Foundation (FAPESP), Brazil.

I would like to thank my supervisor Prof. Dr. Izabel Fernanda Machado for providing excellent discussions, advise and technical guidance during my doctorate. I achieved several goals through her invaluable supervision. Thanks are expressed to Prof. Daniele Dini for hosting and supervising me at the Imperial College London. He gave me the opportunities to be inserted in one of the most worldwide recognized tribology group for its research excellence. Prof. Dr. Francisco Profito is recognized for his valuable help and for providing suggestions during the last part of my research. I thank my co-authors I. S. Tertuliano, A.J. Tertuliano, Prof. Dr. F. Profito, Dr. N. Fukumasu, Prof. Dr. R. M. Souza, M. O. Cano from LFS lab, Dr. Guilherme Antonio Assis Machado and Prof. Dr. Wagner de Rossi from the Nuclear and Energy Research Institute (IPEN – SP) for their cooperation and support.

FAPESP is thanked for providing a generous financial support during my doctorate (grant N. 2016/25067-9) and also for permitting to develop part of the research abroad (grant N. 2017/21151-8). I also would like to thank the FCA group for giving financial support and the possibility to interact with industry.

Prof. Carsten Gachot (TU Wien, Vienna), Daniel Rodrigues (BRATS – Cajamar, São Paulo, Brazil), Dr. Matt Smeeth (PCS – London, UK), Dr. Carlos Eduardo Pinedo (Heat tech – Mogi das Cruzes – São Paulo, Brazil), Philipp Grützmacher (Universität des Saarlandes, Saarland, Germany) and Prof. Dr. Wagner De Rossi (IPEN – São Paulo, Brazil) deserve thanks for manufacturing sintered and textured samples. The laser equipment operated by Prof. Dr. Wagner de Rossi (IPEN – São Paulo, Brazil) was also financed by FAPESP (grant N. 2013/26113-6).

I also wish to acknowledge all my lab colleagues and technicians for being there to help and support me every day during my research.

São Paulo, July 2019

Guido Boidi

# Contents

<b>List of figures</b> .....	<b>viii</b>
<b>List of tables</b> .....	<b>xii</b>
<b>Abbreviations and acronyms</b> .....	<b>xiv</b>
<b>Nomenclature</b> .....	<b>xvi</b>
<b>Publications</b> .....	<b>xvii</b>
<b>Chapter 1 Introduction</b> .....	<b>1</b>
1.1 Context of the research .....	1
1.2 Objectives .....	2
1.3 Research questions .....	3
1.4 Thesis outline .....	3
<b>Chapter 2 Manufacturing processes of samples with surface micro cavities</b> .	<b>5</b>
2.1 Introduction .....	5
2.2 Sintering process .....	5
2.2.1 Powder metallurgy .....	5
2.2.2 Spark Plasma Sintering (SPS) technique .....	6
2.2.3 Sintering parameters effects on porosity and pores morphology .....	8
2.2.4 Sintered samples for experimental studies: manufacturing methods and parameters used .....	9
2.3 Texturing process .....	12
2.3.1 Texturing techniques .....	12
2.3.2 Manufacturing methods of textured samples for experimental studies	13
2.4 Conclusions and final remarks of the chapter .....	14
<b>Chapter 3 Characterization of the specimens</b> .....	<b>16</b>
3.1 Introduction .....	16

3.2	General characterization .....	16
3.3	Porosity and pore morphology measurements.....	17
3.4	Determination of elastic properties and roughness evaluation of PM samples .....	21
3.5	Surface characterization of textured features.....	23
3.6	Conclusions and final remarks of the chapter .....	27
<b>Chapter 4</b>	<b>Tribological studies of textured material .....</b>	<b>29</b>
4.1	Introduction .....	29
4.2	Lubrication regimes.....	29
4.3	Tribological effect of surface topography.....	31
4.4	Tribological effect of surface texture.....	33
4.5	Experimental studies of textured surfaces .....	35
4.5.1	Tribological testing .....	35
4.5.2	Results and discussion .....	39
4.6	Conclusions and final remarks of the chapter .....	54
<b>Chapter 5</b>	<b>Tribological studies of sintered material .....</b>	<b>55</b>
5.1	Introduction .....	55
5.2	Tribological effect of surface porosity in PM materials .....	55
5.3	Experimental studies of sintered materials.....	57
5.3.1	Tribological testing .....	57
5.3.2	Results and discussion .....	62
5.4	Conclusions and final remarks of the chapter .....	73
<b>Chapter 6</b>	<b>Phenomenological model proposal .....</b>	<b>75</b>
6.1	Introduction .....	75
6.2	Model .....	75
6.3	Conclusions and final remarks of the chapter .....	84

<b>Chapter 7</b>	<b>Conclusions and future works.....</b>	<b>86</b>
7.1	Main conclusions.....	86
7.2	Contributions.....	88
7.3	Future work suggestions.....	89
<b>Bibliography</b>	.....	<b>90</b>

## List of figures

Figure 1.1 – Schematic representation of thesis outline.....	4
Figure 2.1 – Schematic representation of SPS sintering chamber, adapted from [30].	7
Figure 2.2 – (a) Ball models and (b) real example of particle necks formation during sintering, adapted from [39]. $r$ is the radius of the particles, $x$ is the radius of the neck and $\rho$ is the radius of curvature. ....	8
Figure 2.3 – (a) Green-compacted (initial phase of sintering), (b) intermediate phase with formation of necks and (c) final sintering phase, porosity reduction and formation of rounded pores, adapted from [38]. ....	9
Figure 2.4 – Microstructure of PM samples after (a) sintering and (b) quenching processes [19]. ....	11
Figure 2.5 – (a) Schematic process for manufacturing sintered (a) balls and (b) disks samples. ....	11
Figure 2.6 – Sintered disk (SPS) on the left hand side, sintered ball (SPS) on the right and disk sintered through conventional technique in the middle. ....	11
Figure 2.7 – Grooves textured by (a) femtosecond pulse lasers and (b) laser interference metallurgy (DLIP). The area (1 mm x 1 mm) textured using one laser pulse (DLIP) is highlighted in figure (b) and detailed in figure (c). ....	14
Figure 3.1 – Schematic representation of process operation. ....	17
Figure 3.2 – Examples of points networks used for quantitative metallography, adapted from [62]. ....	17
Figure 3.3 – Surface porosity of disks sintered by SPS. (a), (c), (e) SEM and (b), (d), (f) filtered images to highlight porosity. ....	19
Figure 3.4 – Pore size (a) and circularity index (b) distributions of disk sintered using SPS technique.....	19
Figure 3.5 – SEM surface images of sintered balls (a) B8, (b) B9 and (c) B10. ....	21
Figure 3.6 – Standard dimensions balls and disks from PCS Instruments London used for tribological tests, adapted from [74]. ....	23
Figure 3.7 – Schematic representation of texturing configurations manufactured on smooth disks, top view of disks. $U_e$ represents the entrainment speed, adapted from [18]. ....	24
Figure 3.8 – Schematic representation of texturing configurations manufactured on smooth balls. $U_e$ represents the entrainment speed. ....	25
Figure 3.9 – 3D profile image of grooves produced by Nd:YAG laser. ....	26

Figure 4.1 – Example of Stribeck curve, adapted from [46].	31
Figure 4.2 – Converging and diverging regions of textured micro features, adapted from [9].	32
Figure 4.3 – Schematic examples of crosshatch, chevrons, dimples and grooves.	33
Figure 4.4 – (a) Schematic representation of friction test configuration and (b) details of MTM2 rig, adapted from [18].	35
Figure 4.5 – Schematic representation of test configurations. (a) Reference bench pair NP x NP, (b) textured balls x NP disk and (c) NP ball x textured disk.	36
Figure 4.6 – (a) EHD1 tribometer [74] and (b) details of the configuration of ball on disk using the spectrometer.	37
Figure 4.7 – COF surface response (COF x $U_e$ x SRR) of (a) NP and (b), (c), (d), (e) textured balls (BD, BLG1, BLG2 and BPG) tested against NP disks.	40
Figure 4.8 – “Stribeck like” curves for textured and NP balls tested using (a) SRR 20%, (b) SRR 50%, (c) SRR 100% and (d) SRR 180%. The horizontal axel is in logarithmic scale.	42
Figure 4.9 – <i>Delta friction</i> % for textured and NP balls tested using (a) SRR 20%, (b) SRR 50%, (c) SRR 100% and (d) SRR 180%. The horizontal axel is in logarithmic scale.	43
Figure 4.10 – Images of lubricated contact using different entrainment speed ( $U_e$ ) for NP and textured (BD, BLG1, BLG2 and BPG) balls.	44
Figure 4.11 – Measured minimum film thickness for different textured balls varying entrainment speed (from 10 to 2200 mm/s) and pure rolling. Details of low speed region (below 800 mm/s) and lift-off ( $l_f$ ) speeds values (vertical dashed lines).	46
Figure 4.12 – Schematic representation of lubricant squeeze in (a) dimples, (b) perpendicular and (c) longitudinal grooves configurations.	47
Figure 4.13 – Solid-to-solid contact (%) and area coverage values $f$ (%) for textured balls (BD, BLG1, BLG2 and BPG). Values obtained using the custom made program for film thickness evaluations.	48
Figure 4.14 – “Stribeck like” curves for textured and NP disks tested using (a) SRR 20%, (b) SRR 50%, (c) SRR 100% and (d) SRR 180%. The horizontal axel is in logarithmic scale.	49
Figure 4.15 – <i>Delta friction</i> % for textured and NP disks tested using (a) SRR 20%, (b) SRR 50%, (c) SRR 100% and (d) SRR 180%. The horizontal axel is in logarithmic scale.	50
Figure 4.16 – Lubricant film formation using shallow (< 0.5 $\mu\text{m}$ ) and deep (> 1 $\mu\text{m}$ ) feature configurations.	51

Figure 4.17 – COF x $U_e$ (left vertical axis) and ECR x $U_e$ (right vertical axis) for 120%, NP and textured disks. ....	52
Figure 4.18 – (a) 3D surface image (800 $\mu\text{m}$ x 800 $\mu\text{m}$ ) of wear track on dimple textured disk (DD). (b) Detailed view of the wear track and representative 2D profile along a row of dimples. ....	53
Figure 5.1 – Converging and diverging regions of surface pores in sintered materials. ....	56
Figure 5.2 – (a) Schematic of Bruker tribometer for lubricated tests in the pin-on-disk configuration. Details of (b) tribometer and (c) test set-up configuration, adapted from [23]. ....	58
Figure 5.3 – (a) SPS sintered disk samples in the foreground and NP in the background [21]. Disk specimens were used both for pin-on-disk and roller-on-disk tests. (b) Counter-bodies, roller (non-conformal contact) on the left and flat pin (conformal contact) on the right side. ....	58
Figure 5.4 – (a) Schematic of Bruker tribometer for lubricated tests in the roller-on-disk configuration. Details of (b) SRR device and (c) test set up configuration, adapted from [21]. ....	60
Figure 5.5 – Schematic representation of test configurations. (a) Reference bench pair NP x NP, (b) sintered balls x NP disk and (c) NP ball x sintered disk. ....	62
Figure 5.6 – Average friction and standard deviations values of NP and sintered disks for pin-on-disk configuration, adapted from [23]. ....	63
Figure 5.7 – SEM surface images of D10 sintered disk (a) before and (b) after pin-on-disk test (wear track), adapted from [21]. ....	63
Figure 5.8 – Friction behaviour varying entrainment speed (COF x $U_e$ ) for sintered and NP disks in roller-on-disk configuration. Error bars represent standard deviation for each speed. (a) SRR = 89% and (b) SRR = 131%, adapted from [21]. ....	65
Figure 5.9 – Wear track geometrical dimensions (depth and width) of the sintered and NP disks after roller-on-disk tests, adapted from [21]. ....	66
Figure 5.10 – SEM surface images of D8 sintered disk (a) before roller-on-disk tests and wear tracks after testing using (b) SRR 89% and (c) 131%, adapted from [21]. ..	67
Figure 5.11 – E/H ratio for NP and sintered disks, adapted from [21]. ....	69
Figure 5.12 – COF x $U_e$ for sintered and NP disks in ball-on-disk configuration using (a) SRR 5% and (b) SRR 120%. ....	70
Figure 5.13 – COF x $U_e$ for sintered and NP balls in ball-on-disk configuration using (a) SRR 5% and (b) SRR 120%. ....	71
Figure 5.14 – (a) Wear track of D4 sintered disk and (b) 3D profile image. ....	71

Figure 5.15 – Traction map (COF x lambda ( $\Lambda$ ) x SRR) for NP and sintered balls. ...	72
Figure 5.16 – COF x specific film thickness $\Lambda$ for NP and sintered balls using (a) SRR 5%, (b) SRR 50%, (c) SRR 100% and (d) SRR 120%. .....	73
Figure 6.1 – Coefficient of friction results vs entrainment speeds ( $U_e$ ) for sintered (a) and (b) and textured material (c). Delta $\Delta$ values (%) are expressed below each graph. ....	78
Figure 6.2 – Delta $\Delta$ results (%) of sintered (LP, IP and SP) and textured (D, SG and DG) materials. ....	78
Figure 6.3 – Methodology adopted for the empirical definition of surface parameter $s$ . ....	80
Figure 6.4 – Sequence of operations for obtaining a numerical definition of parameter $s$ . ....	81
Figure 6.5 – Coefficient of friction results vs entrainment speeds ( $U_e$ ) for sintered (a) and (b) and textured material (c). Dashed markers represent experimental results of surface features, where the apex ' is related to the analytical response. ....	84

## List of tables

Table 2.1 – Direct comparison between main characteristics of conventional and SPS technique.....	8
Table 2.2 – Parameters adapted for sintering ball ( <b>B</b> ) and disk ( <b>D</b> ) specimens through SPS and conventional sintering technique. ....	10
Table 3.1 – Surface porosity and pore characteristics of disks sintered through SPS and conventional technique.....	20
Table 3.2 – Bulk and surface porosity characteristics of ball-shaped samples sintered through SPS.....	21
Table 3.3 – Geometrical characteristics and laser parameters used for disk texturing (Ti-Sapphire laser), adapted from [18].....	25
Table 3.4 – Geometrical characteristic, laser techniques and parameters used for ball texturing.....	26
Table 3.5 – Summary of surface micro features topographical characteristics.....	28
Table 4.1 – Geometrical characteristics and main effects of most common texture configurations. Adapted from Gachot et al. [9].....	34
Table 4.2 – Test parameters used for friction (MTM2 rig) and film thickness (EHD1 rig) measurements, textured samples. ....	36
Table 5.1 – Test parameters used for pin-on-disk tests .....	59
Table 5.2 – Test parameters used for roller-on-disk tests .....	61
Table 5.3 – Test parameters used for friction (MTM2 rig) and film thickness (EHD1 rig) measurements, sintered samples. ....	61
Table 5.4 – Roughness parameters (RMS), material properties (E, $\nu$ and H), asperities characteristics ( $\sigma$ and $\beta$ ) and plasticity index $\psi$ of the tested materials.....	68
Table 5.5 – Surface roughness of PM and NP samples for ball-on-disk configuration. ....	69
Table 6.1 – Summary of surface micro feature effects depending on geometry, lubrication and test conditions. Friction result and main effects were compared with a reference wrought material (non-porous or untextured – NP). This table summarizes only results and test conditions that did not alter material surface integrity (reduced surface wear, maintaining the initial geometrical characteristics of micro cavities)....	76
Table 6.2 – Geometrical characteristics of rounded micro features presented in Figure 6.2. Average values of width were considered for surface pores in sintered material (LP, IP, SP).....	82

Table 6.3 – Geometrical characteristics of grooved shape micro features presented in Figure 6.2. Average values of width were considered for surface pores in sintered material (LP, IP, SP).....82

## Abbreviations and acronyms

B8	:	Sintered <b>B</b> all using <b>800</b> °C (SPS)
B9	:	Sintered <b>B</b> all using <b>900</b> °C (SPS)
B10	:	Sintered <b>B</b> all using <b>1000</b> °C (SPS)
BD	:	Textured <b>B</b> all with <b>D</b> imples configuration
BLG1	:	Textured <b>B</b> all with <b>L</b> ongitudinal <b>G</b> rooves configuration 1 (Ti-Sapphire laser)
BLG2	:	Textured <b>B</b> all with <b>L</b> ongitudinal <b>G</b> rooves configuration 2 (Nd:YAG laser)
BPG	:	Textured <b>B</b> all with <b>P</b> erpendicular <b>G</b> rooves configuration
CCD	:	<b>C</b> harged <b>C</b> oupled <b>D</b> evice
COF	:	<b>C</b> oefficient <b>O</b> f <b>F</b> riction
CNC	:	<b>C</b> omputer <b>N</b> umerical <b>C</b> ontrol
D	:	Samples with textured <b>D</b> imples configuration
DD	:	Textured <b>D</b> isk with <b>D</b> imples configuration
DG	:	Samples with textured <b>D</b> eep perpendicular <b>G</b> rooves configuration
DG1	:	Textured <b>D</b> isk with <b>G</b> rooves configuration <b>1</b> (shallow)
DG2	:	Textured <b>D</b> isk with <b>G</b> rooves configuration <b>2</b> (deep)
DLIP	:	<b>D</b> irect <b>L</b> aser <b>I</b> nterference <b>P</b> atterning
D4	:	Sintered <b>D</b> isk using <b>400</b> MPa (conventional technique)
D5	:	Sintered <b>D</b> isk using <b>500</b> MPa (conventional technique)
D6	:	Sintered <b>D</b> isk using <b>600</b> MPa (conventional technique)
D8	:	Sintered <b>D</b> isk using <b>800</b> °C (SPS)
D9	:	Sintered <b>D</b> isk using <b>900</b> °C (SPS)
D10	:	Sintered <b>D</b> isk using <b>1000</b> °C (SPS)
ECR	:	<b>E</b> lectrical <b>C</b> ontact <b>R</b> esistance
EDS	:	<b>E</b> nergy- <b>D</b> ispersive X-ray <b>S</b> pectroscopy
EHL	:	<b>E</b> lastohydrodynamic <b>L</b> ubrication
EP	:	<b>E</b> xtrême <b>P</b> ressure additives
EPUSP	:	<b>P</b> olytechnic <b>S</b> chool of the <b>U</b> niversity of <b>S</b> ão <b>P</b> aulo
FAPESP	:	<b>S</b> tate of <b>S</b> ão <b>P</b> aulo <b>R</b> esearch <b>F</b> oundation
FCA	:	<b>F</b> iat <b>C</b> hrysler <b>A</b> utomóveis Brasil Ltda
FDTE	:	<b>F</b> oundation for the <b>T</b> echnological <b>D</b> evelopment of <b>E</b> ngineering

FIB	:	<b>F</b> ocused <b>I</b> on <b>B</b> eam
HEHL	:	<b>H</b> ard <b>E</b> lastohydrodynamic <b>L</b> ubrication
HT	:	<b>H</b> eat <b>T</b> reatment
HL	:	<b>H</b> ydrodynamic <b>L</b> ubrication
IP	:	<b>I</b> ntermediate <b>P</b> orosity samples
IPEN	:	<b>N</b> uclear <b>E</b> nergy <b>R</b> esearch Institute, São Paulo, Brazil
lf	:	<b>L</b> ift-off <b>S</b> peed
LFS	:	<b>S</b> urface <b>P</b> henomena <b>L</b> aboratory
LOM	:	<b>L</b> ight <b>O</b> ptical <b>M</b> icroscope
LP	:	<b>L</b> arge <b>P</b> orosity samples
LST	:	<b>L</b> aser <b>S</b> urface <b>T</b> exturing
MTM	:	<b>M</b> ini <b>T</b> raction <b>M</b> achine
NP	:	<b>N</b> ormal <b>P</b> roduction
PCT	:	<b>P</b> hotochemical <b>T</b> exturing
PM	:	<b>P</b> owder <b>M</b> etallurgy
RGB	:	<b>R</b> ed, <b>G</b> reen and <b>B</b> lue
RMS	:	<b>R</b> oot <b>M</b> ean <b>S</b> quare height of surface roughness
SEM	:	<b>S</b> canning <b>E</b> lectron <b>M</b> icroscopy
SEHL	:	<b>S</b> oft <b>E</b> lastohydrodynamic <b>L</b> ubrication
SG	:	Samples with textured <b>S</b> hallow perpendicular <b>G</b> rooves configuration
SLIM	:	<b>S</b> pacer <b>L</b> ayer <b>I</b> maging <b>M</b> ethod
SP	:	<b>S</b> mall <b>P</b> orosity samples
SPS	:	<b>S</b> park <b>P</b> lasma <b>S</b> intering
SRR	:	<b>S</b> lide-to- <b>R</b> oll <b>R</b> atio

## Nomenclature

d	:	Feature depth [ $\mu\text{m}$ ]
E	:	Elastic modulus [GPa]
E*	:	Composite elastic modulus [GPa]
f	:	Feature area coverage [%]
H	:	Surface Hardness [GPa]
$h_c$	:	Central film thickness [nm]
$H_s$	:	Hersey number [-]
R	:	Feature depth/width ratio [-]
s	:	Surface parameter [-]
$S_{pq}$	:	Surface parameter of plateau root mean square height [nm]
$S_q$	:	Surface parameter of root mean square height [nm]
$U_e$	:	Entrainment speed [mm/s]
$U_s$	:	Sliding speed [mm/s]
w	:	Feature width [ $\mu\text{m}$ ]

## Greek alphabet symbols

$\beta$	:	Mean radius of asperities [ $\mu\text{m}$ ]
$\Delta$	:	$\Delta = \left( \frac{COF_{features} - COF_{NP}}{COF_{NP}} \right) \times 100$ . Friction difference between features and standard material response [%]
$\eta$	:	Absolute viscosity [Pa·s]
$\Lambda$	:	Specific film thickness [-]
$\nu$	:	Poisson's ratio [-]
$\rho$	:	Material density [ $\text{g}/\text{cm}^3$ ]
$\sigma$	:	Height standard deviation of asperities [nm]
$\Psi$	:	Plasticity index [-]
$\omega$	:	Rotational speed [rps]

# Publications

## Journal papers

- [1] FUKUMASU, N.K.; BOIDI, G. ; SERIACOPI, V. ; MACHADO, G.A.A. ; SOUZA, R.M. ; MACHADO, I.F. Numerical analyses of stress induced damage during a reciprocating lubricated test of FeCMo SPS sintered alloy. Tribology International, v. 113, p. 443-447, 2017, ([doi:10.1016/j.triboint.2016.12.025](https://doi.org/10.1016/j.triboint.2016.12.025))
- [2] BOIDI, G.; FUKUMASU, N. K.; MACHADO, I. F. Wear and friction performance under lubricated reciprocating tests of steel powder mixtures sintered by Spark Plasma Sintering, Tribology International, v.121, p. 139-147, (<https://doi.org/10.1016/j.triboint.2018.01.032>), 2018.
- [3] BOIDI, G.; TERTULIANO, I. S.; PROFITO, F.J.; DE ROSSI, W.; MACHADO, I.F. Effect of laser surface texturing on friction behaviour in elastohydrodynamically lubricated point contact under different sliding-rolling conditions, Tribology International, 2019 ([doi:10.1016/j.triboint.2019.02.021](https://doi.org/10.1016/j.triboint.2019.02.021)).
- [4] BOIDI, G.; TERTULIANO, I. S.; LIMA, L.G.B.S.; PROFITO, F.J.; MACHADO, I.F. Porosity effect of sintered steel on the frictional performance of conformal and non-conformal lubricated contacts, Tribology Transaction, 2019, Accepted for publication ([doi:10.1080/10402004.2019.1640917](https://doi.org/10.1080/10402004.2019.1640917))
- [5] BOIDI, G.; TERTULIANO, I. S.; CANO, M.F.; MACHADO, G.A.A.; SOUZA, R.M.; MACHADO I.F. Tribological evaluation of sintered and conventional gear materials. SAE International, 2017-36-0153, 2017 (<https://doi.org/10.4271/2017-36-0153>)

## Awards

**Dowson prize** (best paper and presentation) at the 45<sup>th</sup> Leeds-Lyon Symposium on Tribology - September 4-7, 2018, Leeds, UK.

- [1] BOIDI, G.; TERTULIANO, I. S.; PROFITO, F. J.; ROSSI, W.; MACHADO I.F., Effect of laser surface texturing on friction behaviour of lubricated point contact under different sliding-rolling conditions, 45<sup>th</sup> Leeds-Lyon Symposium on Tribology - September 4-7, 2018, Leeds, UK.

## Conference papers

- [1] BOIDI, G. ; TERTULIANO, A. J. ; RODRIGUES, D. ; MACHADO, I. F., Caracterização mecânica de metal duro WC-6Co (%massa) sinterizado via SPS (spark plasma sintering)", 105-078, 22º CBECiMat - Congresso Brasileiro de Engenharia e Ciência dos Materiais, Natal (RN), Brazil, 2016.

## Conference presentations

- [1] BOIDI, G.; FUKUMASU, N. K.; MACHADO, G. A. A.; MACHADO, I. F. Lubricated wear and friction performance of SPS sintered FeCMo and FeCCr powder mixtures. 43<sup>rd</sup> Leeds-Lyon Symposium on Tribology, "Tribology (The Jost report – 50 years on)", Leeds, UK, 2016.
- [2] BOIDI, G.; TERTULIANO, I. S.; MACHADO I.F., Tribological effect of porosity in sintered steel varying sliding / rolling, in: 18th Nordic Symposium on Tribology – NORDTRIB 2018, 2018, 3.2.4, pp. 37–38.
- [3] BOIDI, G.; TERTULIANO, I. S.; PROFITO, F.J.; DE ROSSI, W.; MACHADO, I.F. Effect of laser surface texturing on friction behaviour of lubricated point contact under different sliding-rolling conditions, in: 45th Leeds-Lyon Symposium on Tribology, Leeds, UK, 2018, 8.3
- [4] TERTULIANO, A.J.O.; BOIDI, G; MACHADO, I.F.; TROMBINI, V; Comminution influence on mechanical properties of NbC consolidated by Spark Plasma Sintering, in 7<sup>th</sup> International Congress on Ceramics – ICC7, Foz do Iguaçu, Brazil, June 17-21, 2018

# Chapter 1 Introduction

## 1.1 Context of the research

Tribological studies in mechanical parts aimed at increasing the overall efficiency is not a new topic for the scientific community [1,2], however the interest in reduction friction has risen in recent years boosted by stricter standard emission regulations [3]. Tribologists used different strategies to face these restrictions and improving tribological performance, such as studying the effect of low viscosity and fully formulated lubricants, hard coating and surface topography modifications. The latter was especially scrutinized using texturing techniques and in particular the Laser Surface Texturing (LST), largely used in the last decades [4]. The application of designed surface patterns through texturing techniques permitted in some cases a significant friction reduction compared to smooth surfaces [5–8]. For this reason, the interest in studying tribological effect of surface texturing increased in recent years [4].

The design of surface texture combined with test conditions involved a wide range of parameters; therefore, it is difficult to select a specific texture configuration that reduces friction in different tribological conditions [4,9,10]. Despite the large number of papers related to textured material, there are some aspects poorly understood, such as those related to non-conformal contact and components working under sliding-rolling conditions. The use of texturing technique always brings additional manufacturing costs and sometimes the beneficial effect in terms of friction reduction could not be justified in real engineering application.

On the other hand, Powder Metallurgy (PM) is a lower cost manufacturing technique than texturing ones, especially used for large-scale production. PM materials generally present porosity, which have detrimental effects on mechanical properties. Surface pores could be somehow compared to surface micro cavities produced by texturing technique, thus porosity could potentially improve tribological performance in specific conditions. Mechanical effects of porosity were largely studied and evaluated [11–14], however only few researches ventured to attempt evaluating the tribological effects of pores up to now [15–17].

Lack in understanding of the tribological behaviour related to textured materials and the scarcity of tribological studies regarding PM materials motivated this work. Furthermore, this research is also driven by the ambitious comparison between the tribological effects of surface cavities produced by two very different manufacturing techniques, respectively, texturing and sintering.

## 1.2 Objectives

The objectives of this research could be summarized in the following:

- Manufacture steel samples (sintered and textured) for obtaining different surface features. It implies:
  - Produce disk and ball-shaped samples of sintered material involving a sequence of manufacturing and machining operations;
  - Apply surface texture on plain samples (disks) and curved ones (balls);
- Tune sintering parameters to control porosity and pore features for obtaining similar morphological and geometrical characteristics of textured samples;
- Verify the potential application of sintered materials to achieve superior tribological performances with reduced costs and environmental impact;
- Improve the current knowledge on the tribological effects of micro surface irregularities during lubricated sliding-rolling conditions and especially non-conformal contact;
- Measure film thickness on sintered and textured samples using a novel technique designed for rough surfaces;
- Map the tribological results based on geometrical configurations of surface features and propose an analytic tool that help to better understand and possibly predict the tribological behaviour of surface micro irregularities (texture and porosity).

### **1.3 Research questions**

A series of research questions derived from the objectives and answers for those were addressed during the test:

- 1) How porosity characteristics in PM can be precisely controlled and designed?
- 2) Can surface texture and porosity be compared in terms of geometrical characteristics and tribological performance? If so, which parameters can be used?
- 3) Do the pores size and morphology distribution influence the tribological behaviour in PM material? If so, which characteristics can improve tribological performance for non-conformal contacts?
- 4) In which tests conditions surface micro irregularities (texture and porosity) improve tribological performance?
- 5) Can surface porosity in PM materials lead to similar tribological effects of surface texture? If so, how results can be mapped and categorized as to produce a comprehensive phenomenological model?
- 6) Is it possible to predict the friction response of surface with micro cavities from results of reference material using analytic tools?

### **1.4 Thesis outline**

This thesis is divided into seven chapters, each one presenting an introductory and a conclusive section, which respectively present a brief content outline and main highlights of each chapter.

Chapter 2 describes general aspects of sintering and texturing processes, especially focusing on the techniques and equipment used for manufacturing the experimental samples. Furthermore, the effects of sintering parameters on pore characteristics were described.

Chapter 3 describes the techniques used for characterizing the microstructure, mechanical properties and surface conditions of samples. Specific sections were dedicated respectively to sintered and textured materials to better describe surface features characteristics.

Chapter 4 provides a literature review of lubrication regimes and tribological effects of surface irregularities and texture. In the same chapter the experimental studies of textured material were presented.

Chapter 5 scrutinizes the tribological behaviour of PM material through a literature survey. The experimental investigation of sintered material is reported in this chapter.

Chapter 6 presents the phenomenological model proposal obtained using experimental results of the thesis work. Some principal results and their tribological effects were categorized and organized and a surface parameter  $s$  was obtained. Friction response of samples with surface irregularities (porosity and texture) could be scaled by  $s$  parameter from friction response of reference material (smooth, untextured or non-porous).

Chapter 7 summarizes main conclusions of this work, original contributions and suggests possible future researches. Thesis outline is depicted in Figure 1.1.

The essential information for understanding the research was reported here, and complementarily the main results obtained has been already published elsewhere [18–23].

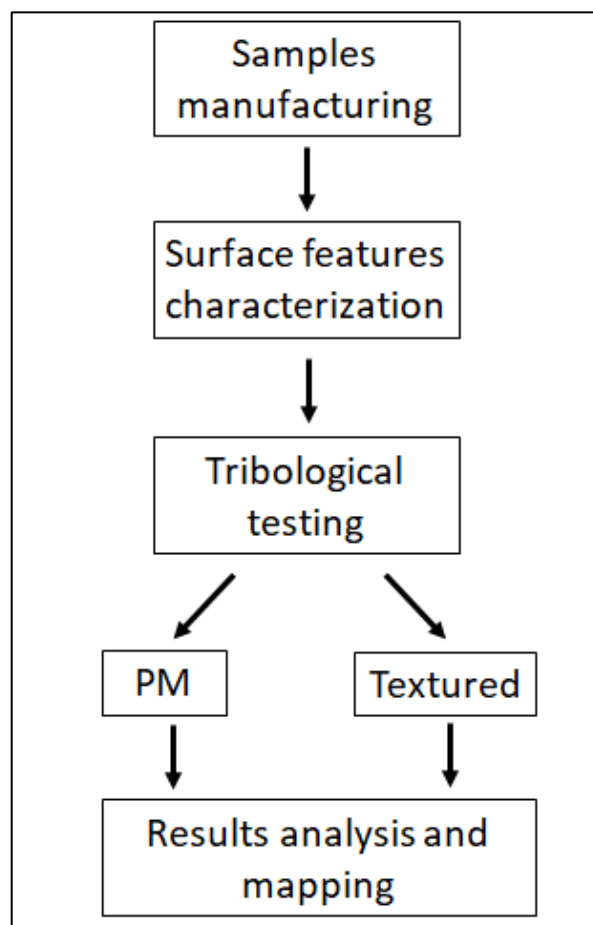


Figure 1.1 – Schematic representation of thesis outline.

## **Chapter 2      Manufacturing processes of samples with surface micro cavities**

### **2.1 Introduction**

Manufacturing processes alter material geometrical characteristics and in most of the cases they also influence microstructure and surface conditions. In this chapter, the sintering and texturing techniques were briefly revised, focusing on the effects of control parameters on surface micro irregularities, since they influence the tribological behaviour. Furthermore, the manufacturing techniques used both for texturing and sintering samples were presented in the next sections.

### **2.2 Sintering process**

#### **2.2.1 Powder metallurgy**

Powder Metallurgy is a manufacturing process that allows the manufacture of components using powder mixtures through the sintering technique. Conventionally, powders are mixed to achieve the desired composition and homogeneous distribution of particle size and then compacted to form a solid component (named “green” component), which have the typical properties of the dense solids. The compacting process occurs by pressing the powders into suitable dies. After that, the “green” component is heated in a furnace below the material melting temperature (typically from 70 to 90% of melting temperature) [24], so that the powder particles fuse together by diffusion and one solid piece is created. Despite the process could be performed in different ways, depending on the compacting techniques and the furnaces used, the principal steps are powder production and mixing, compaction phase, extraction from the die and finally the sintering in the furnace at a controlled atmosphere.

The consolidation process during sintering occurs when the compacted powder particles are in contact one to each other, exclusively through some portions of the outer surfaces, forming necks between them. Consequently, the regions that are not in contact will form micro cavities between the particles, called pores. Pores can be

open or close (occluded) depending on whether they are interconnected and connected with the surface of the component [25]. Many properties of the sintered materials are directly related to the technological process used and to processing parameters. One of the most important properties to be evaluated is porosity, resulting from the compaction characteristics or an insufficient degree of diffusion of the binder elements in the material. Details and information regarding this process are reported elsewhere [26–28].

Porosity in PM materials depends on both sintering parameters and powder particles dimension, shape and distribution [24]. Powder particle morphology mainly depends on production technique and parameters used. Powder produced by atomization generally presents regular rounded particles, whereas mechanical and chemical techniques lead to more irregular shapes. Similar particle dimensions and irregular shapes could favour compaction and reduce porosity [24]. Mechanical properties of powder particles also influence densification, being that plastic deformation could increase compacting rate of “green” parts and consequently reduce porosity. The principal control parameters of sintering processes are compacting pressure, sintering temperature and holding time. The effects of these parameters on porosity characteristics are evaluated in Section 2.2.3.

### 2.2.2 Spark Plasma Sintering (SPS) technique

The effect of the electric field has been the focus of a large number of investigations for theoretical and practical reasons for decades [29]. The application of an external electric field influenced the movement of crystalline defects, nucleation and crystal growth, evaporation and oxidation processes, as reported by Chen et al. [30]. The SPS process is a variation of the electric field applied technique and has attracted considerable attention [19,22,31–33].

In the SPS method, the powder samples are usually mounted in a graphite die to improve electrical conductivity. For instance, a pulsed direct current is used simultaneously with a uniaxial pressure to promote consolidation and sintering. Low vacuum is made into the sintering chamber to allow plasma formation between the particles. The passage of pulsed current forms micro discharges in the plasma

region. However, there is no direct evidence of plasma existing between the particles, thus the role of the pulsed current does not remain adequately understood [30].

Regarding the features of the SPS process, it takes few minutes to complete a sintering cycle, whereas the conventional one generally lasts hours. Shorter sintering time is related to higher heating rates easily achieved in the SPS, due to the internal heating of samples by electric current passage rather than to the external one (from the furnace atmosphere to the external surface of the sample) experienced in the case of conventional sintering. The heating rates normally reached in conventional furnace range from 5 to 10 °C/min, thus from 2 to 4 hours are necessary to reach a temperature of 1200 °C. On the other hand, heating rates of approximately 100 °C/min are easily obtained through SPS [29], hence the same temperature can be reached in few minutes. Moreover, the holding time at the sintering temperature is reduced compared to traditional techniques [34]. Figure 2.1 shows a schematic representation of SPS process.

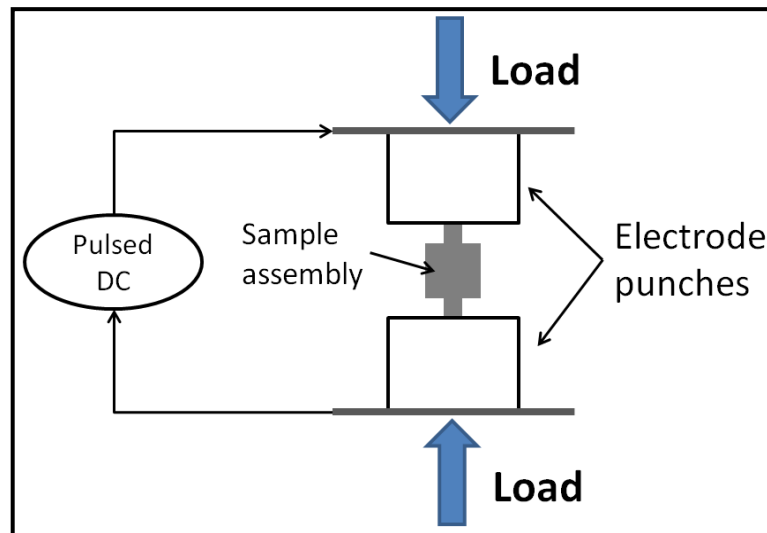


Figure 2.1 – Schematic representation of SPS sintering chamber, adapted from [30].

It is also possible to inhibit grain growth using SPS technique, being that high relative density values are reached in very short times. For these reasons, nanostructured or nanocomposite ceramics can be easily prepared, presenting significant densification and few defects [35–37].

Main aspects of SPS and conventional sintering technique are compared in Table 2.1 [34]. The "+" signs indicate that for a given criterion one technique is better than the other, whilst the "-" signs have opposite meaning. In terms of samples geometry,

the SPS technique is limited to reduced dimension samples and limited geometries, generally only cylindrical shape. Note that the compaction and sintering are two different steps in the conventional sintering techniques, whereas they happen simultaneously using SPS.

Table 2.1 – Direct comparison between main characteristics of conventional and SPS technique.

Technique	Productivity	Speed	Flexibility	Sample geometry	Energy
<b>Conventional</b>	<b>+</b>	<b>-</b>	<b>-</b>	<b>+</b>	<b>-</b>
<b>SPS</b>	<b>-</b>	<b>+</b>	<b>+</b>	<b>-</b>	<b>+</b>

### 2.2.3 Sintering parameters effects on porosity and pores morphology

**Pressure** is applied to compact the powder and consequently it reduces total porosity. The increase of compacting pressure leads to more dense components (less porosity), although mechanical characteristics and morphology of powder particles play an important role in favouring or limiting the compaction. Pressure mainly controls total porosity, whilst pore morphology depends also on sintering process.

The driving force for sintering is the reduction of free surface energy between the particles [26,38]. This energy could be reduced by decreasing the total surface of particles (increase of particles size) or by reducing the interface solid-vapour and creating necks between the particles (densification process), Figure 2.2.

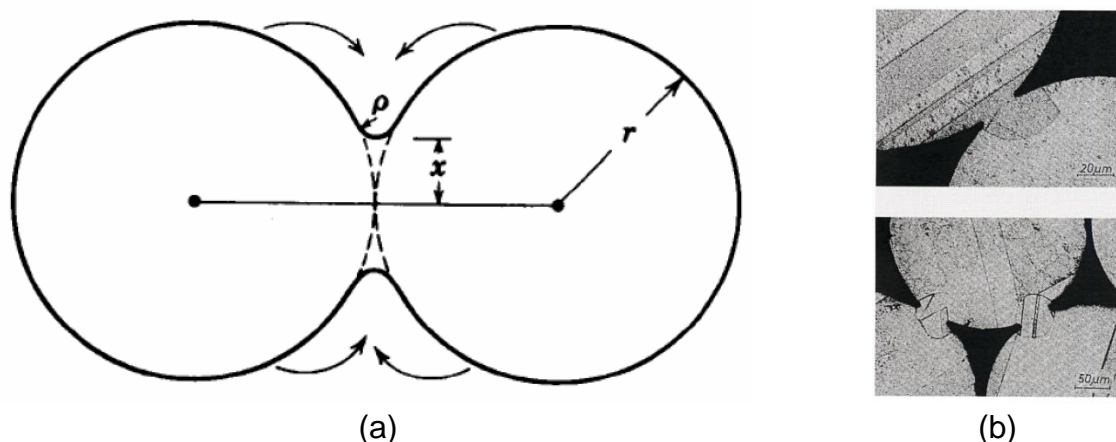


Figure 2.2 – (a) Ball models and (b) real example of particle necks formation during sintering, adapted from [39].  $r$  is the radius of the particles,  $x$  is the radius of the neck and  $\rho$  is the radius of curvature.

The increase of particles size causes pores coalescence, thus larger pores expand and smaller ones restrict. On the other hand, the reduction of surface area and pores volume cause material densification [39].

The reduction of surface area forms more spherical or less irregular cavities, whereas pore volume reduction is due to necks formation between particles or to grain growth, see Figure 2.3.

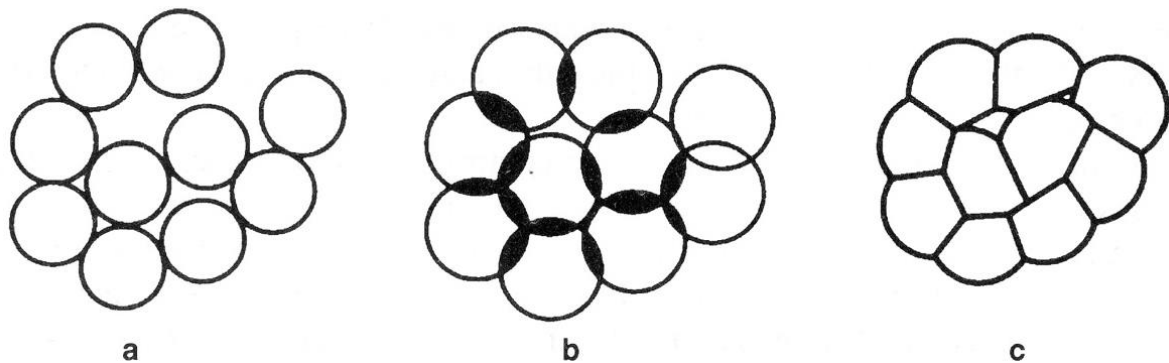


Figure 2.3 – (a) Green-compacted (initial phase of sintering), (b) intermediate phase with formation of necks and (c) final sintering phase, porosity reduction and formation of rounded pores, adapted from [38].

These phenomena involve surface and volumetric diffusion, physical mechanisms of evaporation, condensation and viscous flow, as explained in [38]. **Time** and especially sintering **temperature** have a direct influence on diffusion and consequently on mechanisms related to surface free energy reduction. Temperature favours densification, decreases porosity and pores size, and improves the cavities shape, forming more rounded and less irregular pores [15,17]. On the other hand, time leads to larger diffusion distance.

#### 2.2.4 Sintered samples for experimental studies: manufacturing methods and parameters used

A commercial available steel powder mixture (Astaloy 85Mo from Höganäs Brasil) was used for the sintered material. This steel mixture contained 0.85%wt of Molybdenum and 0.3%wt of Carbon.

The conventional technique was utilized for manufacturing disk-shaped samples. The process was conducted at the company “BRATS” in Cajamar (São Paulo, Brazil)

specialized in the production of metal filters. The compacting pressure varied from 400 MPa to 600 MPa to obtain different pore sizes and characteristics, see Table 2.2. The SPS technique was used for manufacturing of both ball and disk specimens where sintering parameters (time, temperature and pressure) were varied, see Table 2.2. The DR. SINTER® SPS1050 machine is available at the University of São Paulo (Brazil). Holding time, compacting pressure and sintering temperature used for SPS process were much reduced than for conventional technique (Table 2.2.), as reported in literature [29,34] and previously highlighted in Table 2.1 .

Table 2.2 – Parameters adapted for sintering ball (**B**) and disk (**D**) specimens through SPS and conventional sintering technique.

	<b>Sintered disks</b>			<b>Sintered balls and disks</b>		
	<i>Conventional Sintering</i>			<i>SPS</i>		
	<b>D4</b>	<b>D5</b>	<b>D6</b>	<b>B8/D8</b>	<b>B9/D9</b>	<b>B10/D10</b>
Sintering temperature (°C)	1280	1280	1280	<b>800</b>	<b>900</b>	<b>1000</b>
Compacting pressure (MPa)	<b>400</b>	<b>500</b>	<b>600</b>	35	70	70
Holding time (min)	60	60	60	1	5	5

After sintering, disk samples were machined to achieve geometrical standard for tribological tests and then ground for ensuring parallelism. The production of sintered balls required more mechanical operations, since samples produced by SPS are cylinder-shaped. The cylinders were machined to obtain ball-shaped samples with very precise dimensional tolerance, see Figure 2.5.

All the sintered samples were heat treated (HT, water quench at 850 °C) and the “test surface” were polished for reducing the effect of surface irregularities before tribological tests. The specimen microstructure was composed by ferrite and perlite after sintering and martensite after quenching, see Figure 2.4.

SPS disks presented reduced dimensions compared to those produced by conventional sintering technique, as highlighted in Table 2.1. For instance, SPS disks were 20 mm in diameter, whereas conventional sintering ones were 46 mm. Sintered balls were drilled to be fixed on the tribometer and they presented a diameter of 19.05 mm, see Figure 2.6. Disks and balls samples were tested using different tribometers, as explained in Chapter 5.

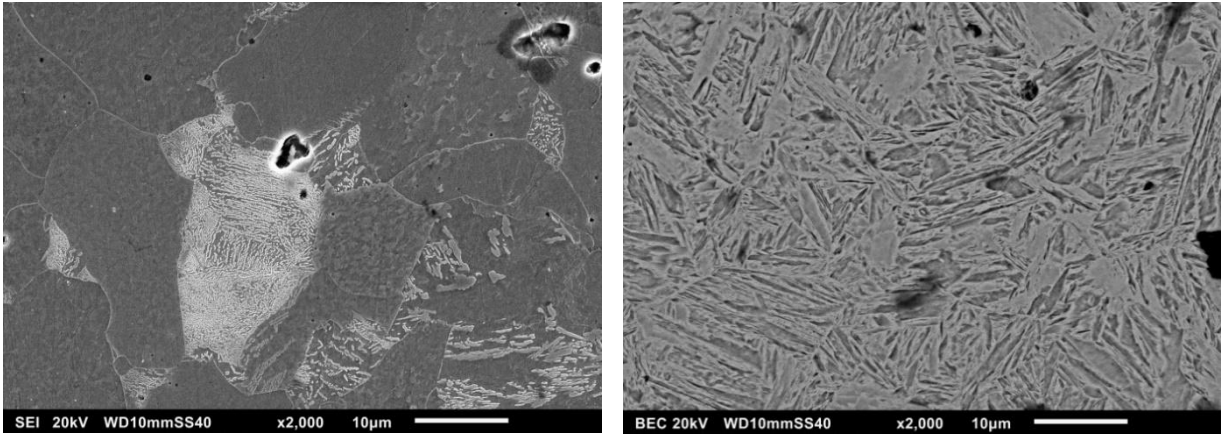


Figure 2.4 – Microstructure of PM samples after (a) sintering and (b) quenching processes [19].

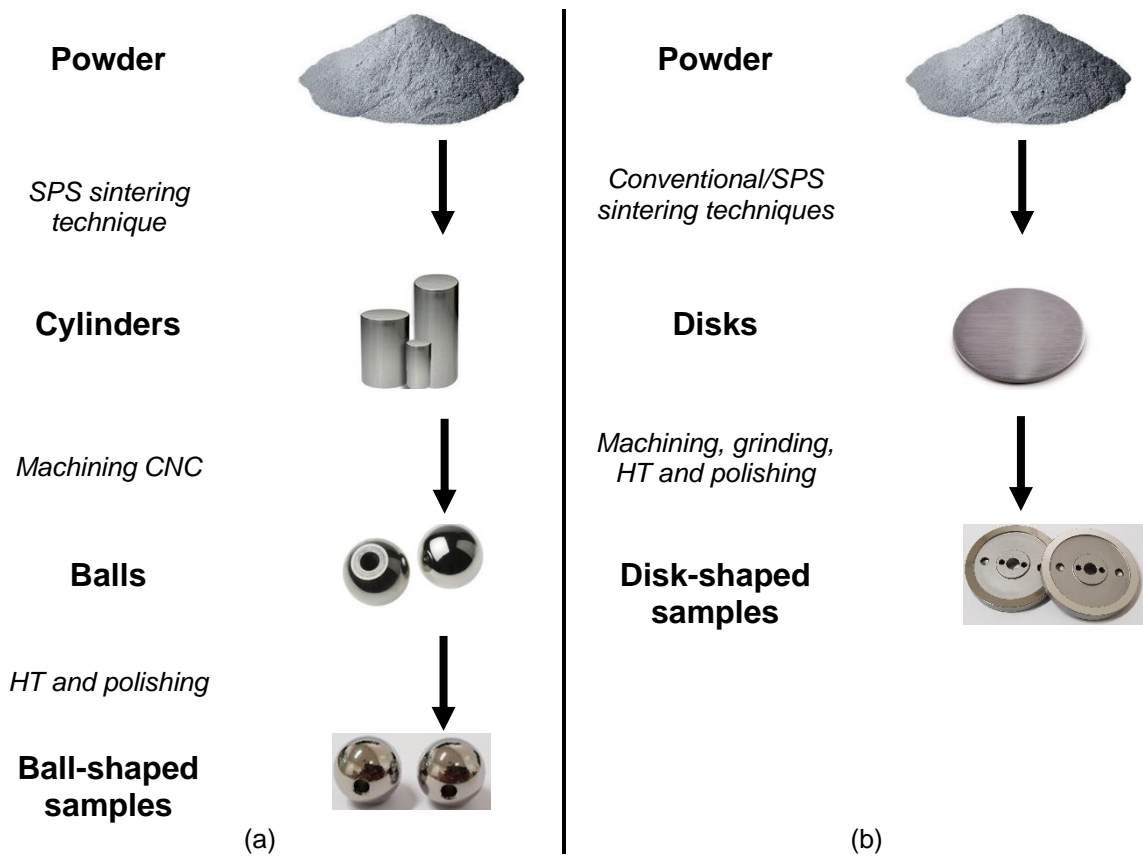


Figure 2.5 – (a) Schematic process for manufacturing sintered (a) balls and (b) disks samples.



Figure 2.6 – Sintered disk (SPS) on the left hand side, sintered ball (SPS) on the right and disk sintered through conventional technique in the middle.

## 2.3 Texturing process

### 2.3.1 Texturing techniques

Surface texture aims at reducing friction, improving lubrication conditions and/or decreasing wear in tribological application. Textured surfaces are generally no longer ideal isotropic due to the introduction of surface micro irregularities. This technique was largely applied for the first time in 1940s. The piston-ring linear of diesel engine presented significant wear and seizure due to absence of lubricant during harsh operation conditions (high load and speed). Cross-hatched grooves were applied on piston linear to improve lubrication and prevent failures [40]. After that in the 1950s and 1960s, texture was utilized for mechanical manufacturing processes (lamination, extrusion and forging) to limit adhesion between parts [1]. Lately in 1990s, the Laser Surface Texturing (LST) technique boosted the disclosure of texturing, especially for mechanical seals [41–45]. The presence of surface micro cavities improves lubricant hydrodynamic pressure, which it is zero for ideally smooth and parallel surfaces [46].

Material could be textured adding or removing material on smooth surfaces, as explained by Gachot et al. [9]. For techniques based on adding material, masks are generally used for inhibiting or favouring material growth. Main techniques are electrodeposition, application of films and surface coatings [9]. Techniques based on removing material can be classified based on the removal source. Although a laser beam through LST is the most common technique, an electron or ion beam could be used for removing material. FIB (*Focused ion beam*) allows high precision removal of material in nanometric scale, however this process is slow and expensive [47]. Material can also be removed chemically through *Photochemical texturing technique* (PCT), where a mask is applied by photolithography and then the material is removed by chemical / electrochemical etching. Finally, material can be removed by mechanical techniques, such as honing or micro machining.

Technique selection tackles several factors, such as the geometry and possible dimensions achieved by the texturing process, cost and compatibility between technique and material. Gachot et al. [9] provided a useful table to help researchers selecting the appropriate texturing technique for a specific application.

### 2.3.2 Manufacturing methods of textured samples for experimental studies

For this study, removal techniques were selected to produce surface micro cavities. Particularly, **LST techniques** were used for being very precise, generally avoiding materials edges and compatibility with steel samples. A laser beam is applied on the material surface for creating micro surface geometries through laser ablation. The high control capacity of laser parameters and movement, the process flexibility and high laser frequency (up to femtosecond) allow the creation of very precise geometries limiting materials edges, which favours lubrication conditions [6–8,48].

Two different LST techniques were used in this study, being respectively: femtosecond pulse lasers (Ti-Sapphire) and Direct Laser Interference Patterning (DLIP) [49].

The femtosecond pulse lasers allowed achieving very precise patterns (see Figure 2.7a), using short pulses with high energy, however long processing times are required [50]. Surface features could assume complex shape, being that laser movement is precisely controlled. On the contrary, DLIP requires reduced processing time, since the laser beam is split and then combined using mirror, lens and beam splitters for texturing greater area than pulsed lasers. Note that area of approximately 1 mm<sup>2</sup> could be textured by one single pulse using laser interference technique, see Figure 2.7b. This technique is similar to lithography, however no masks or etching are required here. Despite this technique requires lower processing times than femtosecond lasers, it generally produces periodic patterns, avoiding the manufacture of complex shapes and different spacing between features [51]. Furthermore, interference process generally leads to less precise patterns due to melting and defect formation during the process [51], see Figure 2.7c. More details about DLPI could be found in [49,52–55].

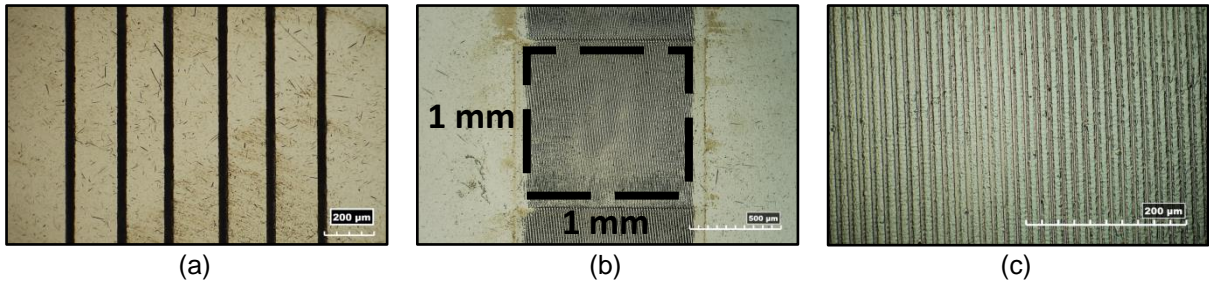


Figure 2.7 – Grooves textured by (a) femtosecond pulse lasers and (b) laser interference metallurgy (DLIP). The area (1 mm x 1 mm) textured using one laser pulse (DLIP) is highlighted in figure (b) and detailed in figure (c).

Surface texture was applied both on plain (disk) and curved (ball) surface samples before being tested using different tribometers; the texture procedures are as follows:

- **Disk samples** were textured using a Ti-sapphire laser (PRO 400 seeder amplified by Femtopower Double 10 kHz both from Femtolasers). This equipment is available at the Nuclear Energy Research Institute (IPEN, São Paulo, Brazil) operated by Prof. Dr. Wagner De Rossi. The linearly polarized laser had pulse length of 30 fs, emission centred at 800 nm, 10 kHz maximum repetition rate and 200 µJ maximum energy per pulse. 10X doublet lens were used to focus the laser beam. Three-axis translator stage (Aerotech ANT130) allowed samples movement through G-codes programming [56].

- **Ball textures** were applied by Philipp Grützmaier, functional materials, Saarland University (Germany) [57]. Curved surface were textured both using femtosecond (Ti:Sapphire laser, Spectra-Physics, Spitfire Pro) and interference lasers (high-power pulsed solid state Nd:YAG laser, Quanta Ray Pro 290, Newport Spectra Physics) [58]. This work was developed in collaboration with Prof. Carsten Gachot, Institute of Engineering Design and Logistics Engineering, TU Wien (Austria). Details of surface texture characteristics and laser parameters can be found in Chapter 3.

## 2.4 Conclusions and final remarks of the chapter

This chapter addressed the general aspects related to the manufacturing techniques utilized in this research. The following conclusion may be drawn:

- Pores features in PM materials depend both on the powder particles characteristics and on the sintering parameters (time, temperature and pressure);
- Conventional and SPS sintering techniques were used to obtain different porosity both for ball and disk-shaped samples;
- The LST technique was selected to manufacture precise texture patterns on the wrought disks and balls;
- Surface textured using Ti-Sapphire laser were more precise and time consuming than those produced by DLIP (Nd:YAG laser). Furthermore, only periodic patterns (fixed spacing between features) were achieved using interference laser.

## **Chapter 3      Characterization of the specimens**

### **3.1 Introduction**

Mechanical properties, wear and friction mechanisms depend on a complex system that involves the interaction of rubbing surfaces in a dynamic environment. Many aspects are involved such as contact mechanics, lubrication, mechanical behaviour of material and microstructural studies. For these reasons, characterization of the specimens represents a fundamental part for tribological studies. In this section, the characterization techniques used in this research are listed and briefly described. Furthermore, two special sections are dedicated to the characterization of randomly distributed surface irregularities (porosities), since they represent a crucial point for understanding the tribological behaviour of PM materials. A section of this chapter was used for detailing surface feature characteristics of textured samples. Finally, a summary table containing the samples nomenclature (both sintered and textured) and surface characteristics was proposed to facilitate interpretation of the results and understanding through the next chapters.

### **3.2 General characterization**

Materials were characterized before tribological tests to evaluate bulk and surface features. Microstructural studies were conducted using metallographic preparation of samples (polishing and chemical etching) and optical analysis (Light Optical Microscope – LOM, Leika DCM3D). Higher magnification and semi-qualitative analysis of chemical composition (EDS – Energy-dispersive X-ray spectroscopy) were carried out by Scanning Electron Microscopy (SEM) Jeol JSM – 6010LA. Vickers hardness was measured varying the load from 10 gf up to 10 kgf, depending on material properties, porosity and microstructure. Digital Vickers tester Buehler VMT-7 and microhardness tester MMT3 were utilized.

Surface morphology and roughness were assessed using a 3D optical interferometry system – Taylor Hobson model CCI MP (magnification of 25X and 50X, TalyMap software). This analysis was conducted on the tested surfaces before and after tribological tests to evaluate initial surface roughness and wear

mechanisms, see Figure 3.1. Furthermore, dimensional characteristics of surface textures were evaluated by quantitative metallography techniques using optical microscopy.

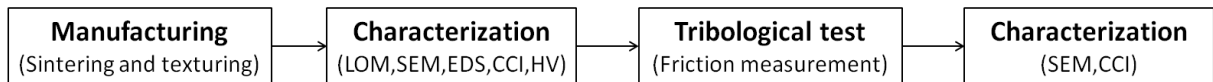


Figure 3.1 – Schematic representation of process operation.

Lubricant properties were measured using an Anton Paar SVM 2001 viscometer [59].

### 3.3 Porosity and pore morphology measurements

Porosity characterization of PM materials plays a crucial role, since pores significantly influence mechanical and tribological properties [11,14,16,19,60]. Besides total (volume) porosity, also pore distribution and main geometrical characteristics should be considered [15,22,23].

PM material density was estimated using Archimedes' principle [61]. Relative density (%) was determined by comparing the measured and theoretical density of PM material, calculated using mixture rule ( $7.83 \text{ g/cm}^3$  for the mixture used). Relative density measurements (%) were used to obtain an estimation of total material porosity.

A 2D image analysis was conducted to confirm porosity values obtained by density measurements and to better characterize distribution and dimensional properties of surface pores. Quantitative metallography is a conventional technique used for this analysis. This method allows determine the quantity, shape, size and distribution of phases or defects. The procedure basically consists in placing a network of points on a certain area of the microstructure for determining specific parameters, see Figure 3.2.

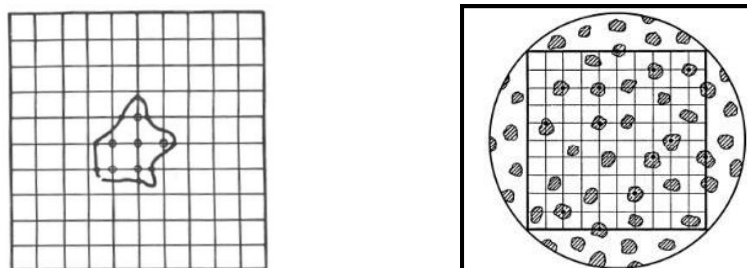


Figure 3.2 – Examples of points networks used for quantitative metallography, adapted from [62].

These parameters are obtained by counting the number of points crossing different types of crystalline defects. More details about the technique and the parameters used could be found in [62].

Several measurements at a specific magnification should be conducted to obtain statistically reliable results. For this reason, a digital image analysis was adopted. Surface images were analysed by the commercially available software Image J® to quantify porosity and pore morphology. The images were obtained using SEM with secondary electrons detectors to highlight pores presence. 2D porosity analysis of SPS disks was depicted in Figure 3.3. Optical images were filtered and processed using ImageJ® to better visualize pores and enhance porosity evaluation.

High sintering temperatures (increasing from 800 °C for D8 and 1000 °C for D10) decreased porosity and pore dimensions, see Figure 3.3 and Table 2.2. This qualitative visual evaluation was supported by statistical analysis using ImageJ®. The software ImageJ® can quantify total porosity and pores features, such as pore perimeter, area, distribution, mean distance and average size. In this research, only the most commonly used parameters [63] were considered:

$$\text{Pore size} = \left(\frac{A}{\pi}\right)^{1/2} \quad (1)$$

$$\text{Circularity index} = \left(\frac{4\pi A}{P^2}\right) \quad (2)$$

where P and A represent respectively the perimeter and the area of pore. The circularity index ideally ranges from 0 to 1, being that highly irregular features assume values close to 0 and rounded ones close to 1.

Pore size and circularity index distribution of SPS disk were shown in Figure 3.4. Three different regions of PM samples were studied to obtain reliable results.

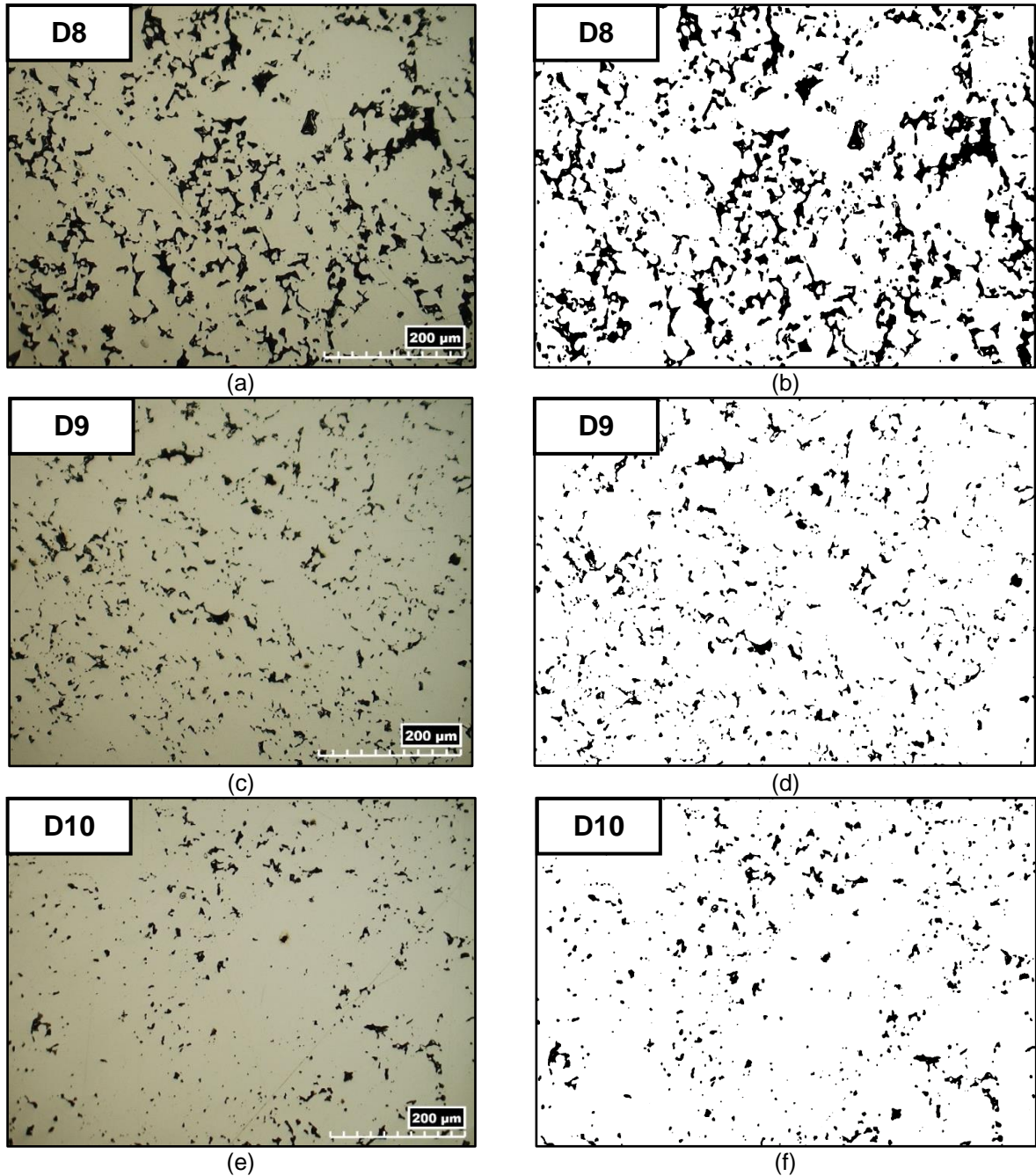


Figure 3.3 – Surface porosity of disks sintered by SPS. (a), (c), (e) SEM and (b), (d), (f) filtered images to highlight porosity.

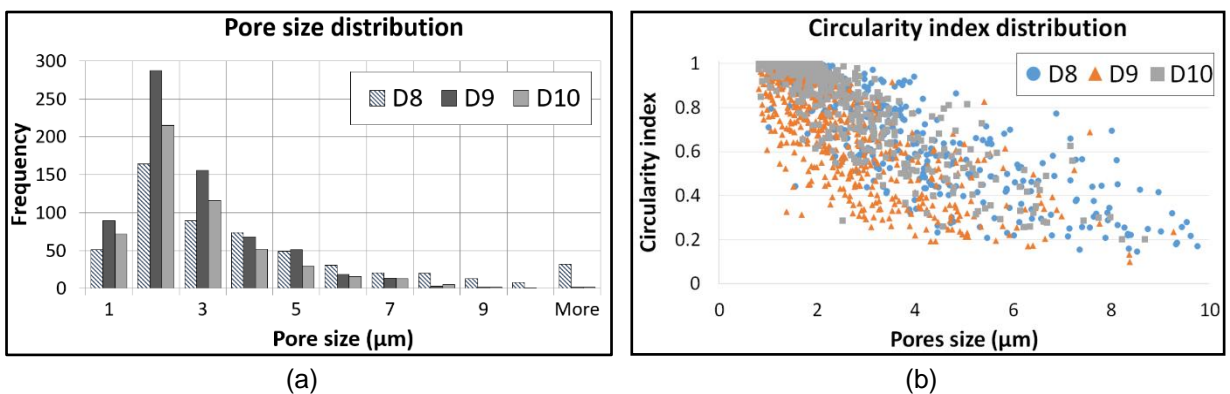


Figure 3.4 – Pore size (a) and circularity index (b) distributions of disk sintered using SPS technique.

Small pores ( $\approx 2 \mu\text{m}$ ) were predominant for the three sintering configurations, whereas the amount of pores decreased with the increase of pore size, see Figure 3.4a. However, more porous disk (D8) still presented a significant quantity of large sized pores. The increase of pore size generally led to more irregular shape (low circularity index), as depicted in Figure 3.4b.

The same porosity characterizations were conducted for disks sintered by conventional technique (D4, D5 and D6). The increase of compacting pressure (from 400 MPa of D4 to 600 MPa of D6) reduced total porosity and pore dimensions. Furthermore, large size pores were less abundant than small ones and presented more irregular shape. The results regarding surface porosity and pore morphology of sintered disks were summarized in Table 3.1.

Table 3.1 – Surface porosity and pore characteristics of disks sintered through SPS and conventional technique.

	<b>Sintered disks</b>					
	<i>Conventional Sintering</i>			<i>SPS</i>		
	<b>D4</b>	<b>D5</b>	<b>D6</b>	<b>D8</b>	<b>D9</b>	<b>D10</b>
Density ( $\text{g/cm}^3$ )	6.7	6.9	7.0	6.6	7.4	7.5
Relative density (%)	86%	88%	89%	84%	94%	96%
Surface porosity	14%	12%	11%	16%	6%	4%
Maximum pores size ( $\mu\text{m}$ )	49	40	38	28	13	11
Average pores size ( $\mu\text{m}$ )	7.1	6.5	5.4	3.7	2.3	2.3
Average circularity index	$0.5 \pm 0.3$	$0.6 \pm 0.2$	$0.6 \pm 0.2$	$0.5 \pm 0.3$	$0.6 \pm 0.2$	$0.8 \pm 0.2$

Compacting pressure and sintering temperature played a similar role for reducing porosity in conventional and SPS disks, see Table 2.2 and Table 3.1. Particularly, average and maximum pore size decreased when using higher compacting pressure (D6) and sintering temperature (D10). Furthermore, pores presented more regular shape (higher circularity index) of less porous disks (D6 and D10).

**PM balls** were sintered using the same parameters of SPS disks (see Table 2.2), therefore they presented same bulk density and porosity, see Table 3.1. However, machining operations from cylinders to ball-shaped specimens (see Figure 2.5) caused plastic deformation on the surface. Surface pores collapsed for less porous balls (B9 and B10), whereas a reduced part of surface cavities (approximately 2%) remained open for more porous samples (B8), see Figure 3.5.

Manufacturing operations (surface grinding, see Figure 2.5) for sintered disks did not cause significant surface deformation, therefore surface pores remained open.

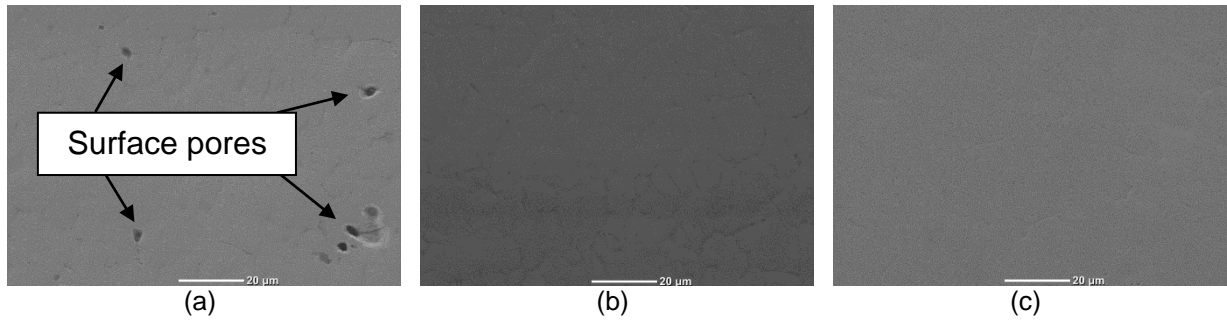


Figure 3.5 – SEM surface images of sintered balls (a) B8, (b) B9 and (c) B10.

Surface and bulk characteristics of sintered balls were summarized in Table 3.2. It is worth noting that bulk properties were evaluated on ball cross sections and presented same values of SPS sintered disks, see Table 3.1. Residual surface pores on B8 samples were round-shaped and small sized (around 2  $\mu\text{m}$ ).

Table 3.2 – Bulk and surface porosity characteristics of ball-shaped samples sintered through SPS.

		<b>Sintered Balls</b>		
		<i>SPS</i>		
		<b>B8</b>	<b>B9</b>	<b>B10</b>
<b>Bulk properties</b>	Density ( $\text{g}/\text{cm}^3$ )	6.6	7.4	7.5
	Relative density (%)	84%	94%	96%
	Bulk porosity	16%	6%	4%
	Maximum pores size ( $\mu\text{m}$ )	28	13	11
	Average pores size ( $\mu\text{m}$ )	3.7	2.3	2.3
	Average circularity index	$0.5 \pm 0.3$	$0.6 \pm 0.2$	$0.8 \pm 0.2$
<b>Surface properties</b>	Surface porosity	Residual porosity ( $\approx 2\%$ )	Pores closure	

### 3.4 Determination of elastic properties and roughness evaluation of PM samples

Mechanical properties of PM materials could be evaluated using mechanical standardized tests, requiring the manufacturing of test samples with specific dimensions. This procedure should be executed for each PM samples, resulting in an expensive and time-consuming process. For this reason, several experimental models were proposed in literature to obtain mechanical properties of PM materials depending on porosity [13,64–67]. Bulk material properties are used as a reference bench and PM properties are estimated (scaled) depending on total porosity or relative density.

Elastic properties of materials are fundamental for contact mechanics and for the evaluation of contact conditions during tribological tests. After a literature review, two equations were selected for estimating elastic modulus ( $E$ ) and Poisson's ratio ( $\nu$ ) [17,68]:

$$E = E' \left( \frac{\rho}{\rho'} \right)^{3.4} \quad (3)$$

$$\nu = \nu' (1 - C_v * p)^{1.6} \quad (4)$$

where  $\rho$  is the material density,  $p$  the pore volume fraction and symbol ' represents bulk reference values. The coefficient  $C_v$  is calculated from the elasticity theory and is defined in [68]:

$$C_v = \frac{5}{9} + \frac{11\nu'}{18} - \frac{1}{18\nu'} \quad (5)$$

Mechanical properties of sintered material were used to determine the plasticity index  $\Psi$  and, consequently the plastic proportion of asperity contact:

$$\Psi = \left( \frac{E^*}{H} \right) \left( \frac{\sigma}{\beta} \right)^{\frac{1}{2}} \quad (6)$$

where,  $E^*$  is the composite elastic modulus,  $H$  the surface hardness,  $\sigma$  the standard deviation of height and  $\beta$  the mean radius of asperities [69]. The composite elastic modulus is defined as follows [70]:

$$\frac{1}{E^*} = \left( \frac{1-\nu_1^2}{E_1} \right) + \left( \frac{1-\nu_2^2}{E_2} \right) \quad (7)$$

Surface topography analysis of PM samples is not easily performed, since porosity represents surface micro valleys and negatively affect most of roughness parameters associated with surface height distribution. For these reasons, surface roughness of reference smooth samples and PM materials cannot be directly compared following conventional surface roughness analysis. In this thesis, a pre-processing procedure

was adopted to discard surface pores and cut-off length was carefully selected for avoiding pore contour effects on surface waviness. Furthermore, the  $S_{pq}$  (plateau root mean square height) parameter was adopted for PM materials for mitigating any negative influence of pores. This parameter was largely adopted for roughness measurements of honed cylinder liners [71–73], since it excludes valley (pores) effects.  $S_q$  (root mean square height) parameter was used for evaluating reference smooth material. Roughness parameters of sintered samples are presented in Section 5.3.2.

### 3.5 Surface characterization of textured features

Surface texture was applied both on smooth steel balls and disks samples (AISI 52100). The specimens had smooth surfaces ( $S_a=6$  nm and  $S_q=20$  nm) and standard dimensions for tribological tests: disks were 46 mm in diameter and 6 mm in thickness, whereas balls were 19.05 mm (3/4") in diameter, see Figure 3.6.



Figure 3.6 – Standard dimensions balls and disks from PCS Instruments London used for tribological tests, adapted from [74].

- Linear rows of dimples and radial curved grooves were manufactured on steel **disks**, using the schematized configuration in Figure 3.7.

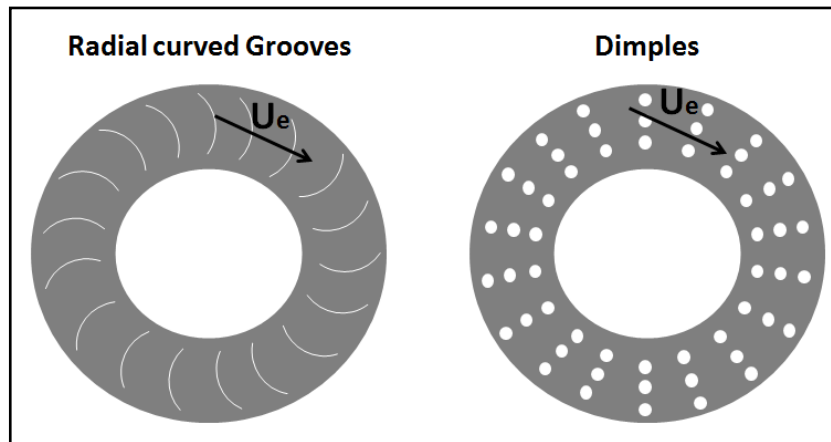


Figure 3.7 – Schematic representation of texturing configurations manufactured on smooth disks, top view of disks.  $U_e$  represents the entrainment speed, adapted from [18].

Different dimensional features were obtained by changing laser control parameters, resulting in two texture configurations for grooves and one for dimples, see Table 3.3. Textured disks are identified as **DG1** (*Disk Grooves configuration 1*), **DG2** (*Disk Grooves configuration 2*) and **DD** (*Disk Dimples configuration*). Groove configuration was designed to present different feature depth, being DG2 deeper than DG1. For this reason, the laser pulse energy and the number of overlapped shots was increased and the laser speed was decreased for DG2, see Table 3.3. Texture design selection was based on literature review [4,9,10]. Features depth was around  $0.5 \mu\text{m}$  for shallow configurations (DG1 and DD) and higher than  $1 \mu\text{m}$  for evaluating the performance of deeper features (DG2). Texture tangential spacing ( $\sim 300 \mu\text{m}$ ) was maintained higher than the contact width ( $\sim 170 \mu\text{m}$  – Hertz contact theory, see Section 4.5.1) to assess the influence of singular texture row within the contact and verify the potential application of low-density texturing (reduce production costs) in real applications.

Table 3.3 – Geometrical characteristics and laser parameters used for disk texturing (Ti-Sapphire laser), adapted from [18].

	Radial Curved Grooves		Dimples
Texture profile			
Texture name	DG1	DG2	DD
Features width $w$ ( $\mu\text{m}$ )	25	20	15
Features depth $d$ ( $\mu\text{m}$ )	0.35	1.35	0.5
Features tangential* spacing ( $\mu\text{m}$ )	300	300	300
Features transversal** spacing ( $\mu\text{m}$ )	/	/	10
Area coverage $f$ (%)	12.5	10	1
Features aspect ratio ( $R = \text{depth}/\text{width}$ )	0.01	0.06	0.03
Laser pulse energy ( $\mu\text{J}/\text{pulse}$ )	2.8	3.5	1.4
Laser number of overlapped shots	4	5	30
Laser processing speed (mm/s)	9	7	/
Laser spot size ( $\mu\text{m}$ )	3.6	3.6	2.4

\*tangential direction is the same direction of entrainment speed

\*\*transversal direction is perpendicular to entrainment speed

- Texture on **ball samples** were also designed in the configuration of dimples and grooves, however configurations were quite different from textured disks, see Figure 3.8.

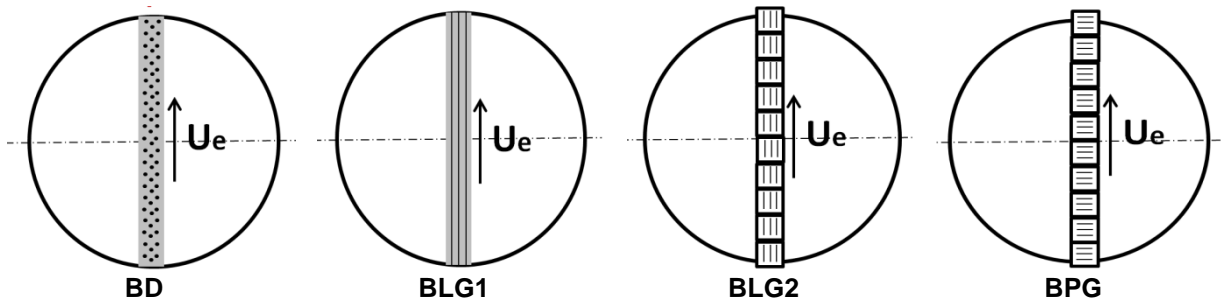
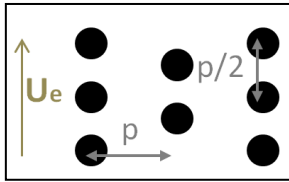
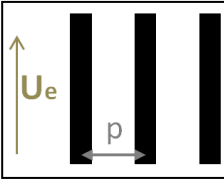


Figure 3.8 – Schematic representation of texturing configurations manufactured on smooth balls.  $U_e$  represents the entrainment speed.

Textured balls are identified as **BD** (*Ball Dimples configuration*), **BLG1** (*Ball Longitudinal Grooves configuration 1*), **BLG2** (*Ball Longitudinal Grooves configuration 2*) and **BPG** (*Ball Perpendicular Grooves configuration*). Geometrical features details, texturing technique and laser control parameters were summarized in Table 3.4.

Table 3.4 – Geometrical characteristic, laser techniques and parameters used for ball texturing.

Texture profile	Dimples	Grooves		
		Longitudinal		Perpendicular
				
Texture name	<b>BD</b>	<b>BLG1</b>	<b>BLG2</b>	<b>BPG</b>
Features width w (μm)	50	35	7	7
Features depth d (μm)	0.1	0.1	0.4	0.4
Spacing p (μm)	200	200	15	15
Area coverage f (%)	14	21	47	47
R = depth/width	0.002	0.003	0.06	0.06
Laser	Ti-Sapphire	Ti-Sapphire	Nd:YAG	Nd:YAG
Pulse duration	100 fs	100 fs	10 ns	10 ns

Feature depth was maintained below 0.5 μm for all configurations for improving performance in non-conformal test conditions, see Section 4.4. Large spacing (~200 μm) was used for Ti-Sapphire laser, since the manufacturing times are significantly long, especially for a curved surface. On the contrary, spacing was around 15 μm for Nd:YAG laser due to operational conditions (see Section 2.3.2). Considering Hertzian contact diameter of ~170 μm (see Section 4.5.1), the influence of singular texture row was analysed for Ti-Sapphire laser, whereas multiple features were contained within the contact for Nd:YAG. Furthermore, feature width is significantly higher for Ti-Sapphire laser rather than Nd:YAG one, see Table 3.4.

Note that Nd:YAG reduced texturing time, however surface morphology is more similar to roughness, being that a periodic pattern was obtained, see Figure 3.9.

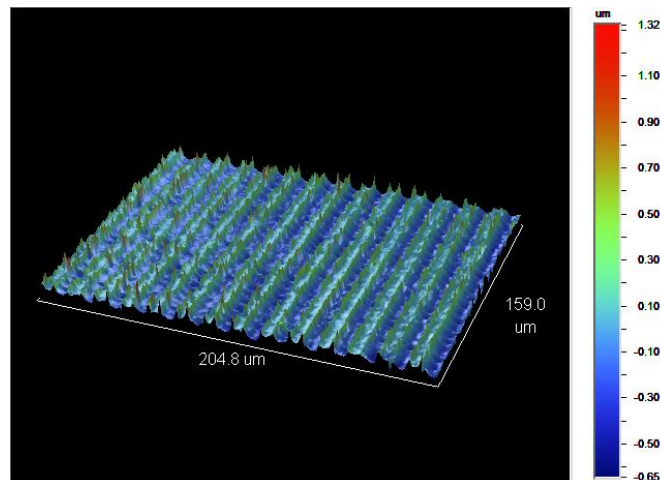


Figure 3.9 – 3D profile image of grooves produced by Nd:YAG laser.

Both for textured and sintered samples, reference smooth surface specimens are used as reference benches. These samples are denominated **NP** (Normal Production) along the text.

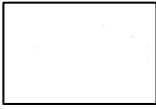
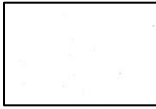
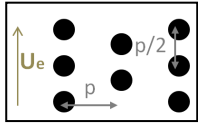
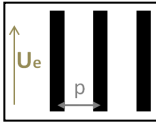
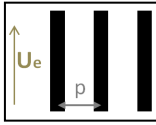
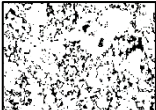
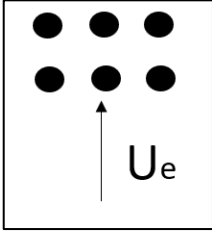
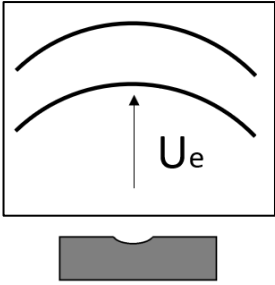
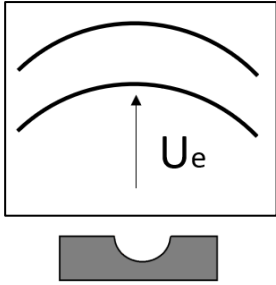
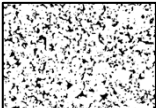
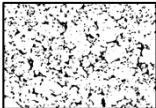
Surface characteristics of features produced by sintering and texturing were summarized in Table 3.5 to improve results interpretation in next sections.

### **3.6 Conclusions and final remarks of the chapter**

This chapter listed the general characterization techniques and the specific ones used for PM materials. The following conclusions can be drawn:

- Microstructural characterization studies were conducted using optical analysis and hardness measurements;
- Surface roughness and surface features characteristics were evaluated by 3D optical interferometry;
- Porosity, relative density and pore characteristic were carried out using a 2D digital image analysis;
- Elastic properties of PM materials were evaluated using experimental models proposed in literature. Furthermore, the plastic proportion of asperity contact was obtained by plasticity index  $\Psi$  calculation;
- A specific procedure was developed for roughness analysis of sintered material to avoid negative pores effects on surface conditions.

Table 3.5 – Summary of surface micro features topographical characteristics.

	Sintered			Textured			
<b>Ball</b>							
	B8	B9	B10	BD	BLG1	BLG2	BP
<b>Disks</b>							
							DD

This table intends to visually summarize surface features characteristics of both textured and sintered samples. Detailed information should be consulted in Table 3.1, Table 3.2, Table 3.3 and Table 3.4.

## Chapter 4 Tribological studies of textured material

Tribological evaluations regarding textured surfaces have been extensively scrutinized in literature [4] as compared to sintered materials, therefore this chapter is presented before those related to sintering sample tribology.

### 4.1 Introduction

The presence of surface micro irregularities alters lubrication conditions and influences component tribological behaviour. Relevant tribological aspects related to lubrication and surface topography effects on frictional response are scrutinized in this chapter. Furthermore, Section 4.4 summarized principal tribological effects of surface texture in different testing conditions, attempting to create guidelines for future texture designs. Finally, main experimental results of textured material are presented.

### 4.2 Lubrication regimes

According to Hamrock [46], four lubrication regimes could be identified: boundary, mixed (or partial), hydrodynamic (HL) and elastohydrodynamic (EHL).

In **HL** regime, there is no contact between asperities and a lubricant film completely separates the surfaces. The hydrodynamic pressures developed within this lubricated film sustain the applied load. Friction depends on lubricant bulk properties (viscosity) and it is governed by lubricant shearing. Low friction and wear characterize this regime, which is typical of contacts involving low pressures (conformal contacts). Film thickness depends on lubricant viscosity, contact geometry and operational conditions (speed and load). No elastic mechanisms are considered, since the contact pressure is low (5 MPa maximum) in conformal contact.

**EHL** is a type of hydrodynamic lubrication (no asperities contact) that involves high contact pressures (non-conformal surfaces), causing significant elastic deformation of surfaces and often viscosity changes of the lubricant. This regime could be further divided into Hard (HEHL) and Soft (SEHL), for materials with respectively high

(metals) and low (elastomers) elastic modulus. In HEHL, surface elastic deformation and pressure-viscosity effects are both relevant. For this reason, besides the parameters used for HD, film thickness also depends on elastic properties of material (composite elastic modulus) and lubricant pressure viscosity coefficient. On the other hand, in SEHL only elastic properties should be considered due to large deformation even for low pressure [46]. Load in EHL has restrained effects on film thickness compared to HL.

In **boundary** lubrication, lubricant film is lower than composite surface roughness, therefore load is supported by asperity contact. Friction behaviour depends on physical and chemical characteristics of the thin surface film formed during the contact, frequently called *tribofilm*. The mechanisms involved in this regime are complex and generally require a multidisciplinary approach, including phenomena related to chemical and physical absorption and chemical reaction on the surface substrate. Friction and wear are higher than EHL and HL due to solid contact between asperities.

Finally in the **mixed** regime, part of the load is supported by asperities and part by lubricant film between surfaces. Friction depends both on bulk and surface film properties of lubricant. The transition between EHL and mixed happens gradually, whereas for HL it happens suddenly. Friction magnitude is between boundary and full film condition (EHL or HL).

Lubrication regime effect on frictional behaviour is normally depicted using the Stribeck curve, see Figure 4.1. The coefficient of friction (COF) is plotted as a function of Hersey number ( $H_s$ ), defined as follows:

$$H_s = \eta \times \left( \frac{\omega}{p} \right) \quad (8)$$

Where  $\eta$ ,  $p$  and  $\omega$  are respectively absolute viscosity (Pa's), pressure (Pa) and rotational speed (rps).

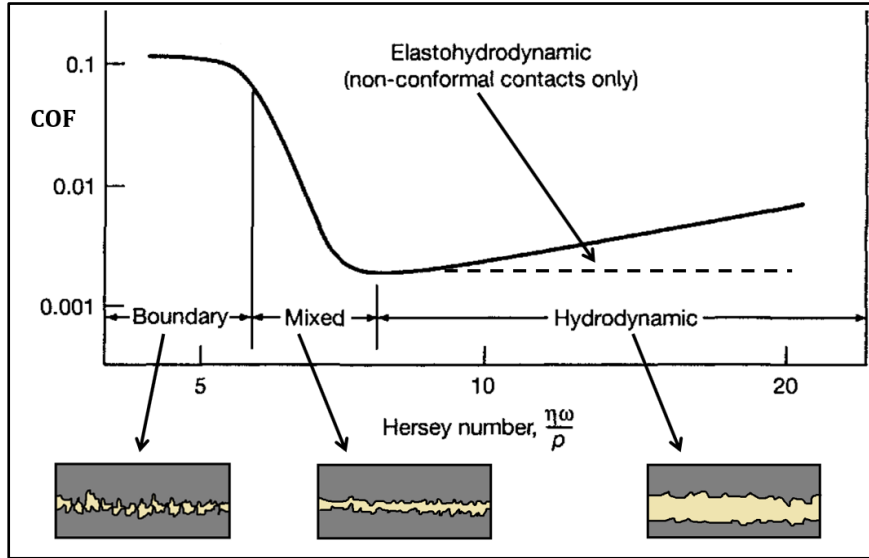


Figure 4.1 – Example of Stribeck curve, adapted from [46].

Stribeck curve could be also traced using specific film thickness  $\Lambda$  [46], instead of Hersey number.  $H_s$  and  $\Lambda$  both assume respectively low and high values for boundary and full film conditions (EHL and HL), presenting intermediate values for mixed lubrication. It is generally assumed that boundary regime had  $\Lambda < 1$ , mixed  $1 < \Lambda < 3$  and for full film conditions  $\Lambda > 3$  [46]. The parameter  $\Lambda$  is defined as follows:

$$\Lambda = \frac{h_c}{\sqrt{RMS_1^2 + RMS_2^2}} \quad (9)$$

where  $RMS_1$  and  $RMS_2$  are the root mean square height of the surface roughness (in this study,  $S_q$  parameter for NP material and  $S_{pq}$  for PM, see Section 3.4) and  $h_c$  is the central film thickness.  $h_c$  could be estimated by Hamrock/Dowson equation [75] and more accurate evaluations [76–78] or it could be measured using interferometry [79–81], capacitance [82], fluorescence [83] and ultrasound [84] methods. Optical interferometry was used in this study and main principles of this technique are scrutinized in Section 4.5.1.

### 4.3 Tribological effect of surface topography

The frictional influence of surface topography onset studies started more than 50 years ago [2]. This work showed how non-conventional topographic conditions (non-isotropic) and the presence of micro surface irregularities can have a direct influence

on the lubricant load carrying capacity, especially for conformal contact [2]. The presence of micro irregularities changes the local topography and surface roughness conditions possibly influencing lubrication conditions. The application of surface texture on smooth surface changed the traditional concept of isotropic surfaces for improving tribological behaviour.

According to the classical theory of lubrication [46], the hydrodynamic pressure generated between two parallel and flat smooth surfaces is zero under steady state conditions. Several factors can promote local pressure rise, such as physical and density wedge effect, local expansion, stretch, normal and transverse squeeze [46]. The effect of surface micro irregularities can be somehow similar to physical wedge effect ("hydrodynamic micro bearings"), since surface cavities represent divergent-convergent regions, see Figure 4.2.

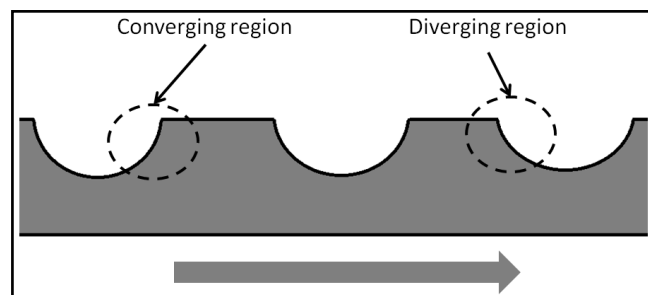


Figure 4.2 – Converging and diverging regions of textured micro features, adapted from [9].

These superficial irregularities generate an asymmetry of the field of hydrodynamic pressures, due to cavitation in the divergent region [5,85,86]. In successful cases, the passage of the counter body causes a local increase of pressure close to converging regions of micro cavities, generating a local viscosity increment, improving lubricant carrying capacity [87]. Furthermore, when the inlet pressure (diverging region) is lower than atmospheric, the lubricant is “sucked” in the feature (inlet suction) supplying extra load support [88,89].

The tribological studies of surface topography also involve lubricant characteristics. For instance, when asperities are in contact (boundary and mixed regimes) it is possible to activate some additives present in the lubricant to generate a specific superficial *tribofilm* able to reduce friction [90,91]. Some types of additives could be activated at high contact pressure (Extreme pressure – EP). Contact pressure is higher when using limited contact area, therefore EP additives are

generally first activated on asperities peaks on rough surfaces, rather than smooth ones [19]. Surface features directionality also represents a key factor to be analysed when using additives [91].

Honing in cylinder liner is a machining process related to surface feature orientation [92,93]. In this process, the feature directionality is controlled and usually assumes angles between  $40^\circ$  and  $50^\circ$  [94]. These grooves are made for promoting lubrication and reducing excessive wear and seizure problem, especially with high load and temperature conditions [40]. In this case a more "irregular" surface with superficial scratches can provide better performance and less wear than a smooth surface due to the topography effect on lubrication.

#### 4.4 Tribological effect of surface texture

Feature shape is probably the first parameter considered during texture design. Although it could ideally assume any shape, the most common geometries are generally dimples, grooves, chevrons and crosshatch, see Figure 4.3.

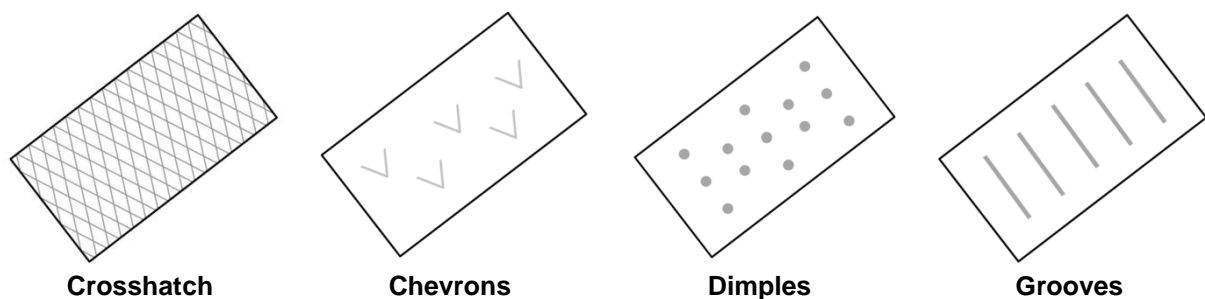


Figure 4.3 – Schematic examples of crosshatch, chevrons, dimples and grooves.

After defining the shape, dimensional parameters should be selected, i.e. depth, width, spacing and distribution. Geometrical design of texture depends on operational conditions of mechanical components. It includes type of contact (conformal or non-conformal), lubrication regime, lubricant characteristics and test parameters (load, speed, temperature, type of movement). The large number of parameters to be controlled for texturing design implied a relevant experience or a significant literature study. For this reason, different authors attempted to support future projects with comprehensive review papers [4,9,10].

Surface texture generally aims at reducing friction and wear, having specific tribological effects on different lubrication conditions, see Table 4.1. For solid-to-solid contact (**boundary** lubrication), surface micro features could reduce wear, since they act as debris trapping and offer extra lubrication (oil reservoirs) [95]. In some cases, surface micro features could increment local hydrodynamic pressure (“micro bearing effect”), promoting friction reduction. However, high area coverage of texture reduced contact area, altering local stress condition and possibly increasing friction and wear.

During **mixed** regime, surface micro features still represent oil reservoirs and can act as debris trapping, however the “micro bearing effect” becomes more relevant [6,96,97]. The effects of texture in **HL** are well established, being that surface features generally increment lubricant carrying capacity reducing friction [98,99] for conformal contact. In addition, surface micro irregularities may shift Stribeck curve [97,100,101], favouring mixed and full film conditions for smaller  $\Lambda$  values. Finally, the tribological effect of surface texture in **EHL** is still under discussion, since some configurations increment friction, whereas others have opposite effects [102–105].

Albeit texture geometrical characteristics are designed for specific operational conditions, a general guide could be created for supporting future texturing projects. For instance, most used and “successfully” geometries were summarized in Table 4.1, based on the more extensive and comprehensive review paper [9]. The values presented in Table 4.1 were taken from different literature [9], hence they are indication, not strict rules.

Table 4.1 – Geometrical characteristics and main effects of most common texture configurations.  
Adapted from Gachot et al. [9]

Effect	Lubrication Regime		
	Boundary	Mixed/HL	EHL
	Debris trapping Lubricant reservoir Increase hydrodynamic pressure	Increase load support Secondary oil effects	Increase/decrease film thickness
Features depth $d$ ( $\mu\text{m}$ )	2-15	1-10	< 0.5
Features width $w$ ( $\mu\text{m}$ )	< contact width	5-100	< contact width
Features aspect ratio ( $R = \text{depth}/\text{width}$ )	-*	$\approx 0.1$	< 0.1
Area coverage $f$ (%)	-	7-12%	10-20%
Shapes	Pockets/Grooves	Pocket/Grooves/Chevrons	Pocket/Grooves
Directionality	-	Perpendicular	Perpendicular

\* - not available

In general, texture width should be smaller than elastic contact dimension (Hertz theory) and grooves should be oriented perpendicular to counter-body movement. Lubricant squeezes along longitudinal features, avoiding any local increment of lubricant pressure. Geometrical characteristics are quite similar for mixed and HL lubrication, presenting a feature aspect ratio  $R$  of approximately 0.1. For EHL, dimensional properties are not well established, however friction reduction is generally obtained using shallow features ( $< 0.5 \mu\text{m}$ ) with  $R$  lower than 0.1.

## 4.5 Experimental studies of textured surfaces

### 4.5.1 Tribological testing

Tribological testing consisted on friction and film thickness measurements. Synthetic base oil PAO 6 was used for all tribological tests. The kinematic viscosity of the oil was  $31 \text{ mm}^2/\text{s}$  at  $40 \text{ }^\circ\text{C}$ .

- **Friction** was evaluated using a ball-on-disk rig (MTM2 – Mini Traction Machine, PCS Instruments London) during lubricated tests, see Figure 4.4. After the ball and disk specimens are fixed on the shafts, the temperature controlled pot is filled with lubricant and the test could start.

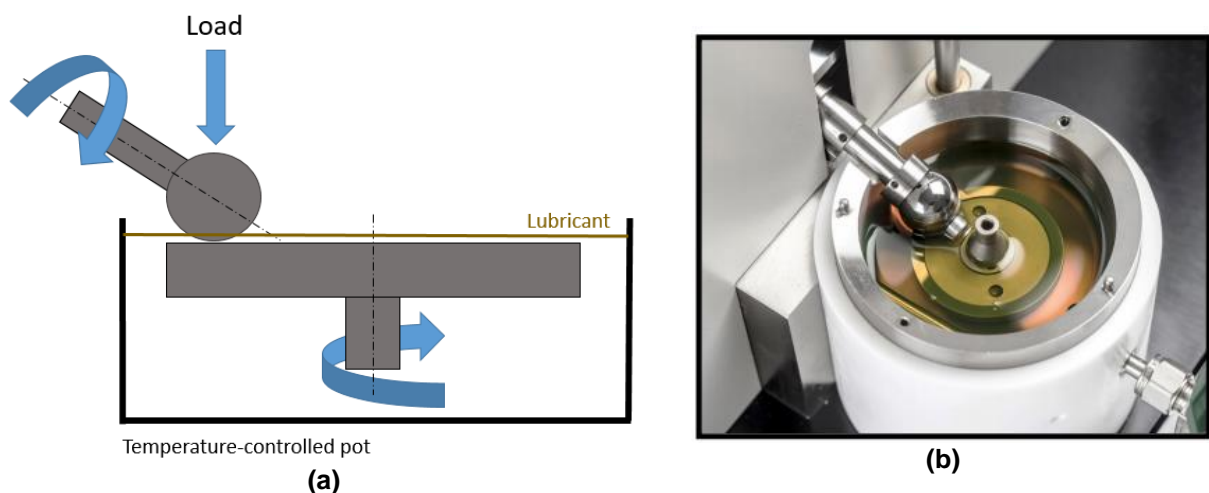


Figure 4.4 – (a) Schematic representation of friction test configuration and (b) details of MTM2 rig, adapted from [18].

Ball and disk are driven by two independent motors, permitting continuous variations of speeds and slide-to-roll ratio (SRR). The SRR is defined as the ratio between sliding  $U_s$  and entrainment  $U_e$  (also known as rolling speed):

$$SRR = 100 \times \frac{U_{Disk} - U_{Ball}}{(U_{Disk} + U_{Ball})/2} = 100 \times \frac{U_s}{U_e} \quad (10)$$

SRR values range from 0% (pure rolling) up to 200% (pure sliding).

Both SRR and  $U_e$  varied during tribological tests (see Table 4.2) to scrutinize a vast range of operational conditions and of lubrication regimes. Tests were repeated twice to ensure statistical reliability.

Table 4.2 – Test parameters used for friction (MTM2 rig) and film thickness (EHD1 rig) measurements, textured samples.

	MTM2 rig	EHD1 rig
Range of entrainment speed, $U_e$ (mm/s)	2000 – 10	2200 – 20
Slide-to-roll ratio, SRR (%)	5 – 20 – 50 – 80 – 100 – 120 – 150 – 180	0
Temperature (°C)	40	40
Contact pressure (GPa)	0.6	0.5

The rig could measure electrical contact resistance (ECR) between the specimens during the test, since ball and disk are electrically insulated. ECR could be used for identifying lubricant regime transitions, since it could qualitatively estimate the amount of solid-to-solid contact. For instance, ECR assumes values of 100% when a lubricant film prevents asperities contacts (EHL). On the contrary, ECR is 0% when the load is fully supported by asperities (boundary lubrication) and the bodies are in contact. Under mixed lubrication, ECR ranges from 0% to 100%, since the load is both supported by asperities and lubricant film. Furthermore, ECR could be used to identify transitional speed from mixed to full-film regime, defined as lift-off speed (lf) [82]. The electrical resistance technique of MTM2 rig does not directly measure film thickness, therefore a specific rig was used to evaluate lubricant gap between the bodies. This methodology is explained in the next paragraphs.

Textured balls and disks were tested separately against non-porous (**NP**) samples, whereas untextured (hereafter designated as **NP** – normal production) pairs were used as reference bench material, see Figure 4.5.

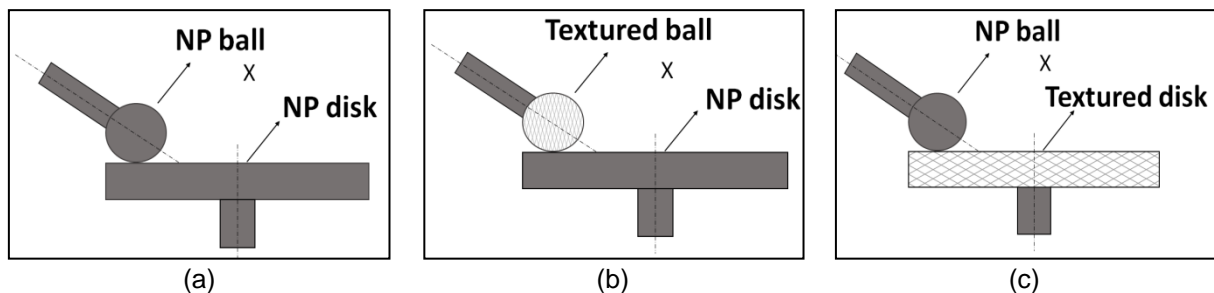


Figure 4.5 – Schematic representation of test configurations. (a) Reference bench pair NP x NP, (b) textured balls x NP disk and (c) NP ball x textured disk.

- Film thickness** measurements were carried out by the optical interferometry technique, using the EHD1 rig (PCS Instruments London), see Figure 4.6a. A steel ball is loaded against a glass disk and a white light is emitted on the contact between the bodies, as showed in Figure 4.6b. Part of the light passing through the glass disk is reflected by a thin Cr layer at the bottom of the disk and another part is reflected by the steel ball after passing through the SiO<sub>2</sub> spacer layer and the thin lubricant film. After that, the two light beams are recombined using a beam splitter, focused on a spectrometer and captured by a white CCD (Charged Coupled Device) camera. It is possible to determine the central film thickness measuring the light wavelength using the spectrometer. More details about the principles of optical interferometry could be found in the literature [79–81].

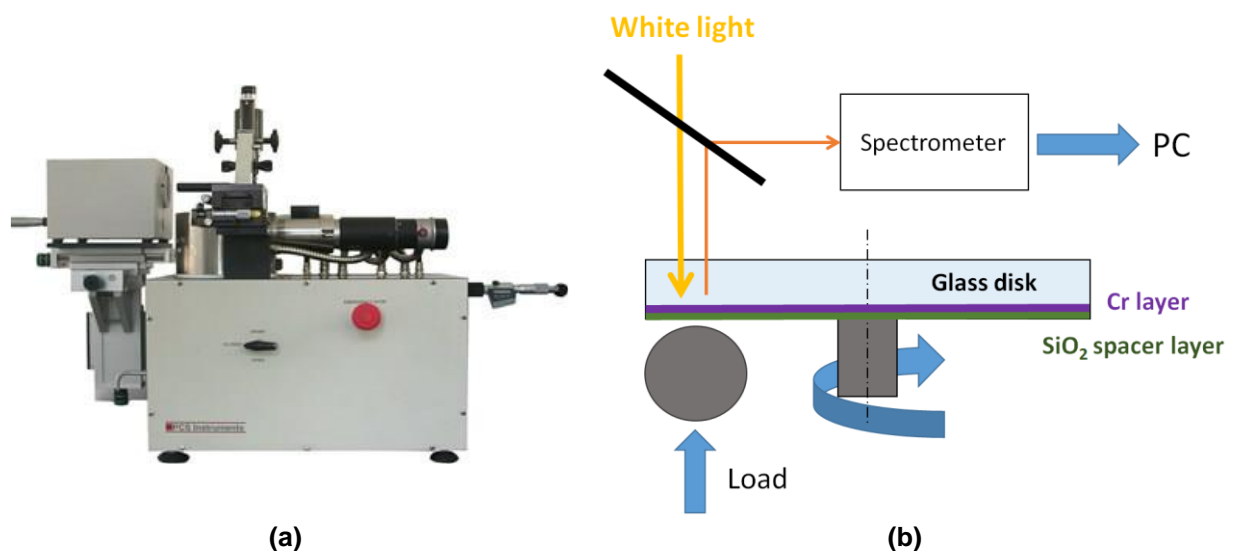


Figure 4.6 – (a) EHD1 tribometer [74] and (b) details of the configuration of ball on disk using the spectrometer.

The spectrometer permits to determine only the central film thickness, however it is possible to use a RGB (red, green and blue) colour camera to grab high resolution images of the whole contact. This more complex and accurate technique is named Spacer Layer Imaging Method (SLIM). PCS software is used to calibrate the system and produce a film thickness map of the whole contact. The EHD1 tribometer of PCS uses a white light source for the SLIM. However a brighter light (two led sources) is necessary for rough surfaces, as explained in [106,107]. The EHD1 used in this study is available at Imperial College London (UK) and it was modified by Dr. Johan Guegan during his PhD to enhance film thickness measurement of rough surfaces [108]. The modifications mainly consist in improving both the acquisition system and

the light source to extend the range of film thickness measurement. Furthermore, a custom-made MatLab® program was developed to analyse the interferograms and obtain film thickness profile, area and also the solid-to-solid contact (%). The reader is referred to Guegan's publications and thesis [106–108] for a full description of the technique and experimental set-up. This novel technique was applied to rough surfaces produced by lathe machining in [106,107] and it is now applied for the first time on sintered and textured samples in this research.

Sintered and textured balls were tested against glass smooth disks and the obtained results were compared to those of a smooth steel ball (NP). The tests were conducted using the parameters summarized in Table 4.2. SRR variations presented limited effects on film thickness [106,107,109], therefore only pure rolling (SRR 0%) was evaluated using EHD1 rig, see Table 4.2.

Material type and applied load for friction and film thickness evaluation assume different values, see Table 4.2. Lubricant film measurements could be used for conditions tested in MTM2 rig through a transformation based on Hamrock-Dowson equation [75]:

$$\frac{h_{MTM2}}{h_{EHD1}} = \left( \frac{E^*_{EHD1}}{E^*_{MTM2}} \right)^{0.073} \times \left( \frac{W_{EHD1}}{W_{MTM2}} \right)^{0.067} = 0.99 \quad (11)$$

Where  $h$ ,  $E^*$  and  $W$  represent respectively film thickness, composite elastic module and load used for EHD and MTM rig. This analysis made it possible to obtain film thickness values of metal-to-metal contact ( $h_{MTM}$ ) for specific speeds based on measurements conducted on EHD1 ( $h_{EHD}$ ). Furthermore, friction response (MTM2 rig) could be evaluated in term of specific film thickness values ( $\Lambda$ ).

Film thickness was measured for textured balls, since a plain steel disk could not be used for interferometry measurements. NP balls were used as reference bench material for friction tests.

The contact diameter (Hertz theory) was around 170  $\mu\text{m}$  for MTM2 tests and around 270  $\mu\text{m}$  for EHD1 rig.

Both MTM2 and EHD1 require standard dimensions samples. Standard steel samples (NP) were purchased at PCS Instruments London, see Figure 3.6. Surface texture was applied on NP smooth samples as explained in Section 2.3.

## 4.5.2 Results and discussion

This section focuses on frictional response rather than wear behaviour, since the load applied for tribological tests did not cause significant surface modification and wear. Textured balls results (see configuration in Figure 4.5b) are presented first, followed by textured disks configuration (see Figure 4.5c). Finally, wear and surface analysis after testing are also reported.

- **Textured balls X NP disk**

Variation of entrainment speed ( $U_e$ ) and sliding-rolling conditions (SRR) during tribological tests permitted to obtain a friction surface response, also defined as traction map. The coefficient of friction (COF) could be traced as a function of  $U_e$  and SRR, as depicted in Figure 4.7.

Traction maps were displayed with the same scale and colour map to facilitate comparisons between different configurations, see Figure 4.7. Differences can be noticed at low entrainment speed ( $U_e$ ), especially between NP and longitudinal grooves BLG1 and BLG2 (see Figure 4.7a, c and d). In general, dimples (BD) and perpendicular grooves (BPG) decreased friction compared to NP at low SRRs and  $U_e$ , whereas longitudinal grooves configurations (BLG1 and BLG2) seemed to present detrimental results. All samples behaved similarly in the plateau region (dark blue), presenting a friction coefficient of approximately 0.03.

Traction maps enhance general comparisons between different configurations and permit to detect in which operational conditions friction reduction is achieved. However, a more detailed analysis is required to quantify and better visualize frictional behaviour in different lubrication regimes. For these reasons, COF was depicted varying  $U_e$  and maintaining fixed the SRR, see Figure 4.8. This curve response is also known as “Stribeck like” due to similarities with Stribeck curves, see Figure 4.1. Four SRRs conditions ranging from prevalent rolling (SRR 20%) to prevalent sliding (SRR 180%) were selected to accurately assess texture frictional behaviour, see Figure 4.8.

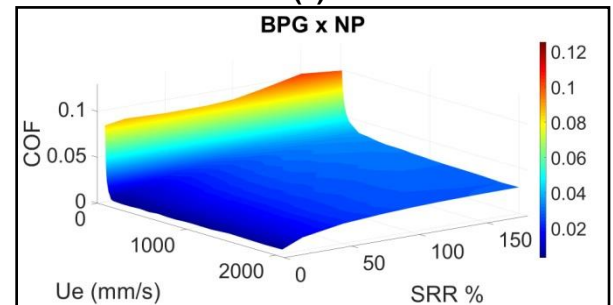
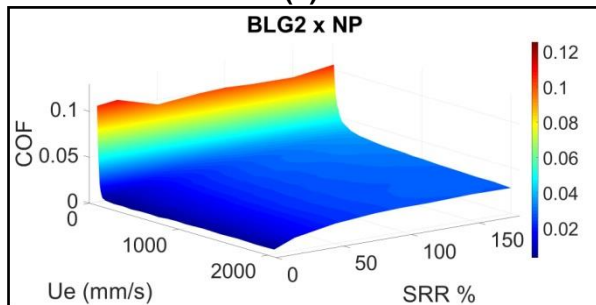
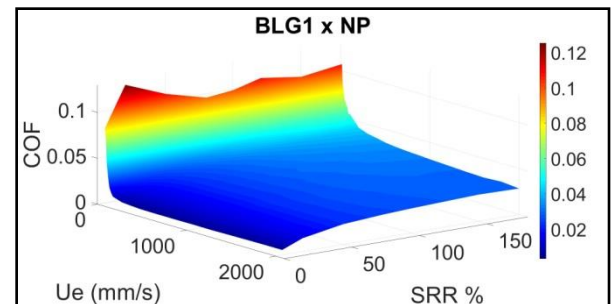
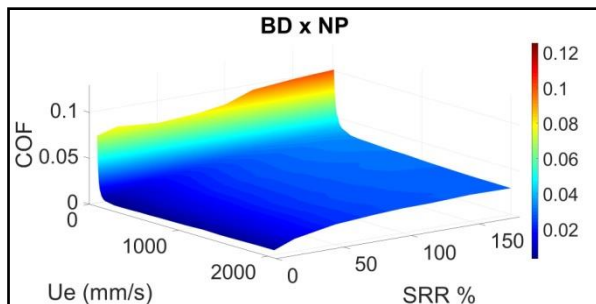
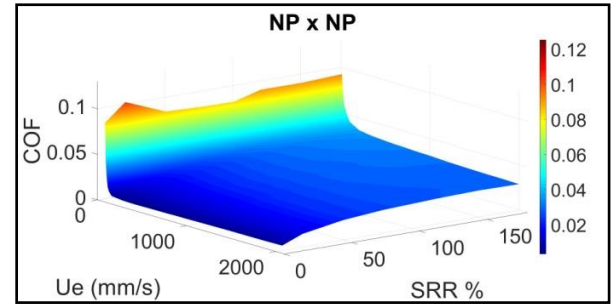
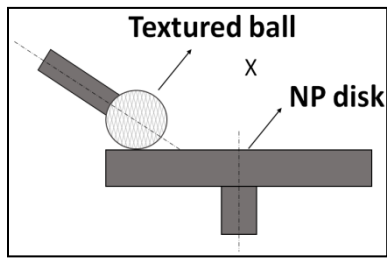


Figure 4.7 – COF surface response (COF x  $U_e$  x SRR) of (a) NP and (b), (c), (d), (e) textured balls (BD, BLG1, BLG2 and BPG) tested against NP disks.

Textured and smooth configurations exhibited same friction at high speeds (higher than 600 mm/s), presenting COF of approximately 0.03 for all SRR conditions. Friction differences became more significant for lower speeds. For instance, longitudinal grooves (BLG1 and BLG2) increased significantly friction compared to NP in this region. Worse results were presented by less dense configuration BLG1, see Table 3.4 and Figure 4.8. Perpendicular grooves (BPG) generally behave similarly to NP material. In particular, BPG performed slightly better than NP for SRR 20% and worse for SRR 180%. Furthermore, BPG reduced friction compared to longitudinal feature as expected (see Table 4.1). Finally, dimple configurations (BD) presented best frictional response especially for low speeds (below 100 mm/s). SRR

variation seemed to have a slight effect only on BPG behaviour, whereas the trend for other configurations remained unchanged as SRR varied.

It is difficult to determine and quantify friction reduction in a specific region by simple inspection of “Stribeck like” curves in Figure 4.8. Thus, percentage differences in friction were evaluated using as a bench mark NP results. Friction variation (*Delta friction*) was defined as:

$$\Delta friction \% = \left( \frac{COF_{Texture} - COF_{NP}}{COF_{NP}} \right) \times 100 \quad (12)$$

where friction reductions assume negative values of *Delta* and  $COF_{Texture}$  represents friction response for textured balls. *Delta* values were calculated for every speed and plotted as “Stribeck like” curves (fixed SRRs), see Figure 4.9.

Observing Figure 4.9, the results highlighted in Figure 4.8 become now more evident. For instance, longitudinal grooves BLG1 increased friction of 30-40% and up to 50-60% for SRR 20%. At high speeds, BLG1 still presented small friction increment, whereas all other configurations behave as NP. On the contrary, significant differences were encountered for lower speeds (below 600 mm/s). Friction response presented different results depending on the lubrication regime, however a more in depth analysis is required to better identified speed ranges of lubrication regime.

Dimples (BD) promoted best friction reduction in all SRRs, obtaining decrements up to 20%, especially for speed close to 100 mm/s. BLG2 configuration generally increased friction (15-20%), especially for harsher test conditions (SRR>50%). BPG configuration ranged from small reductions ( $\approx 10\%$ ) to small increments ( $\approx 10\%$ ) with the increase of SRR.

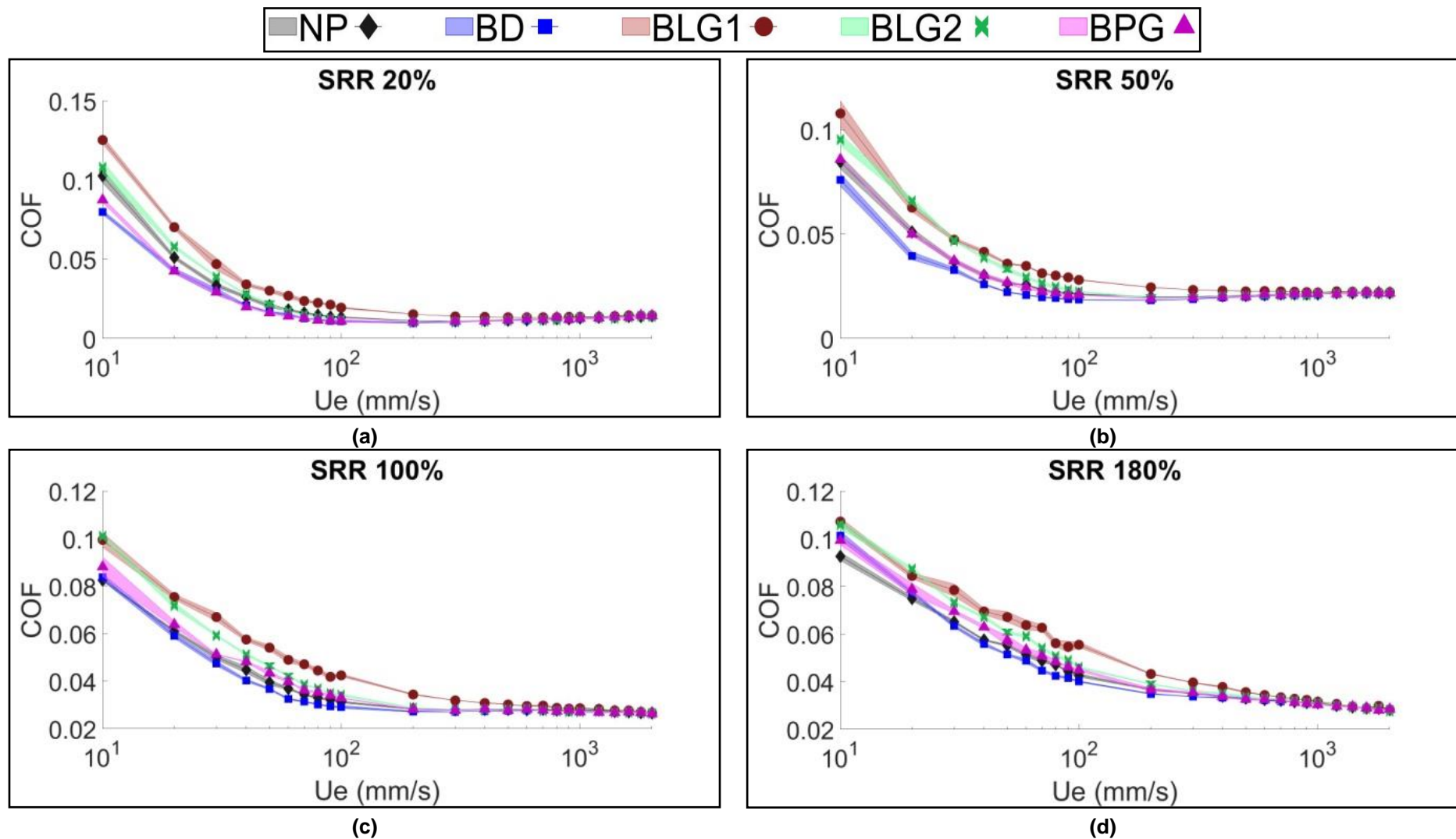


Figure 4.8 – “Stribeck like” curves for textured and NP balls tested using (a) SRR 20%, (b) SRR 50%, (c) SRR 100% and (d) SRR 180%. The horizontal axis is in logarithmic scale.

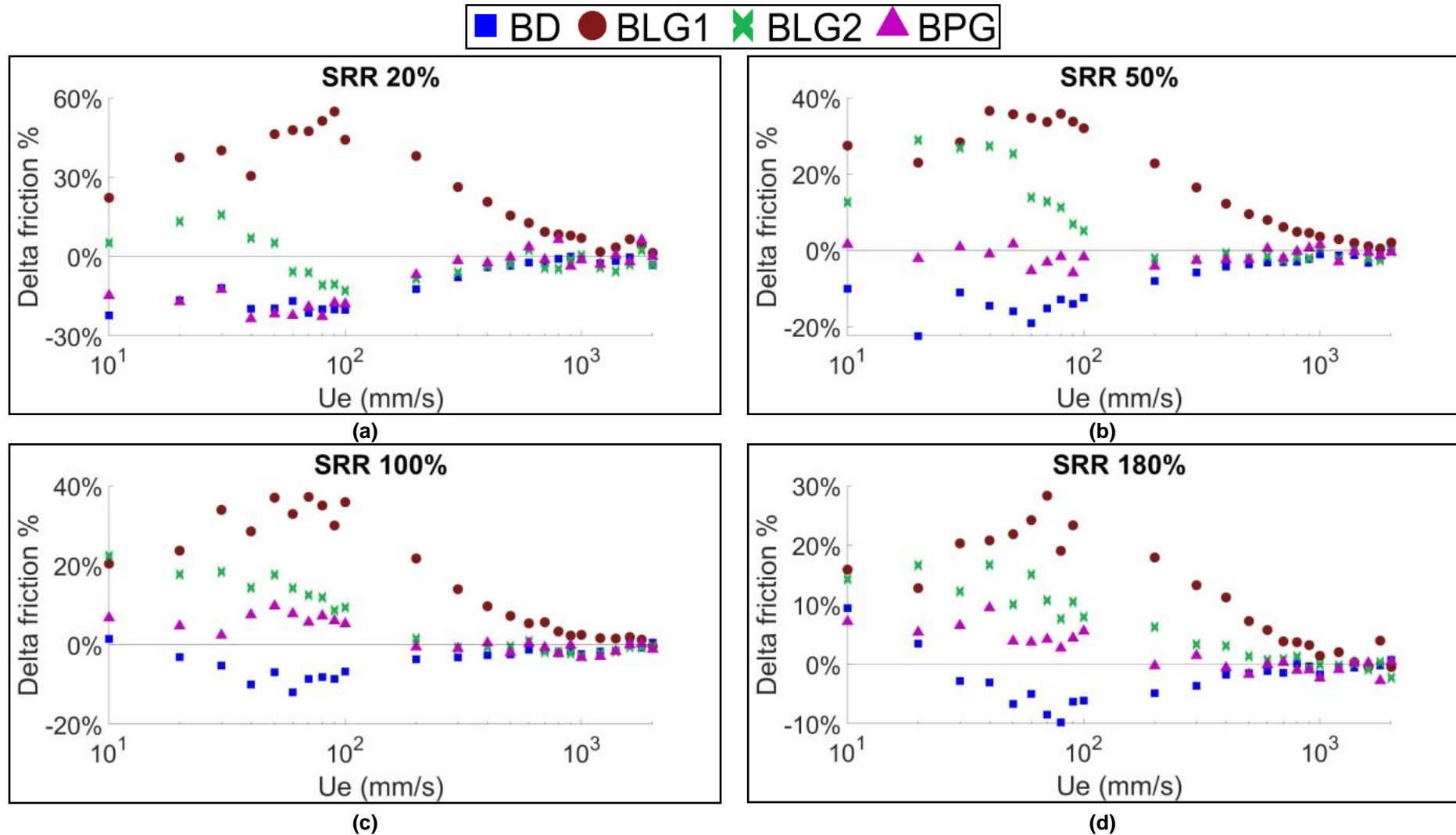


Figure 4.9 – *Delta friction %* for textured and NP balls tested using (a) SRR 20%, (b) SRR 50%, (c) SRR 100% and (d) SRR 180%. The horizontal axel is in logarithmic scale.

Film thickness was evaluated for ball samples for determining texture effects on friction and lubricant regime variations. Images of the lubricated contact (also known as interferograms) for different entrainment speeds were collected in Figure 4.10. The inlet position is on the left side, whereas the outlet is on the right. The evolution of film thickness could be evaluated for increasing entrainment speeds (from 0.02 m/s up to 2.2 m/s).

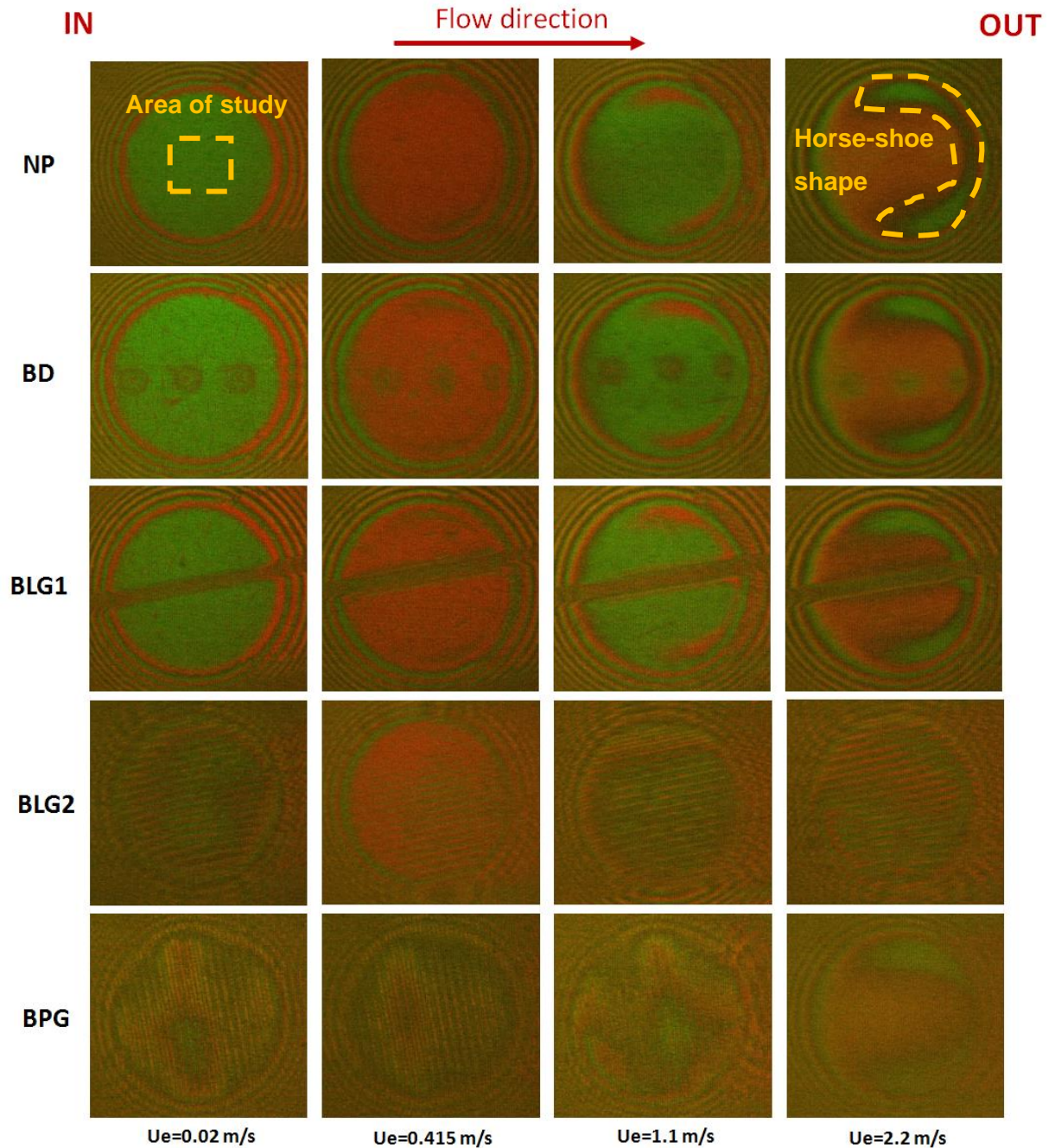


Figure 4.10 – Images of lubricated contact using different entrainment speed ( $U_e$ ) for NP and textured (BD, BLG1, BLG2 and BPG) balls.

Different film thickness produced colour variations in the interferograms as explained in [79–81]. Classical EHL film distribution is composed by a flat central region (Hertz theory) with a horse-shoe shape in the outlet for high entrainment speeds [110]. Horse-shoe shape became visible at  $U_e=1.1$  m/s for smooth samples (BD, BLG1, NP), however it is difficult to be identified in rougher samples (BLG2 and BPG) even at high speed ( $U_e=2.2$  m/s), see Figure 4.10. The horse-shoe represents a film constriction region caused by the rapid pressure drop between central contact (high pressure) and exit region (atmospheric pressure). The pressure fall causes an exponential viscosity drop, thus film thickness must decrease in the outlet region to maintain flow continuity. The horse-shoe shape is less visible for rougher configurations (BLG2 and BPG), since the real contact area was much lower ( $f=47\%$ ) than smooth surfaces, see coverage area  $f$  in Table 3.4.

The central area of contact was selected for more detailed analysis, see Figure 4.10. The custom made program for film thickness measurements permitted to obtain maximum and minimum film thickness values. Minimum values could be used for precisely identified lift-off speed ( $l_f$ ). In particular, minimum film thickness greater than zero implied absence of asperity contact and consequently full-film lubrication condition (EHL). Minimum film thickness and  $l_f$  speeds for textured balls were shown in Figure 4.11.

Dimple configuration promoted EHL for lower speed ( $l_f=311$  mm/s) compared to perpendicular grooves ( $l_f\approx 415$  mm/s). Longitudinal grooves “delayed” the transition from mixed to full film up to approximately 600 mm/s. The  $l_f$  trend was similar to those encountered for friction response, see Figure 4.9. Dimples reduced both friction and  $l_f$  speed, see Figure 4.9 and Figure 4.11. For these reasons, BD seemed to increase load carrying capacity (micro bearing effect), especially in mixed lubrication regime.

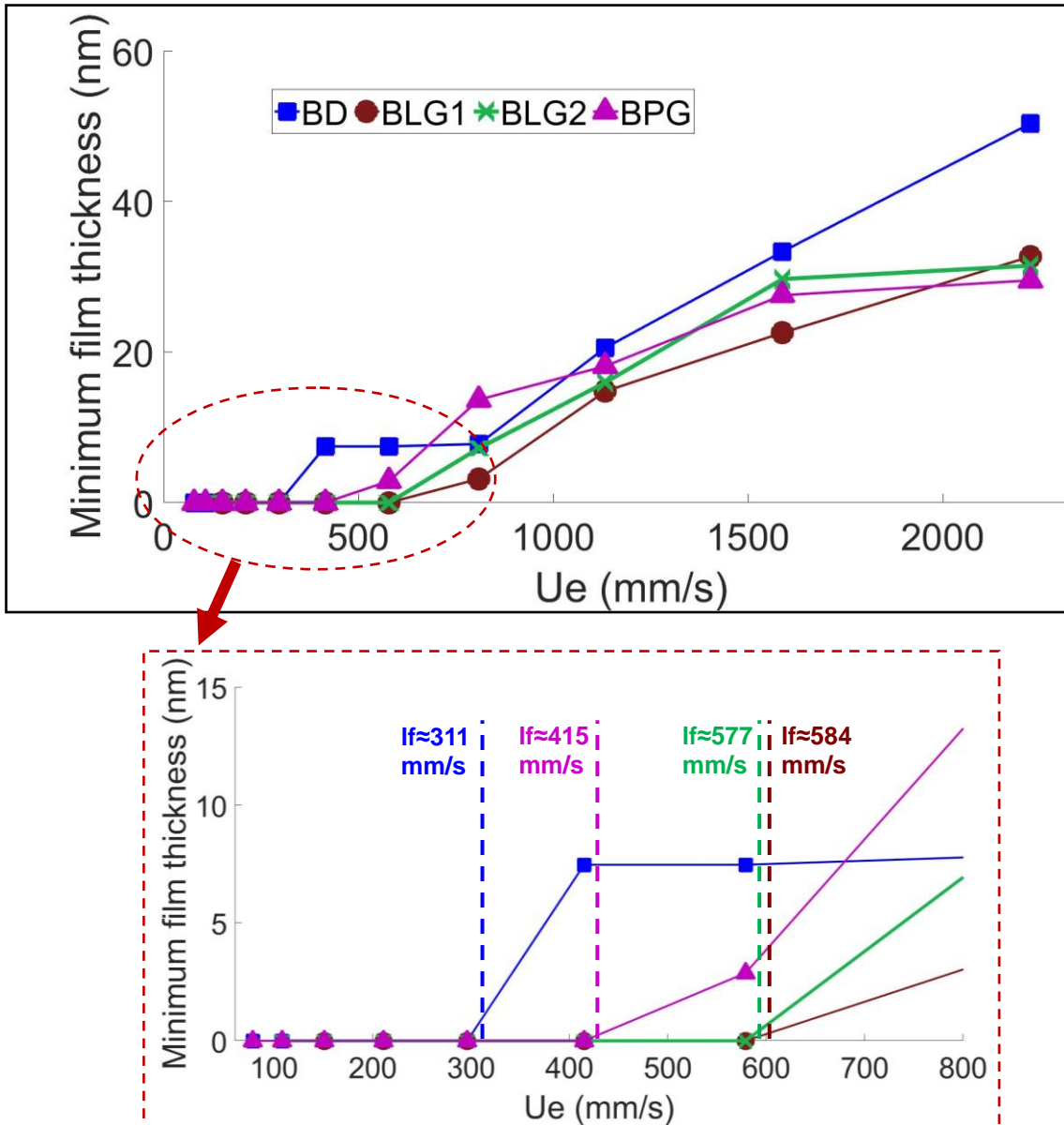


Figure 4.11 – Measured minimum film thickness for different textured balls varying entrainment speed (from 10 to 2200 mm/s) and pure rolling. Details of low speed region (below 800 mm/s) and lift-off ( $l_f$ ) speeds values (vertical dashed lines).

Perpendicular grooves slightly increased friction and  $l_f$  speed compared to dimples (Figure 4.9 and Figure 4.11), even presenting similar geometrical characteristics (Table 3.4). This could be caused by perpendicular extension of grooves which was approximately 1 mm. Considering a contact diameter of 170  $\mu\text{m}$ , transversal dimension of grooves was much larger than contact diameter. For these reasons, local increment of pressure close to perpendicular features could be attenuated by transversal flow of lubricant within the grooves, see Figure 4.12c. For dimple configuration lubricant squeeze is less probable, since the diameter of the micro cavities is smaller than contact dimensions, see Figure 4.12a. Grooves were not

entirely contained within the contact, therefore lubricant could flow out the contact zone. This behaviour is common for longitudinal grooves, where lubricant flow and groove have the same direction [5,9], see Figure 4.12c.

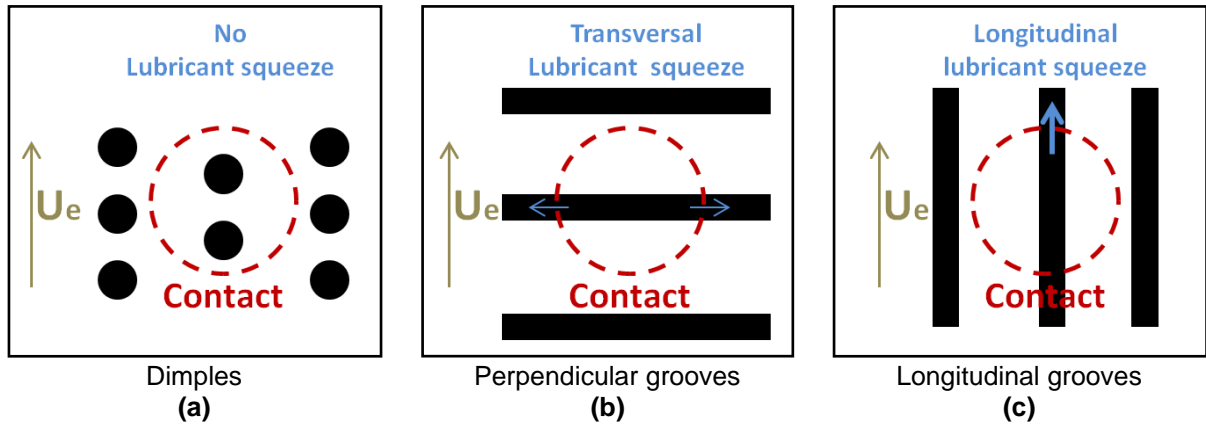


Figure 4.12 – Schematic representation of lubricant squeeze in (a) dimples, (b) perpendicular and (c) longitudinal grooves configurations.

Finally, the percentage of solid-to-solid contact was evaluated using the custom made program for interferogram analysis, see Figure 4.13. The amount of asperity contact increased as speed reduced, passing from EHL to mixed lubrication. Asperity contact followed the same trend of friction results, being that longitudinal grooves presented higher values of solid-to-solid contact followed by perpendicular features and dimples. These results were analysed jointly with area coverage  $f$ .

Solid contact (%) of BLG1 was higher than BLG2, probably due to smaller area coverage values ( $f = 21\%$  and  $47\%$  respectively) and consequently, more material in contact. Both longitudinal (BLG2) and perpendicular (BPG) grooves produced by Nd:YAG laser presented coverage area  $f$  of approximately  $47\%$ . However, BPG showed less asperity contact for the low speed range, enforcing the hypothesis of more lubricant squeeze in longitudinal direction than on transversal, see Figure 4.12.

Dimple configuration, even presenting lower  $f$  values (more surface untextured), showed smaller amount of asperity contact and consequently reduced friction, see Figure 4.9 and Figure 4.13. These results corroborate with the hypothesis of micro bearing effects on lubrication. Converging regions in dimples increased local viscosity and lubricant pressure, raising load carrying capacity and preventing asperity contact. For these reasons, dimple configuration reduced friction in mixed regime, see Figure 4.9.

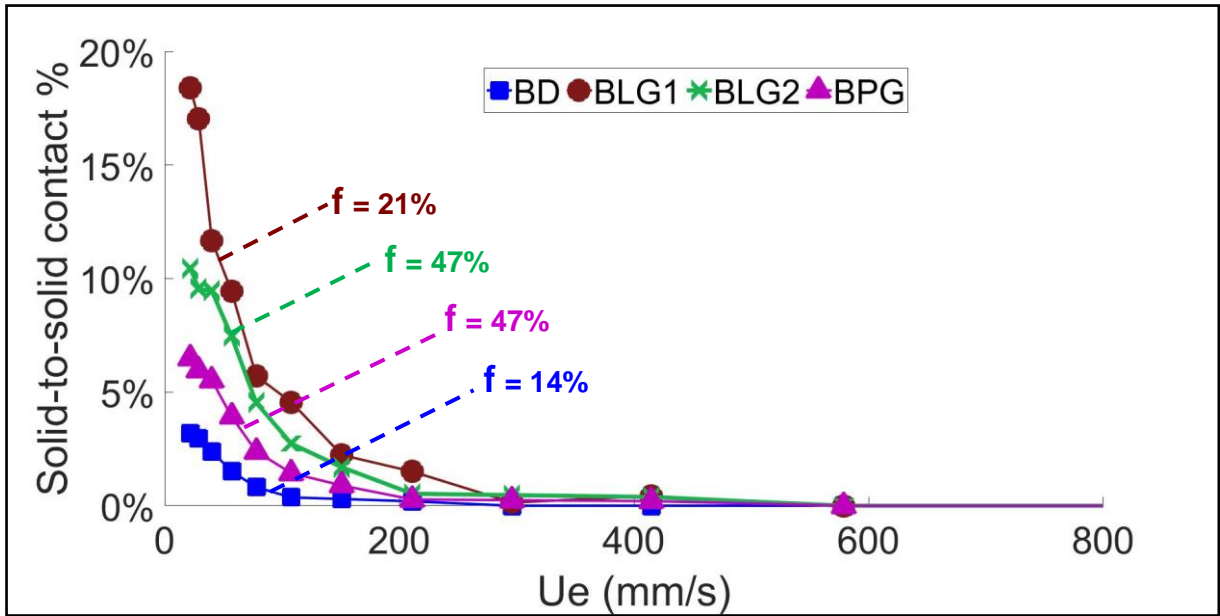


Figure 4.13 – Solid-to-solid contact (%) and area coverage values  $f$  (%) for textured balls (BD, BLG1, BLG2 and BPG). Values obtained using the custom made program for film thickness evaluations.

- **NP ball X textured disks**

Friction results of textured disks were scrutinized using “Stribeck like” curves for different SRRs, see Figure 4.14.

Similar to the ball configuration behaviour (see Figure 4.8), significant differences could be notice for lower speeds, whereas friction assumed same values for high speeds. Deep grooves configuration (DG2) increment significantly friction for all SRRs compared to NP. On the contrary, shallow grooves (DG1) promoted friction reduction, especially for smaller amount of sliding (SRR 20% and 50%). Dimple configurations showed best frictional performance for all SRRs considered in this study, see Figure 4.14.

Friction beneficial effects were better quantified using *Delta friction* values, see Figure 4.15.

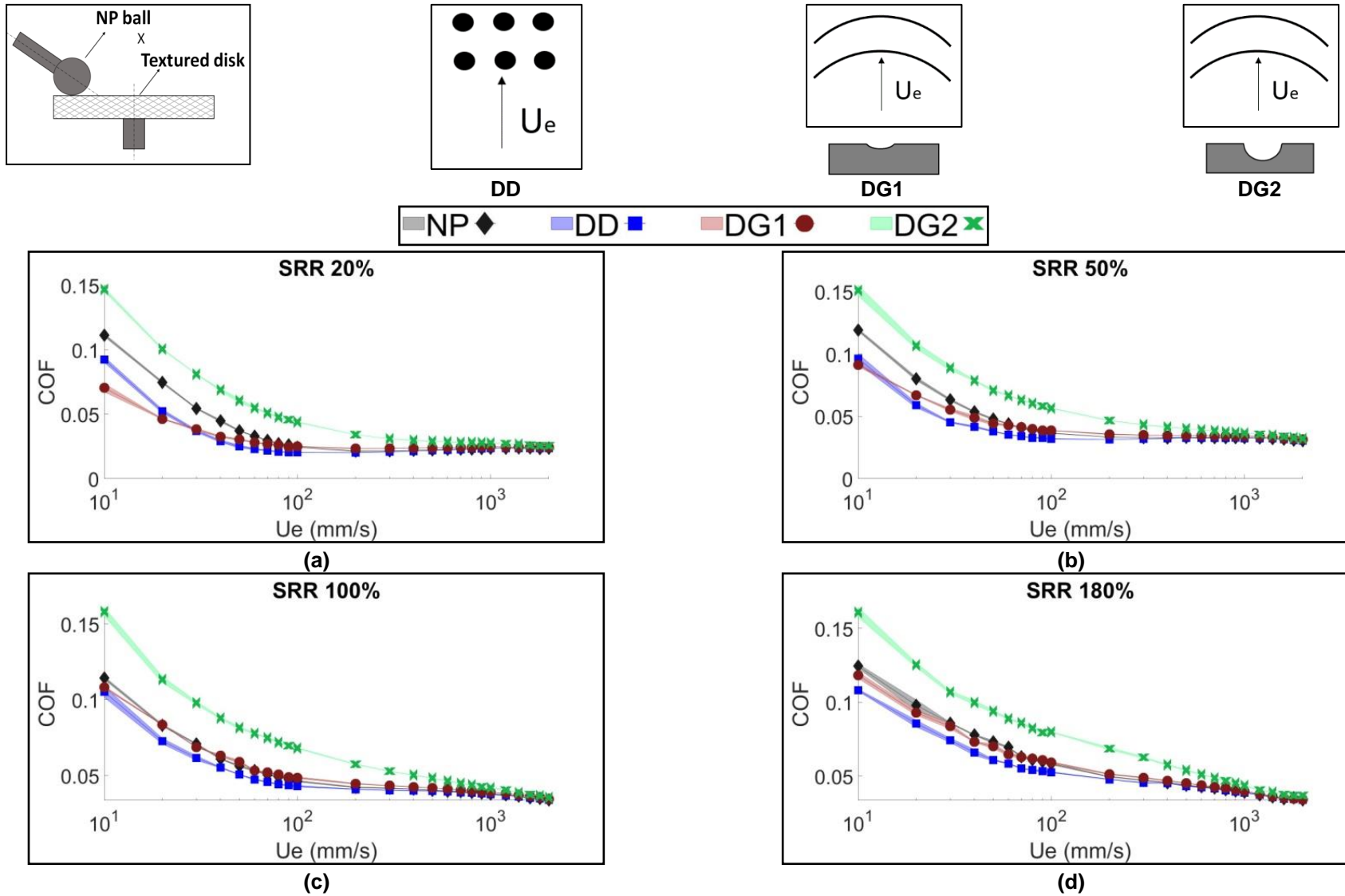
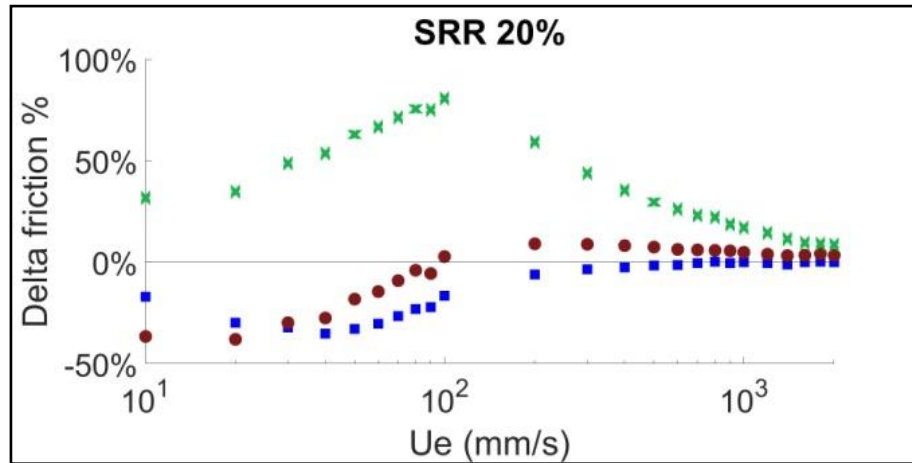
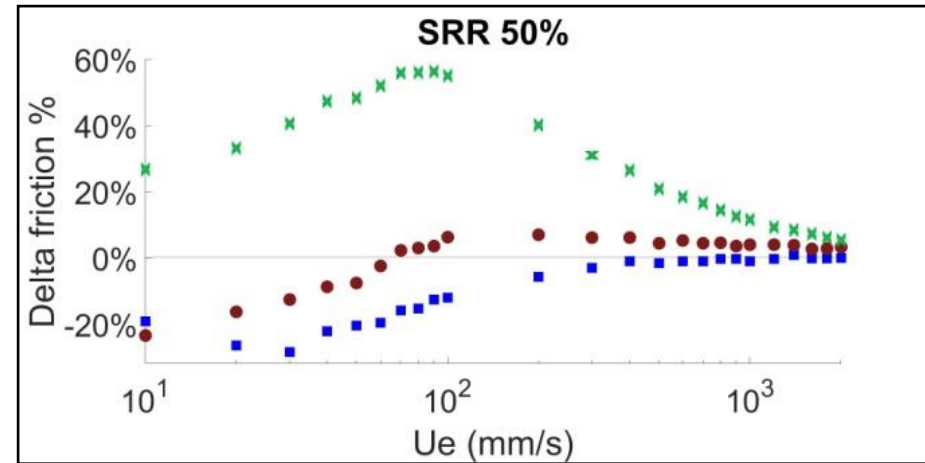


Figure 4.14 – “Stribeck like” curves for textured and NP disks tested using (a) SRR 20%, (b) SRR 50%, (c) SRR 100% and (d) SRR 180%. The horizontal axis is in logarithmic scale.

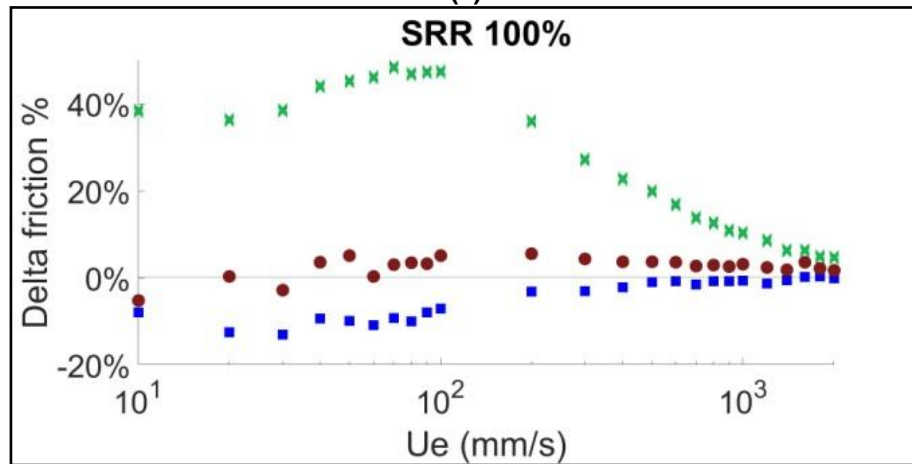
■ DD ● DG1 × DG2



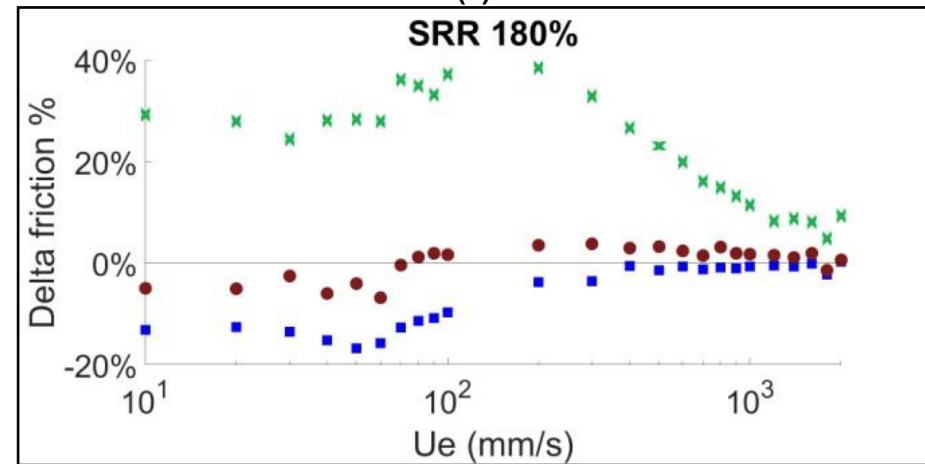
(a)



(b)



(c)



(d)

Figure 4.15 – *Delta friction %* for textured and NP disks tested using (a) SRR 20%, (b) SRR 50%, (c) SRR 100% and (d) SRR 180%. The horizontal axel is in logarithmic scale.

Shallow configurations (DD and DG1) had similar friction response of NP material from high speed up to approximately 100-200 mm/s. Deeper feature DG2 presented higher friction even for high speeds (close to 2000 mm/s). Beneficial effects of shallow textures were intensified for mild test conditions (SRR<50%). Particularly, DD promoted friction reduction lower than 20% for SRR 180% (high sliding) and up to 40% using SRR 20% (low sliding). Similarly, DG1 behave as NP for harsh conditions (SRR>100%) and it promoted friction reduction for low speed in mild test conditions (SRR<50%), see Figure 4.15. DG2 significantly increment friction (around 50%) when compared to NP.

Shallow configuration (DD and DG1) brought beneficial effects in term of friction reduction. Shallow features could increment local pressure and viscosity, inducing film thickness raise, as reported in [48,95,111]. On the contrary, deep cavities (DG2) led to detrimental results in all conditions, enforcing the importance of texture depth for non-conformal contact. Deep surface valleys could cause local viscosity and pressure drops, therefore lubricant could not provide a sufficient film for avoiding asperities contacts [48], see Figure 4.16. Furthermore, film thickness evaluated through Hamrock/Dowson equation [75] were between 50 and 400 nm varying entrainment speed. These values were similar to cavity depth in shallow configurations (<0.5  $\mu\text{m}$ , see Table 3.3), whereas surface cavities in DG2 samples were much deeper than film thickness (> 1  $\mu\text{m}$ ). Cavities presenting the same depth magnitude of film thickness could potentially promote lubricant film built-up, however deep cavities seemed to promote film breakdown, consequently increasing solid contact and friction, see Figure 4.16.

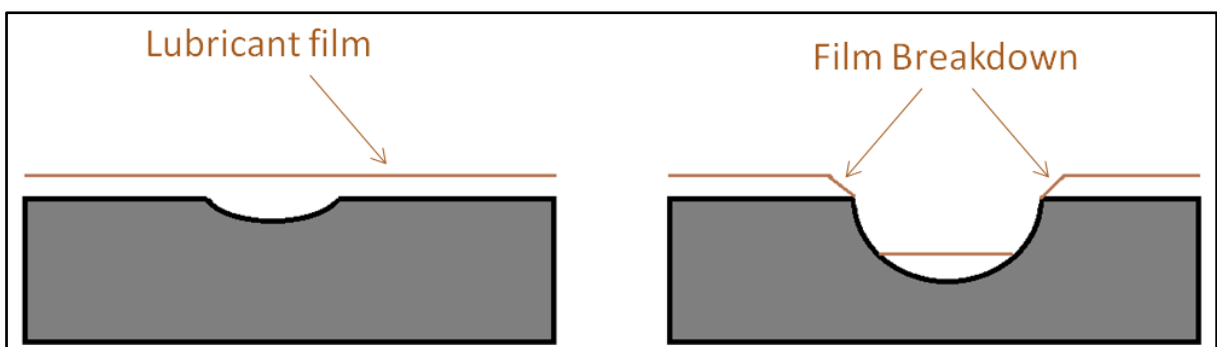


Figure 4.16 – Lubricant film formation using shallow (< 0.5  $\mu\text{m}$ ) and deep (> 1  $\mu\text{m}$ ) feature configurations.

Although DG1 covered much more area than DD ( $f=1\%$  and  $12.5\%$  respectively, see in Table 3.3), dimples performed better results (see Figure 4.15). Similarly to ball texture, this behaviour could be caused by transversal dimensions on grooves, possibly enabling lubricant lateral flow, see Figure 4.12.

ECR measurements were used to define lift-off ( $l_f$ ) speeds, since interferometry measurements of film thickness are not possible for plain steel disks. COF and ECR results were plotted jointly to visualize texture influence on lubrication regime transitions, see Figure 4.17. The results using SRR 120% were used as examples, being that the other test conditions presented similar ECR trends.

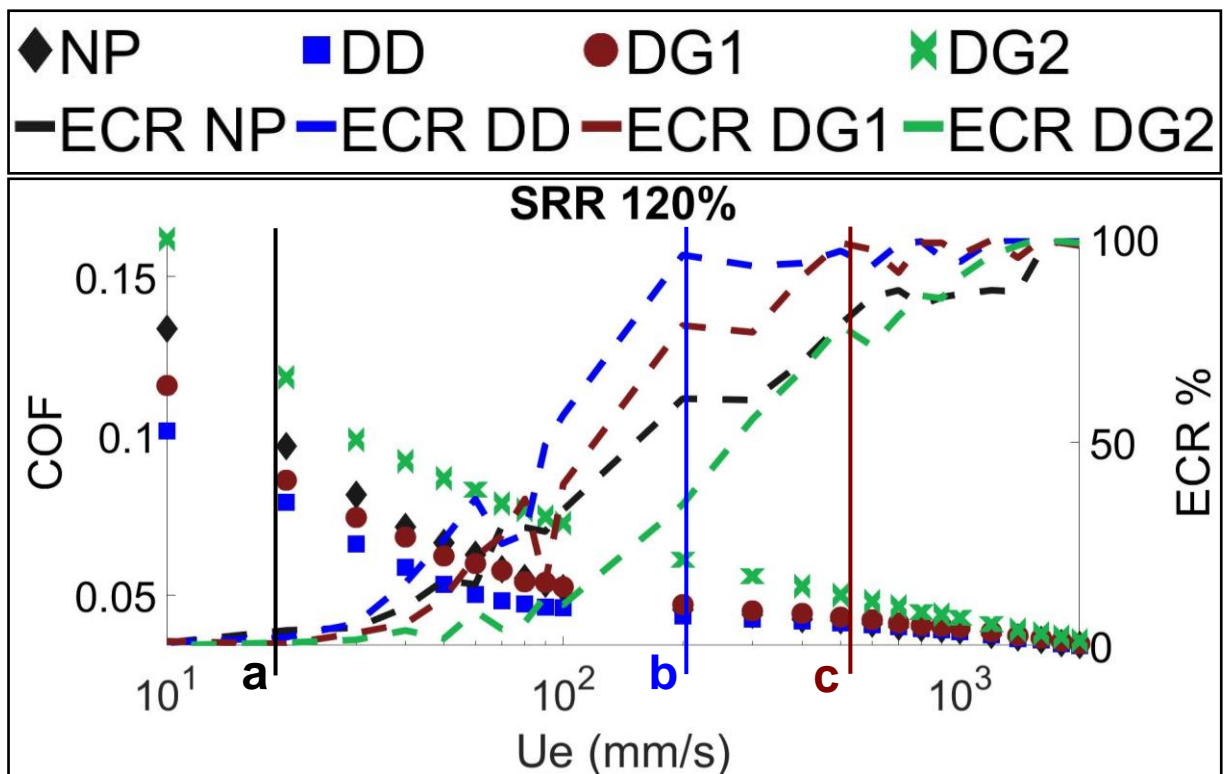


Figure 4.17 – COF  $\times$   $U_e$  (left vertical axis) and ECR  $\times$   $U_e$  (right vertical axis) for 120%, NP and textured disks.

EHL and boundary lubricant regimes were discriminated by respectively 100% and 0% of ECR values, as explained in Section 4.5.1. Dimples decreased  $l_f$  speed compared to smooth samples (NP), see vertical line 'b' in Figure 4.17. It seemed that dimples increased load carrying capacity in mixed lubrication, promoting friction reduction (see Figure 4.15) and anticipating EHL regime. DG1 decreased  $l_f$  speed (line 'c' in Figure 4.17), having an intermediate values between NP and DD. Grooves configuration behaved similarly to dimples, however with more attenuate effects (both

in term of friction and If reduction). Reasons for that were evaluated in previous paragraphs. NP and BG2 were generally under mixed and boundary conditions. The transition from mixed to boundary happened at almost the same speed for all configurations, see line 'a' in Figure 4.17.

- **Wear**

Materials did not wear out significantly, since wear rate was not measurable using a precision balance (resolution of  $10^{-4}$  g) or 3D optical interferometry. However, surface topography of wear track was measured to quantify texture geometry and surface roughness alteration after testing. Dimple configuration on disk (DD) samples is depicted in Figure 4.18 as example. The other texture configurations did not present any relevant topographic alteration after testing.

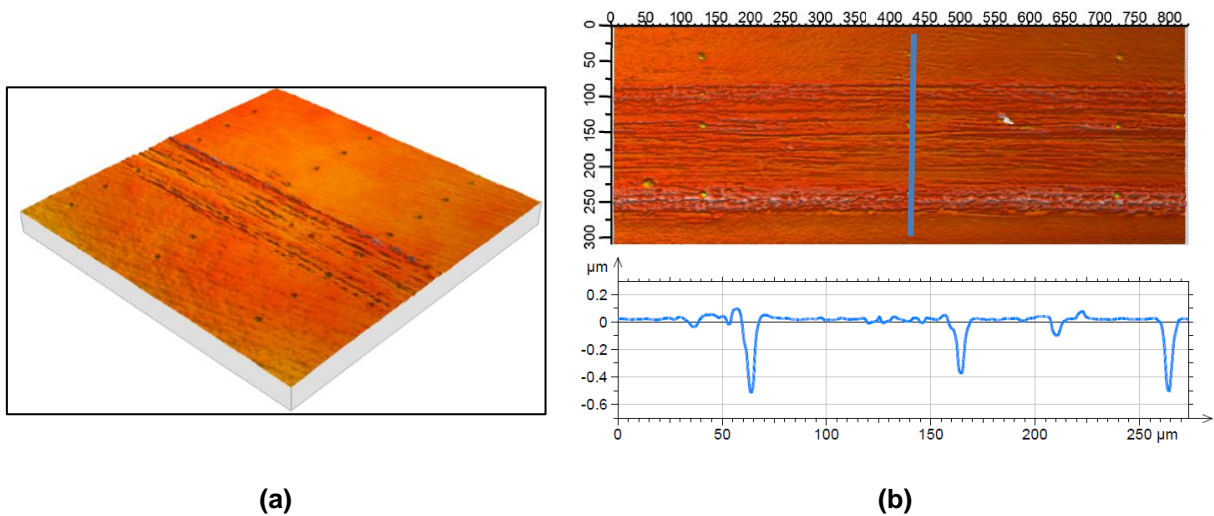


Figure 4.18 – (a) 3D surface image (800 μm x 800 μm) of wear track on dimple textured disk (DD). (b) Detailed view of the wear track and representative 2D profile along a row of dimples.

Surface micro scratches after testing did not affect dimples geometry, see Figure 4.18. Moreover, surface roughness was not affected and ball samples did not present significant topographic alterations.

## 4.6 Conclusions and final remarks of the chapter

Literature review and tribological experimental results of surface texture were explored within this chapter. Two different texture configurations (dimples and grooves) were applied both on ball and disks specimens. The following conclusion could be done:

- Design parameters for surface texturing should consider operational conditions and material properties. Each texture configuration is designed for a specific application.

From the experimental results and the texture configurations studied:

- The surface textures studied did not influence full-film regime, except for detrimental results (DG2 and BLG1). On the contrary, texture effects were significant in boundary and mixed lubrications.
- Shallow configurations generally improved tribological performance compared to deeper ones due to micro bearing effects;
- Dimples were more efficient than perpendicular grooves probably due to feature dimensions. Excessive transversal dimension of grooves could promote lubricant lateral flow and consequently the attenuation on local pressure increment;
- Dimples decreased lift-off speed, promoting full-film conditions for lower speeds. Furthermore, friction presented lower values especially in mixed and boundary lubrication regimes. Even presenting less coverage area  $f$  (potentially higher area in contact), dimples promoted friction reduction possibly caused by the increase of lubricant load carrying capacity (micro bearings effect);
- Longitudinal grooves decreased friction compared to perpendicular features. Lubricant could easily flow within feature when entrainment speed and grooves presented the same direction. This effect avoided lubricant local built-in and incremented asperities contact, consequently increasing friction.

## **Chapter 5 Tribological studies of sintered material**

### **5.1 Introduction**

Tribological effects of textured micro features could be somehow applied to PM components, since surface pores represent surface irregularities with random distribution. However, sintered material is still poorly explored regarding tribological performances [15–17,60], probably due to negative effects of the pores on mechanical properties [64–66,112]. This chapter presents literature studies regarding surface porosity effects on tribological properties. The interest in studying tribological properties of PM seemed to be limited to boundary lubrication and pure sliding conditions [15–17,60]. However, several mechanical components operated under varying sliding-rolling condition, such as cam-tappet and gears applications. The lack of studies in this field boosted the interest in understanding the tribological effect of randomly distributed surface cavities under varying sliding-rolling and lubricant regime conditions. After a literature review, experimental studies developed are shown.

### **5.2 Tribological effect of surface porosity in PM materials**

Surface pores similarly to textured features could promote lubrication in severe conditions (lubricant reservoirs), reduce wear (debris trapping) and potentially increase lubricant local viscosity and hydrodynamic pressure (micro hydrodynamic bearing effect). Surface pores are randomly distributed and generally assumed an irregular shape (see Figure 5.1), therefore the micro bearing effect is plausible just for pores of reduced dimensions with regular rounded shape [23]. Furthermore, large porosity networks with connected porosity and irregular shape of surface pores could promote crack propagation for high contact pressure tests (HEHL).

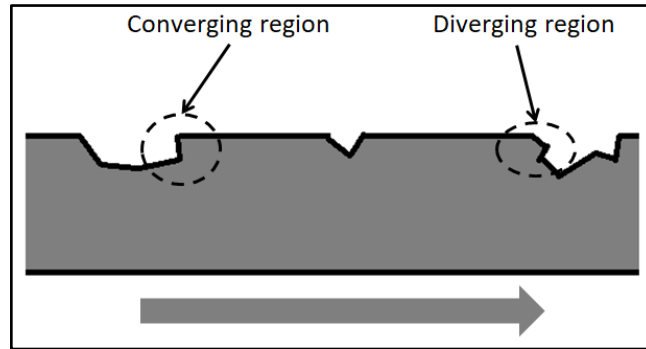


Figure 5.1 – Converging and diverging regions of surface pores in sintered materials.

Tribological studies of sintered materials were mainly related to sliding conditions of gear material during boundary lubrication regime [15–17,60]. Particularly, Martin and co-authors scrutinized the effect of porosity during self-lubricated tests under pure sliding tests [15]. The tests were performed under boundary lubricant and main results showed that the increase of porosity led to wear reduction. Pores acted as oil reservoir in boundary lubrication, enhancing lubrication in harsh conditions and consequently reducing wear. Similar behaviour was encountered for textured surfaces [95].

Li and co-authors [16,17,60] studied the tribological performance of sintered and wrought (non-porous) materials for gears application. They aimed at simulating the sliding portion of gear tooth contact under boundary lubrication. Main results showed that porous samples tested against wrought ones reduced friction when compared to same pair material (PM x PM, wrought x wrought). The increase of pores dimensions generally decreased friction and wear. Surface pores served as oil reservoirs and promoted heat exchange, favouring lubrication and limiting adhesive wear in boundary conditions. These results for boundary lubrication regime corroborates with those found by Martin [15].

Recent studies focused on tribological performance of sintered oil-impregnated gears [113,114]. The authors studied tribological effects of porosity during high load EHL lubrication. Main results showed that high porosity decrease elastic properties and surface load support capacity, causing excessive wear and closure of local pores [114]. Surface pore collapse avoids any beneficial effect on lubrication, as previously found by Boidi and co-authors [19,22]. Furthermore, Ebner and co-authors [113] verified that close porosity could improve lubrication rather than open one (connected network of pores). The increase of surface porosity generally increment surface

roughness values, since pores represent micro valleys. Surface pores could potentially improve tribological performance. However high porosity surfaces and large pores increased surface roughness, potentially having detrimental effect on lubrication. The importance of having a good balance between porosity and surface finishing was recently stressed by Ebner [113].

### **5.3 Experimental studies of sintered materials**

#### **5.3.1 Tribological testing**

The tribological tests for sintered materials were performed in three different configurations, pin-on-disk, roller-on-disk and ball-on-disk. Details of each testing configurations will be scrutinized in the following sections.

- **Pin-on-disk**

Pin-on-disk tests were performed using a UMT-2 Bruker tribometer with rotary configuration. A fixed pin was loaded against a rotating horizontal disk under pure sliding conditions, see Figure 5.2. The chromium steel (AISI52100) pin was 6 mm in diameter and presented flat surface in order to assess potential micro bearing effects of surface pores under conformal contact, see Figure 5.3. Disks sintered using SPS (D8, D9 and D10) were tested in this configuration. Conventional gear material (AISI 4320) was used to manufacture NP smooth disks. SPS disks were 20 mm in diameter due to manufacturing dimensional limitations (see Section 2.2.2), whereas NP much larger (75 mm in diameter), see Figure 5.3.

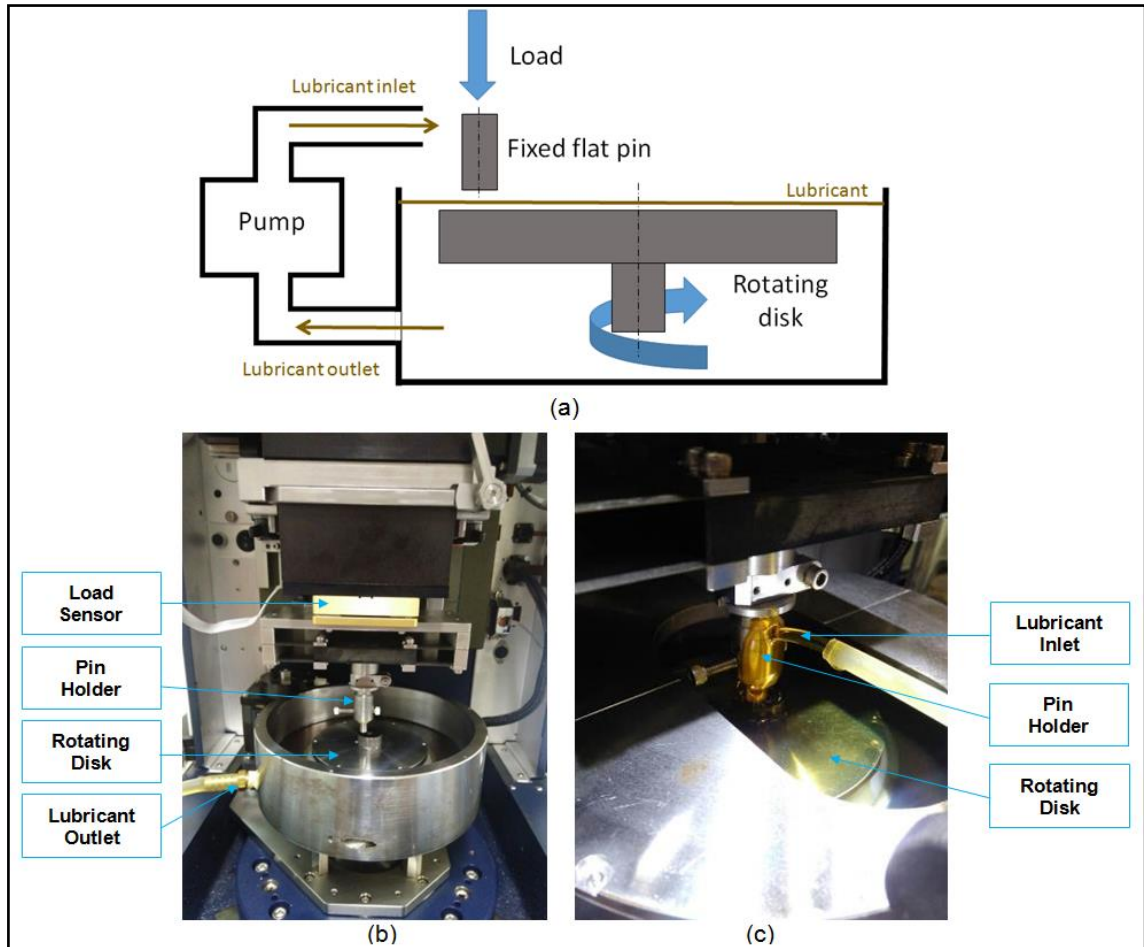


Figure 5.2 – (a) Schematic of Bruker tribometer for lubricated tests in the pin-on-disk configuration. Details of (b) tribometer and (c) test set-up configuration, adapted from [23].

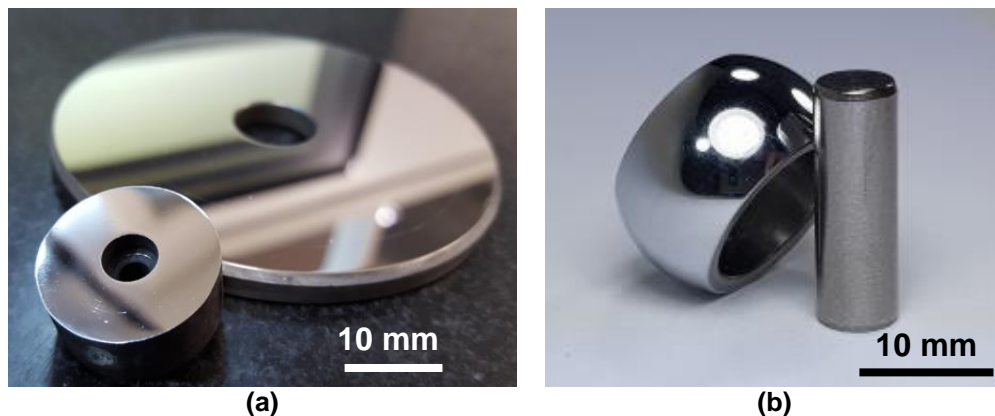


Figure 5.3 – (a) SPS sintered disk samples in the foreground and NP in the background [21]. Disk specimens were used both for pin-on-disk and roller-on-disk tests. (b) Counter-bodies, roller (non-conformal contact) on the left and flat pin (conformal contact) on the right side.

Synthetic transmission oil SAE 75W-85 was constantly pumped within the tribological contact, see Figure 5.2. The oil presented kinematic viscosity of  $220 \text{ mm}^2/\text{s}$  at test temperature ( $25 \text{ }^\circ\text{C}$ ). Entrainment speed and vertical load were

maintained constant during the tests for 15 minutes, see Table 5.1. A load cell applied vertical load and also measured tangential forces for friction calculation.

To ensure parallelism between the flat bodies (pin and disk) a running-in process prior each experiment was developed. Pins were loaded against a sandpaper arranged on disk surface. Low speeds and loads were used during this operation to avoid excessive pin wear. This procedure was repeated using sandpaper with progressive lower grit size until achieving a smooth flat pin surface parallel to disk.

Table 5.1 – Test parameters used for pin-on-disk tests

<b>Pin-on-disk configuration</b>	
Disk material	D8, D9, D10 and NP (AISI 4320)
Pin material	AISI 52100
Synthetic transmission oil	SAE75W-85
Entrainment speed, $U_e$ (mm/s)	1200
Slide-to-roll ratio, SRR (%)	200%*
Temperature (°C)	25
Mean contact pressure (MPa)	0.35 (10 N)
Kinematic viscosity (mm <sup>2</sup> /s)	220 (at 25 °C)

\*Pure sliding condition.

- **Roller-on-disk**

Roller-on-disk tests were performed using the same tribometer of pin-on-disk configuration with a custom-made device for SRR variations, see Figure 5.4. This device was proposed by [115] and allowed discrete variation of sliding-rolling conditions. SRR variations were obtained by changing angular speed direction on roller and horizontal disks, thus affecting local kinematics of roller-on-disk interface. The SRR device is composed of two shifting parts joined by a screw, being the upper attached to the tribometer and the lower hold the roller, see Figure 5.4. These parts can assume limited numbers of relative angular position between them depending on specific screw position. Tilt angle variation of roller and disk interface were induced by relative angular position between shifting device parts. As a consequence, roller tilt angle variation with respect to horizontal disks controlled SRR changes. It is possible to achieve only limited, discrete and positive values of SRR with this device. If the roller and the disk were driven independently, it would be possible to achieve continuous values of SRR, both positive and negative (see MTM2 rig in Section 4.5.1). The roller is driven by the disk and the entrainment velocity  $U_e$  is a result of the kinematic composition of velocity of the roller and the disk at the point of contact,

see [115]. The SRR validation occurred through kinematic evaluation and speed measurements (optical tachometer). The device effectiveness and reliability in term of SRR variations, along with additional information necessary to deeply understand the fundamentals surrounding the device operation, can be found in the same reference [115].

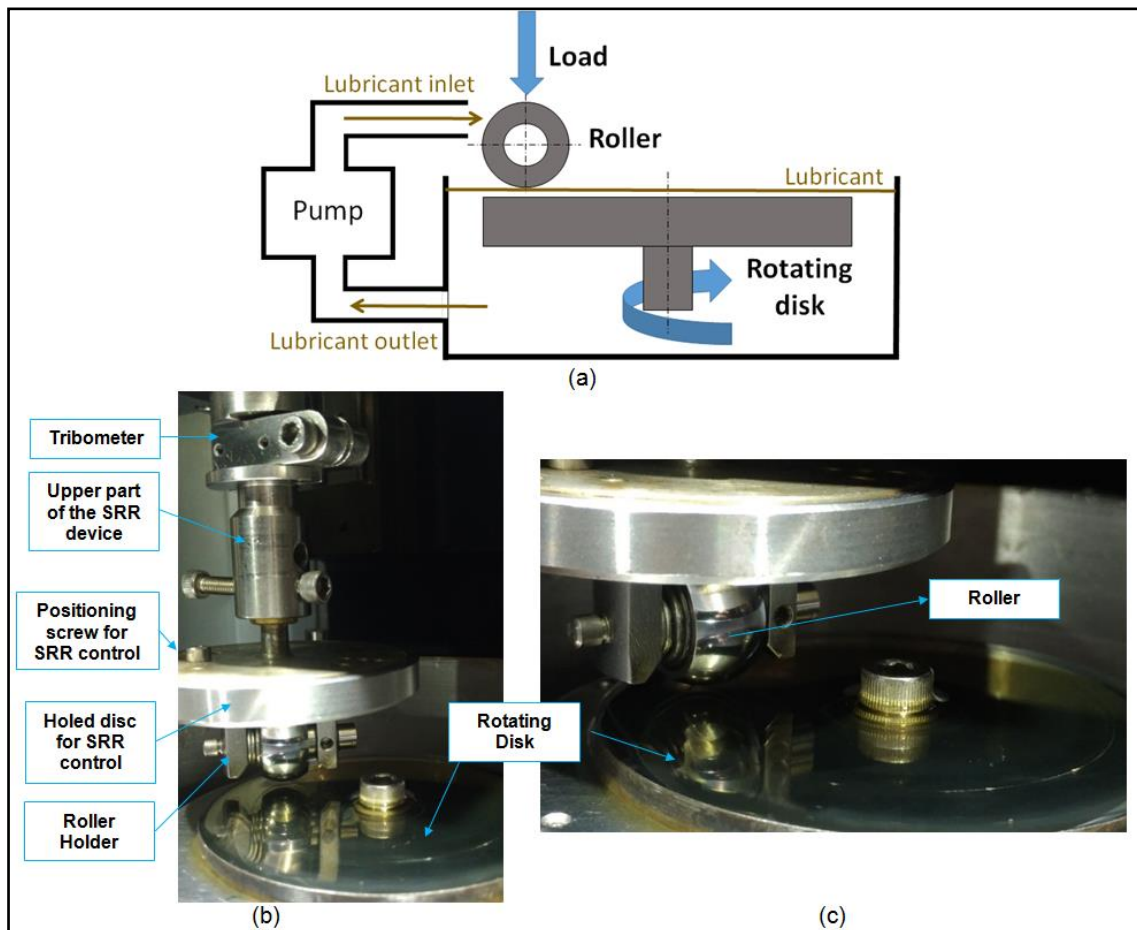


Figure 5.4 – (a) Schematic of Bruker tribometer for lubricated tests in the roller-on-disk configuration. Details of (b) SRR device and (c) test set up configuration, adapted from [21].

The disk samples and oil used for pin-on-disk tests were evaluated here. The counter-body was a chromium steel (AISI 52100) roller, see Figure 5.3 and Table 5.2.

Frictional tests were performed varying entrainment speeds to scrutinize surface pore effect during different lubrication regimes. Two SRR conditions were studied, being SRR 89% prevalent rolling and SRR 131% prevalent sliding ratio.

Table 5.2 – Test parameters used for roller-on-disk tests

Roller-on-disk configuration	
Disk material	D8, D9, D10 and NP* (AISI 4320)
Roller material	NP* (AISI 52100)
Synthetic transmission oil	SAE75W-85
Range of entrainment speed, $U_e$ (mm/s)	1050-10
Slide-to-roll ratio, SRR (%)	89% - 131%
Temperature (°C)	25
Contact pressure (GPa)	≈1
Kinematic viscosity (mm <sup>2</sup> /s)	220 (at 25 °C)

\*Note that non-porous reference material NP was different for disk and roller samples

### • Ball-on-disk

Disks sintered by conventional techniques (D4, D5 and D6) and SPS balls (B8, B9 and B10) were tested in this configuration. NP standard samples (PCS Instruments London) of chromium steel (AISI 52100) were used as reference bench. Sintered disks and balls were manufactured adopting samples standard dimensions required for the rig (disks: 46 mm in diameter and 6 mm in thickness; balls: 19.05 mm (3/4") in diameter).

Ball-on-disk configuration was evaluated by the same procedure used for textured materials (see Section 4.5.1). Particularly, coefficient of friction was measured using MTM2 rig and film thickness by EHD1 (see Figure 4.4 and Figure 4.6). Synthetic base oil PAO 6 was used for all tribological tests. Tests samples and parameters were summarized in Table 5.3. Note that testing parameters were similar to those used for textured samples (Table 4.2), however milder conditions were evaluated here (higher speed and lower SRRs), see Table 5.3.

Table 5.3 – Test parameters used for friction (MTM2 rig) and film thickness (EHD1 rig) measurements, sintered samples.

	MTM2 rig	EHD1 rig
Disk material	D4, D5, D6 and NP* (AISI 52100)	Glass
Ball material	B8, B9, B10 and NP* (AISI 52100)	
Oil	PAO 6	PAO 6
Range of entrainment speed, $U_e$ (mm/s)	2000 – 100**	2200 – 20
Slide-to-roll ratio, SRR (%)	5 – 20 – 50 – 80 – 100 – 120**	0
Temperature (°C)	40	40
Contact pressure (GPa)	0.6	0.5
Kinematic viscosity at 40 °C (mm <sup>2</sup> /s)	31	31

\*Non-porous reference material was AISI 52100 both for ball and disks samples.

\*\*Limited values compared to those used for textured material see Table 4.2.

Sintered balls (B8, B9 and B10) and disks (D4, D5 and D6) were tested separately against non-porous (**NP**) reference samples, whereas NP pairs were used as reference bench material, see Figure 5.5. Sintered pairs were not tested to avoid complex combination of effects derived from surface with different porosity properties. Furthermore, previous work [17] showed that PM pairs led to detrimental results compared to hybrid combinations (NP x PM).

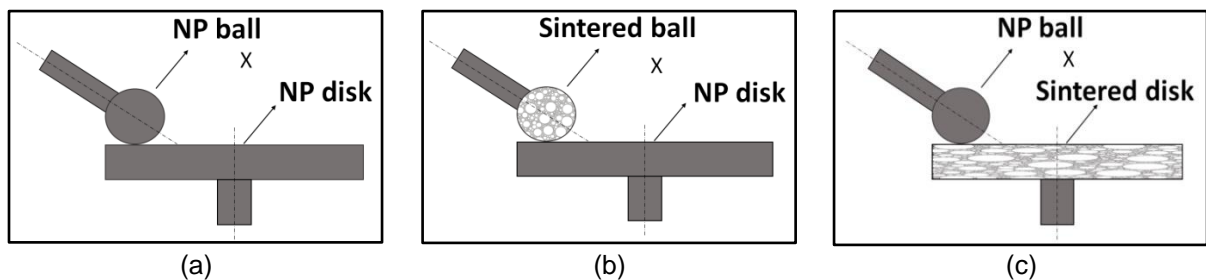


Figure 5.5 – Schematic representation of test configurations. (a) Reference bench pair NP x NP, (b) sintered balls x NP disk and (c) NP ball x sintered disk.

### 5.3.2 Results and discussion

Results were organized and presented depending on test configurations, similarly to the division adopted in the previous section.

- **Pin-on-disk**

Average values of friction were calculated during tribological tests, being that speed and load were maintained constant, see Figure 5.6. The decrease of porosity from D8 to D10 (see Table 3.1) led to friction reduction. Surface with less porosity and rounded-shape pores (D10) performed significantly better than high porosity samples (D8). Furthermore, less porous disks (D10) reduced friction by 15% when compared to NP samples, see Figure 5.6. Intermediate porosity conditions (D9) behave similarly to NP and more porous ones (D8) led to 10% of increment compared to reference specimens (NP).

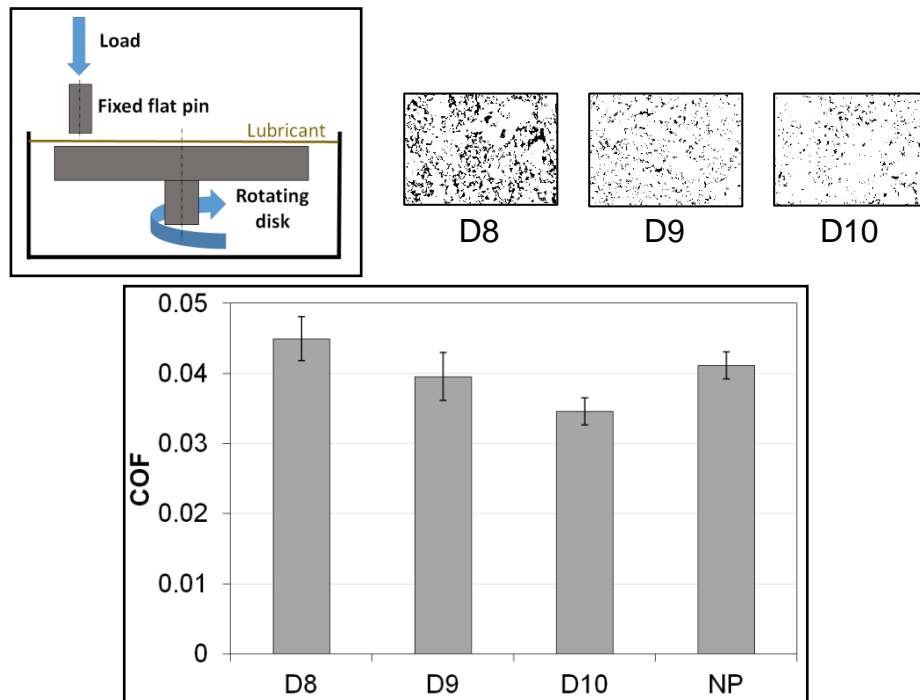


Figure 5.6 – Average friction and standard deviations values of NP and sintered disks for pin-on-disk configuration, adapted from [23].

Sample surfaces were analysed prior and after frictional test to evaluate wear mechanisms. The parameters used during sliding tests (high speed and low load in conformal contact) did not cause significant wear both on disk and pin surfaces. For instance, it was difficult to properly identify the testing track of disks samples even using SEM, see Figure 5.7. Low contact pressure in conformal contact conditions did not cause significant surface alteration on PM disks, therefore surface pores remained open after frictional tests. Surface of less porous disks samples (D10) was shown in Figure 5.7 as example.

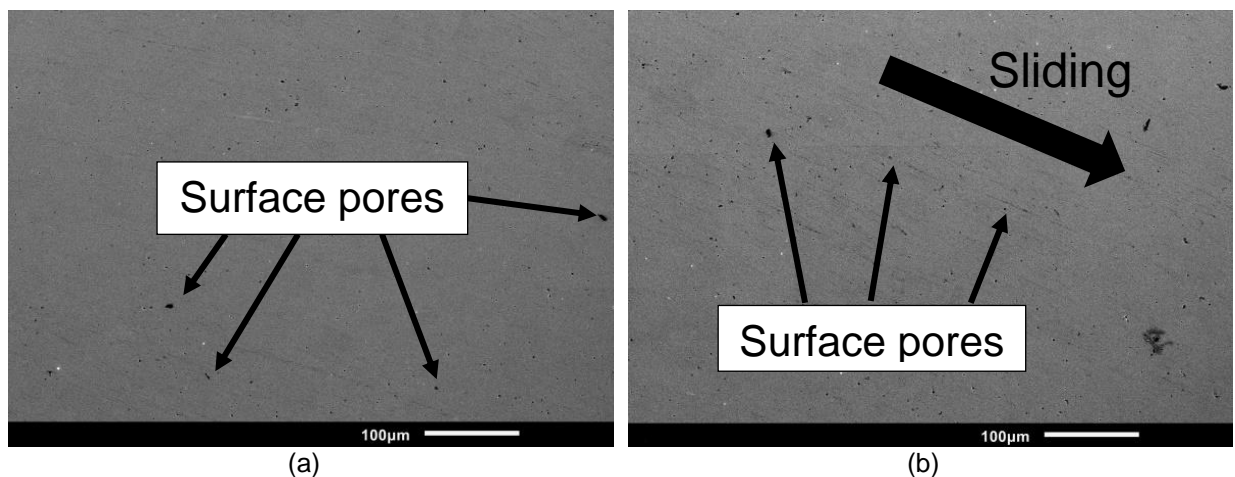


Figure 5.7 – SEM surface images of D10 sintered disk (a) before and (b) after pin-on-disk test (wear track), adapted from [21].

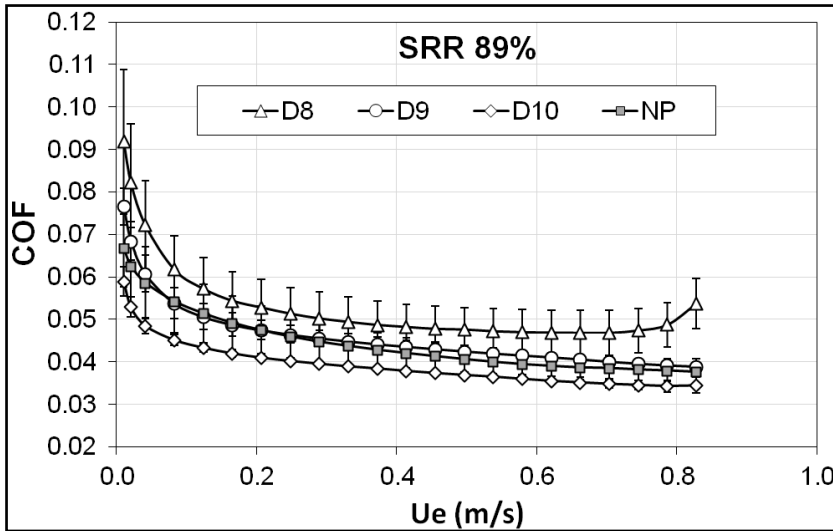
Note that less porous material (D10) presented less surface micro valleys and theoretically offered more solid contact than high porosity samples (D8). Despite this, D10 reduced friction compared to D8, see Figure 5.6. Rounded shape pores of reduced dimensions in D10 seemed to improve load carrying capacity and thus reduce friction (micro bearing effect). On the contrary, the increase of pore dimensions and irregular shape in D8 led to friction increment, probably related to a negative disturbance in lubricant flow caused by the higher size, density, proximity and irregularity of the pores.

General results found here had opposite trend to those encountered in literature [15,17], where the increase of porosity improved tribological performance. It is worth noting that lubrication regime was boundary in [15,17] and surface pores mainly acted as oil reservoirs, supplying additional lubrication and preventing wear. On the contrary during pin-on-disk experiments here, the regime seemed to be full film, especially due to friction values encountered (see Figure 5.6) and absence of wear (see Figure 5.7). In this lubrication condition, surface pores had micro bearing effects rather than oil reservoirs. Therefore, small rounded pores seemed to promote local film thickness increment and reduce friction in opposition to large pores that probably caused film breakdown. Tribological effect of surface pores in D10 disks could be compared to those obtained for successful cases fabricated by more expensive texturing techniques [44].

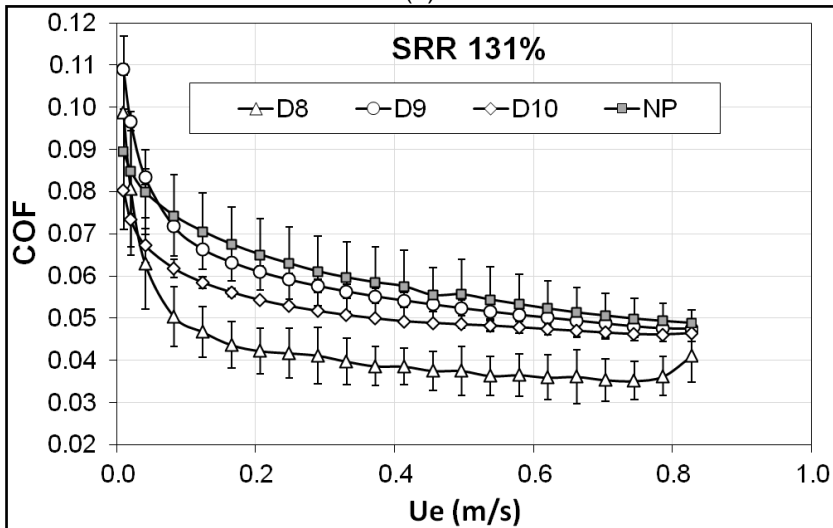
- **Roller-on-disk**

Friction results for all disk configurations were plotted varying entrainment speeds, see Figure 5.8. Each point in the graph represents the average value of three test repetitions for a certain speed.

In mild testing conditions (SRR 89%), porosity friction trend was similar to those presented for conformal contact tests (pin-on-disk), see Figure 5.8a and Figure 5.6. Particularly, less porous disks (D10) reduced friction at all speeds, intermediate porosity conditions (D9) behave similarly to NP and more porous specimens (D8) yielded higher friction.



(a)



(b)

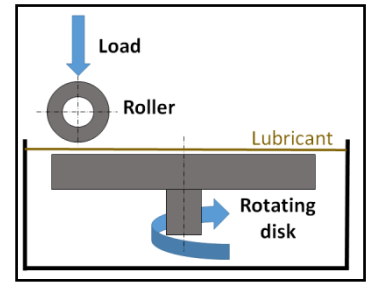


Figure 5.8 – Friction behaviour varying entrainment speed ( $\text{COF} \times U_e$ ) for sintered and NP disks in roller-on-disk configuration. Error bars represent standard deviation for each speed. (a) SRR = 89% and (b) SRR = 131%, adapted from [21].

During tests with higher slide-to-roll ratio (SRR 131%), NP samples still performed similarly to D9 (intermediate porosity) and they both increased friction compared to less porosity material (D10) for all speeds, see Figure 5.8b. In contrast with trend encountered for SRR 89%, more porous material (D8) promoted best friction reduction even compared to D10 sintered material. This behaviour was better scrutinized and understood through surface analysis.

Steel roller was not significantly worn out during frictional tests, whereas disks surfaces presented wear tracks. Track dimensions were measured using 3D optical profilometry and main results were summarized in Figure 5.9.

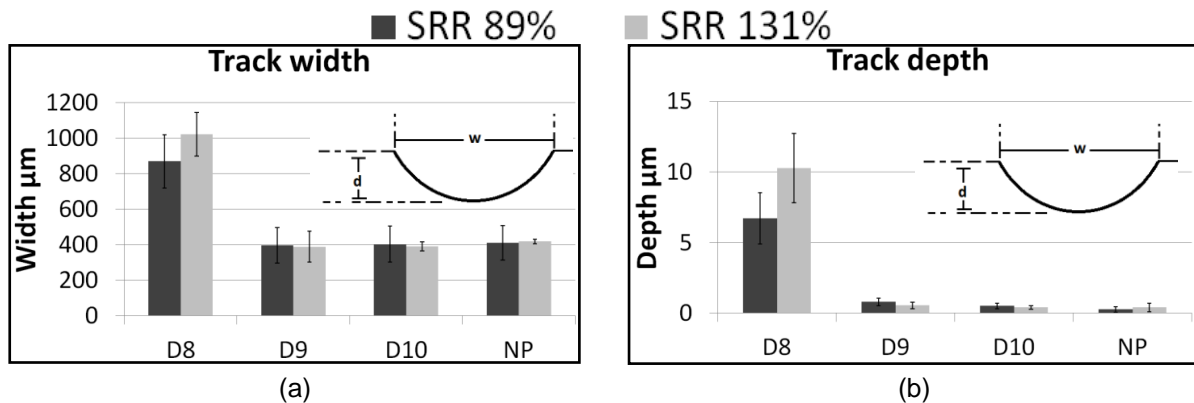


Figure 5.9 – Wear track geometrical dimensions (depth and width) of the sintered and NP disks after roller-on-disk tests, adapted from [21].

Wear tracks of more porous material (D8) were considerably larger and deeper than other disk conditions both for SRR 89% and 131%. NP and less porous disks (D9 and D10) presented similar wear track size for both testing conditions. Note that for harsh test conditions (SRR 131%), more porous material D8 formed a wear track approximately fifty times larger than for NP specimens, changing the relative contact conformity. Furthermore, large surface deformation in D8 disks induced surface pore closure (see Figure 5.10), whereas surface micro cavities remained open for all other PM specimens. Surface analysis of D8 disks was depicted in Figure 5.10

Generally, porosity of small dimensions with regular round shape (D10) achieved best friction response and the increase of pore size and irregular shape led to detrimental results. Lubricant film formation varying pore dimensions was recently evaluated in [113]. It was proved that small sized pores promote local lubricant film formation reducing solid contact, whereas lubricant squeezes within open and large surface porosity, generating local film breakdowns (increase asperities contact) and friction raises. Another key parameter to be considered in this analysis is cavity depth, especially important for non-conformal contact [9], see Section 4.4. Shallow features reduced friction compared to untextured reference cases due to micro bearing effects [48,95]. Deep surface cavities could lead to lubricant local pressure and viscosity drop, therefore beneficial effect in non-conformal contact could be obtained especially using shallow surface cavities. Similar considerations were made for surface texture configuration in Section 4.5.2, see Figure 4.16. In this study, surface pores depth was not measurable via optical profilometry and it was assumed that the increase of pores size generally leads to deeper cavities. Therefore, surface

pores in D10 promoted friction reduction probably due to reduced dimensions, rounded shape and shallow depth, similarly to dimples successful configurations [48,95].

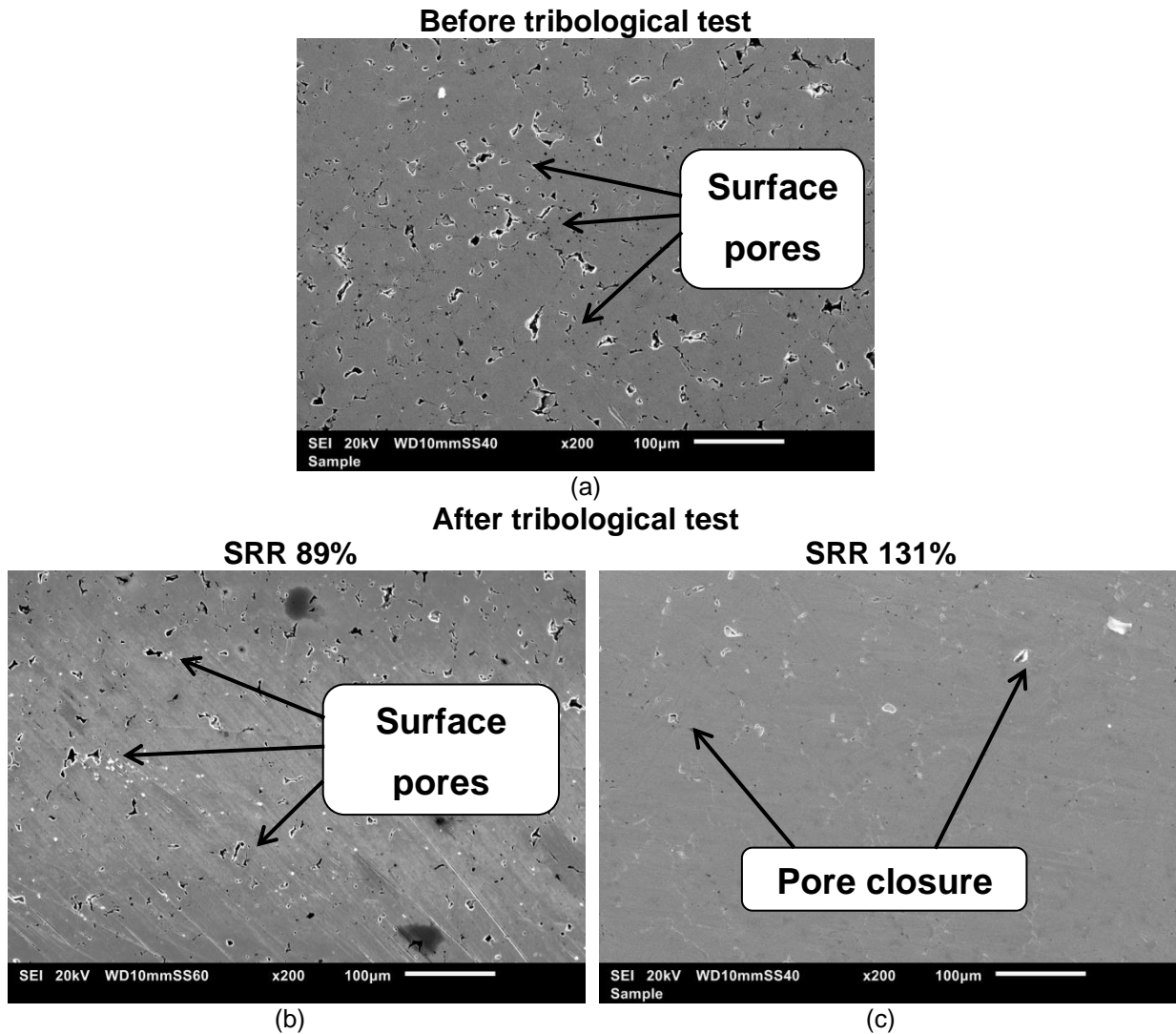


Figure 5.10 – SEM surface images of D8 sintered disk (a) before roller-on-disk tests and wear tracks after testing using (b) SRR 89% and (c) 131%, adapted from [21].

More porous samples (D8) behaved out of trend at SRR 131%, presenting best coefficient of friction reduction, see Figure 5.8. Harsh test conditions combining high contact pressure and sliding speed caused significant plastic deformation and surface pores closure in more porous surfaces (D8). Low density material did not offer enough surface load capacity when tested at high contact pressure, therefore pores could collapse, as showed in [19,22]. In this context, the E/H ratio could be used as a deformation indicator, as reported in [116]. Surface roughness, mechanical properties and plasticity index of sintered and NP samples were summarized in Table

5.4. More porous material (D8 and D9) presented higher surface roughness values, even if the same polishing procedure was used for all samples.

Table 5.4 – Roughness parameters (RMS), material properties (E,  $\nu$  and H), asperities characteristics ( $\sigma$  and  $\beta$ ) and plasticity index  $\psi$  of the tested materials.

	RMS* (nm)	E (GPa)	$\nu$	H (GPa)	$\sigma$ (nm)	$\beta$ ( $\mu\text{m}$ )	$\psi$
<b>D8</b>	83 ± 38	117	0.27	2.4	0.045	38.4	1.13
<b>D9</b>	82 ± 39	161	0.28	4.9	0.016	43.7	0.39
<b>D10</b>	27 ± 19	197	0.29	5.9	0.006	133.4	0.13
<b>NP</b>	4 ± 0.08	210	0.29	5.4	0.005	46.8	0.22

\* The nomenclature used in this work for root mean square deviation was RMS. For PM material, only plateau root mean square deviations were considered (Spq), whereas for NP material, root mean square deviation of surface (Sq) was used, see Section 3.4.

NP and more dense PM materials (D9 and D10) suffered elastic deformations, for instance they presented  $\Psi < 0.6$ , see Table 5.4. On the contrary, more porous material with rougher surface was prone to plastic deformation ( $\Psi > 1$ ). Despite the limitations of this calculation, the  $\Psi$  parameters corroborate to scrutinize and analyse PM results.

Notwithstanding the increase of porosity decreased mechanical properties (E,  $\nu$  and H), more porous material (D8) presented higher E/H ratio than other samples (see Figure 5.11), confirming the proneness in deform plastically and consequently causing possible pores collapse. Additionally, surface wear in D8 created a semi-spherical cavity, altering progressively contact configuration from non-conformal to conformal, hence decreasing contact pressure. For instance, D8 friction results in non-conformal contact were approximately 0.04 (see Figure 5.8b), similar to values experienced during conformal contact test (see Figure 5.6). Surface pores also negatively influenced material topography, see Table 5.4. This response jointly with the detrimental effect of porosity on mechanical properties brought to plasticity index higher than 1 for more porous surface (D8), see Table 5.4.

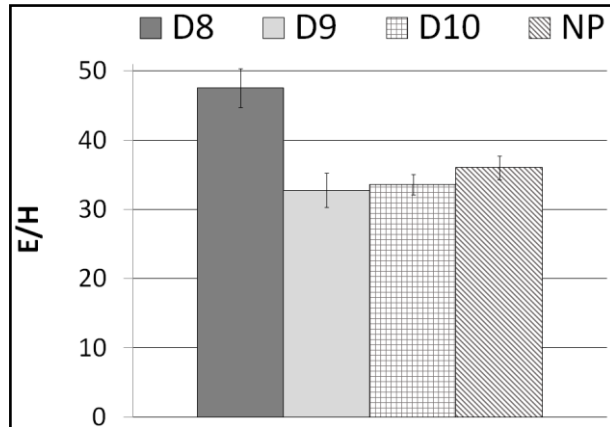


Figure 5.11 – E/H ratio for NP and sintered disks, adapted from [21].

- **Ball-on-disk**

Friction map surface ( $\text{COF} \times U_e \times \text{SRR}$ ) could be obtained similarly to those studied for textured material (see Section 4.5.2), however main results are depicted here as “Stribeck like” curve ( $\text{COF} \times U_e$  with fixed values of SRR) to better visualize and quantify difference between sample frictional behaviour. Friction trends did not change with varying SRR conditions, therefore results of both sintered disks and balls were presented for “boundary” test condition (SRR 5% and SRR 120%).

High porosity surfaces in PM disks increased friction at every speed tested (see Figure 5.12), similarly to what founded previously for pin-on-disk and roller-on-disk tests. Less porous samples (D4) decrease friction compared to more porous ones (D5 and D6). However, standard NP disks yielded to friction values significantly lower than PM material. Note that PM disks were produced by conventional sintering techniques and presented higher values of porosity and pores dimensions, compared to SPS disks, see Table 3.1. Furthermore, conventional sintered disks had higher values of surface roughness compared to SPS disks (see Table 5.4) and especially to NP ones, see Table 5.5.

Table 5.5 – Surface roughness of PM and NP samples for ball-on-disk configuration.

	<i>Conventional Sintering</i>			<i>SPS</i>			<b>NP</b>
	<b>D4</b>	<b>D5</b>	<b>D6</b>	<b>B8</b>	<b>B9</b>	<b>B10</b>	
RMS (nm)	370±85	280±70	190±60	180±50	180±55	180±50	20±4

MTM2 rig requires samples with tight controlled dimensions and high standard of precisions, since it is very sensitive to roughness and samples flatness. PM disks

presented therefore higher values of friction due to higher roughness and also probably to the custom-made process to manufacture these non-conventional samples.

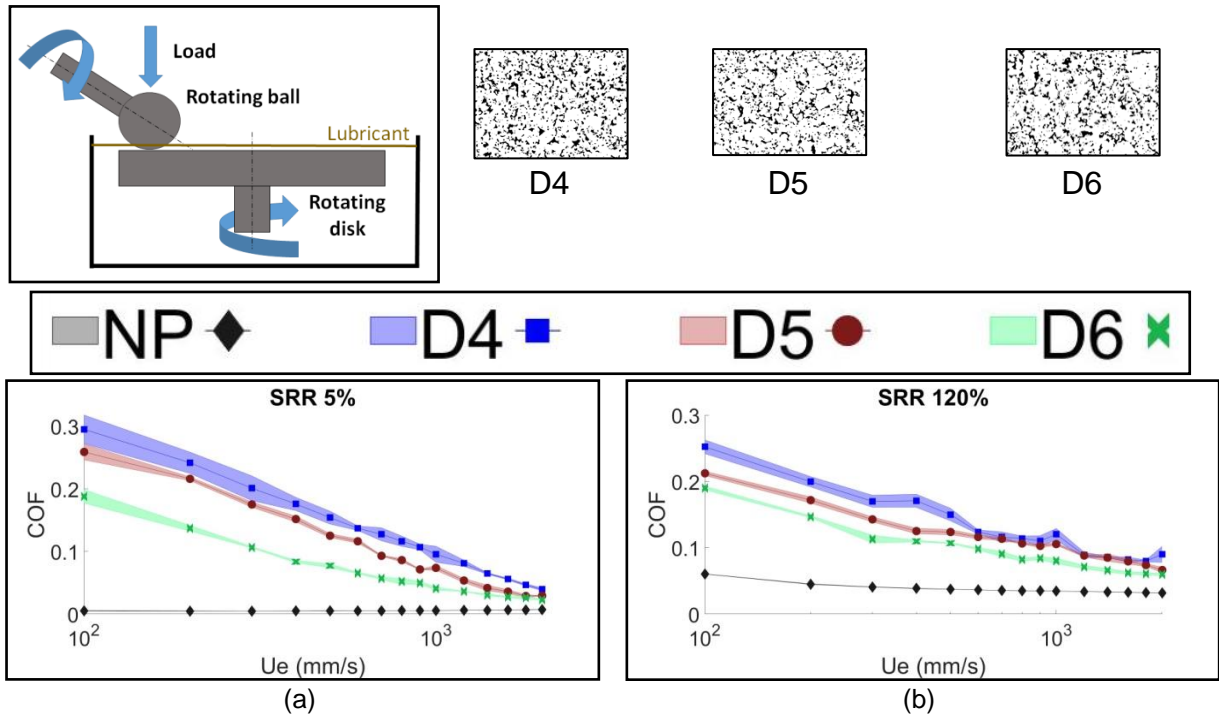


Figure 5.12 – COF  $\times U_e$  for sintered and NP disks in ball-on-disk configuration using (a) SRR 5% and (b) SRR 120%.

Friction results of PM and NP balls were shown in Figure 5.13. Besides bulk properties of PM balls, it is also important to consider surface porosity, since the manufacturing process caused pores closure in some configurations (B9 and B10) and limited porosity and pores dimensions in others (B8), see Table 3.2. For instance, PM balls with pore closures (D9 and D10) yielded to similar friction results especially for high sliding conditions (SRR 120%), even if bulk properties were different. Note that PM balls with residual porosity (B8) reduced friction compared to other PM samples at all SRR and  $U_e$  conditions, see Figure 5.13. NP balls improved notably friction performance when compared to PM samples. These behaviours could be influenced by higher roughness values of PM balls (see Table 5.5) and manufacturing processes, similarly to PM disks conditions.

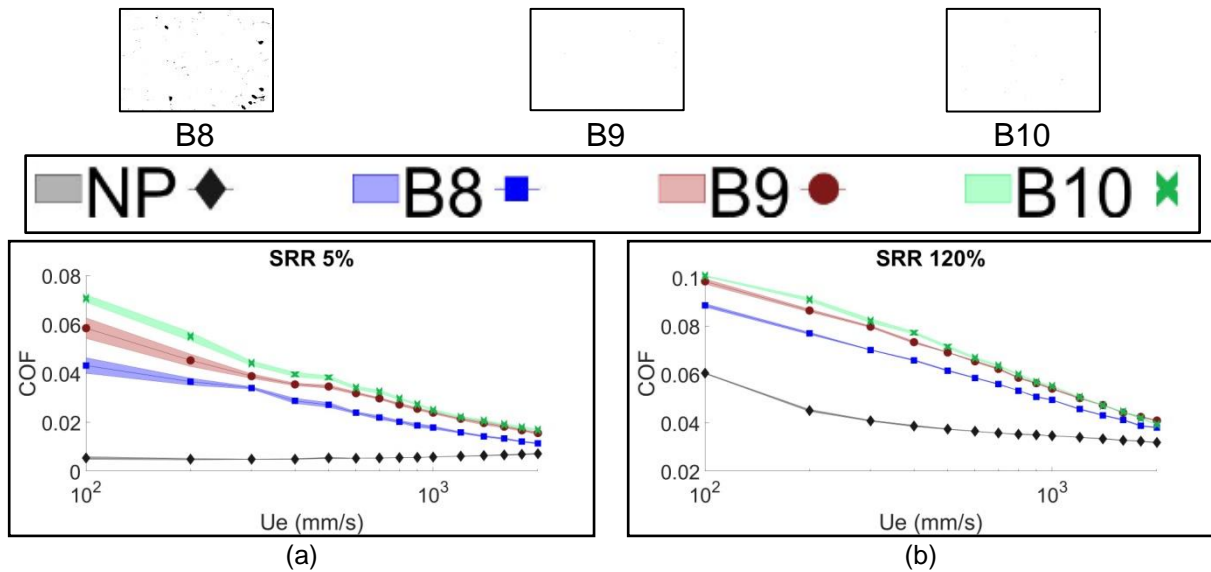


Figure 5.13 – COF  $\times U_e$  for sintered and NP balls in ball-on-disk configuration using (a) SRR 5% and (b) SRR 120%.

Both ball and disk samples did not wear out significantly; it was difficult to identify test track in many cases. Test conditions did not cause surface pore closure in PM material. Only more porous PM disks presented some superficial scratches, however they did not alter considerably surface conditions, since they are shallower than surface pores, see Figure 5.14.

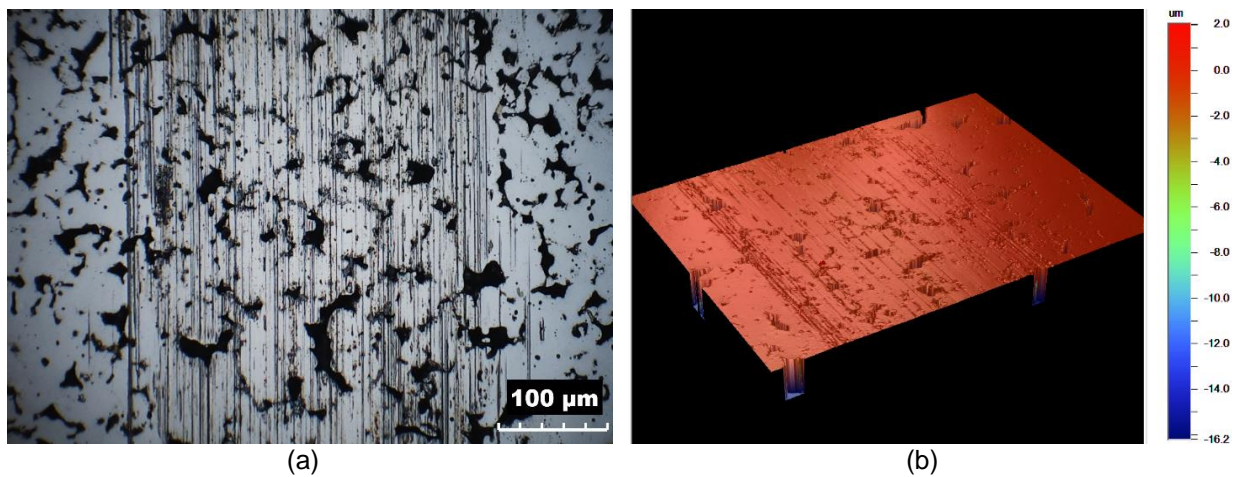


Figure 5.14 – (a) Wear track of D4 sintered disk and (b) 3D profile image.

The increase of surface pores, pores dimensions and irregularity shape led to detrimental effect on friction response, as found also in other testing configurations.

Friction response highly depends on morphology of surface micro cavities, as reported in [117]. Dimples geometry (“perfect” rounded shape) and the absence of material pile-up potentially improve lubrication and reduced friction [9,118]. Precise

control on morphology of surface cavities is difficult to achieve for PM materials, however material with small rounded pores decreased friction when compared to more porous surfaces. For instance, residual surface porosity on B8 (2%, rounded shape and reduced dimensions, see Section 3.3) could be compared to dimple texture configurations [111,119]. Even if pores are randomly distributed rather than precisely tailored by laser texture, a friction reduction was obtained compared to PM material with pores closures (B9 and B10), see Figure 5.13.

Surface roughness highly influences friction in this test conditions, therefore results were evaluated in terms of specific film thickness for avoiding comparisons between materials with significant difference in roughness. Particularly, NP had much lower RMS values than PM balls (see Table 5.5) and consequently it was tested at lower speeds (up to 10 mm/s) to achieve similar  $\Lambda$  values of PM material. Note that film thickness was measured for sintered and smooth balls using interferometry technique, as explained in Section 5.3.1 (ball-on-disk).

Surface friction response (COF x  $\Lambda$  x SRR) is depicted in Figure 5.15. The colour scale was intentionally the same for the different configurations to enhance visual comparisons. Main difference could be noticed at low  $\Lambda$  combined with high SRR values. For instance in this region, B8 decreased friction compared to NP. Balls B9 and B10 generally presented higher friction than B8 and NP samples.

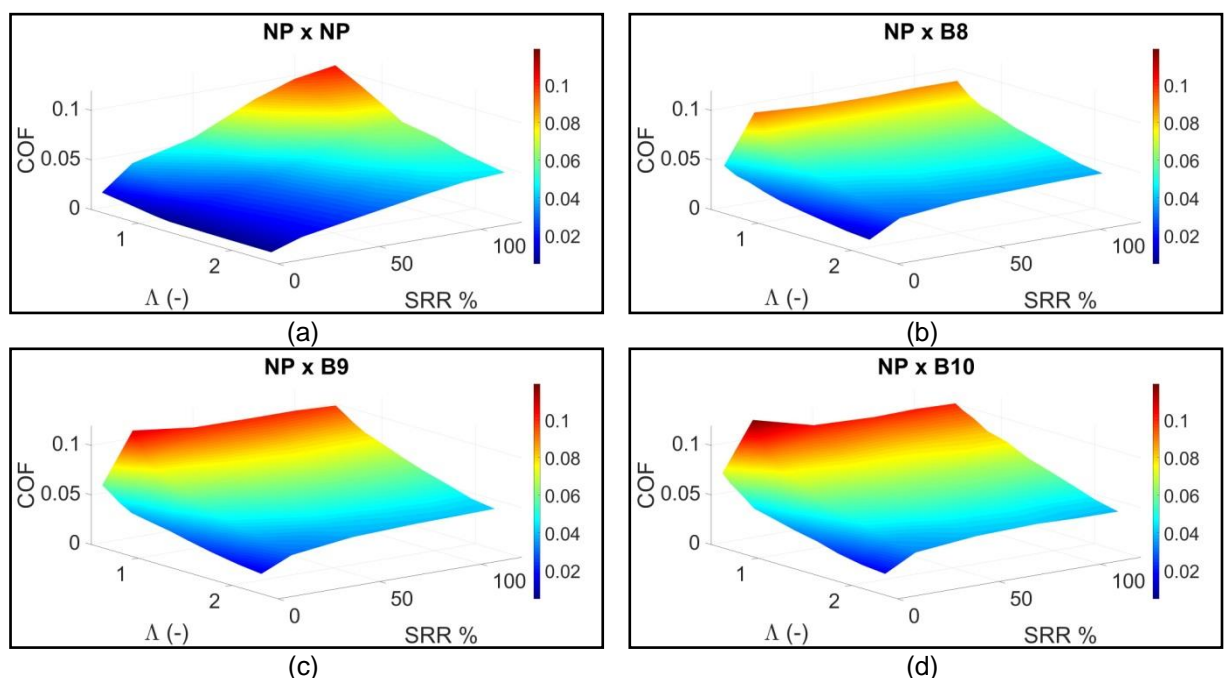


Figure 5.15 – Traction map (COF x lambda ( $\Lambda$ ) x SRR) for NP and sintered balls.

Quantitative analysis could be conducted studying again “Stribeck like” curves, see Figure 5.16. Ball with residual porosity (B8) always performed better than other PM conditions both varying SRR and  $\Lambda$  ratios. NP samples presented low friction values using SRR 5% (see Figure 5.16a), however the increase of sliding ratio (SRR 80%) led to friction increment and NP behave similarly to B8 specimens, see Figure 5.16b. For harsher test conditions (SRR>100%), NP performed similarly to B9 and B10, whereas balls with residual porosity (B8) decreased friction compared to NP. These findings corroborate with the hypothesis presented in the previous section, being that residual porosity could act as textured dimples and improve lubrication especially in harsh test conditions.

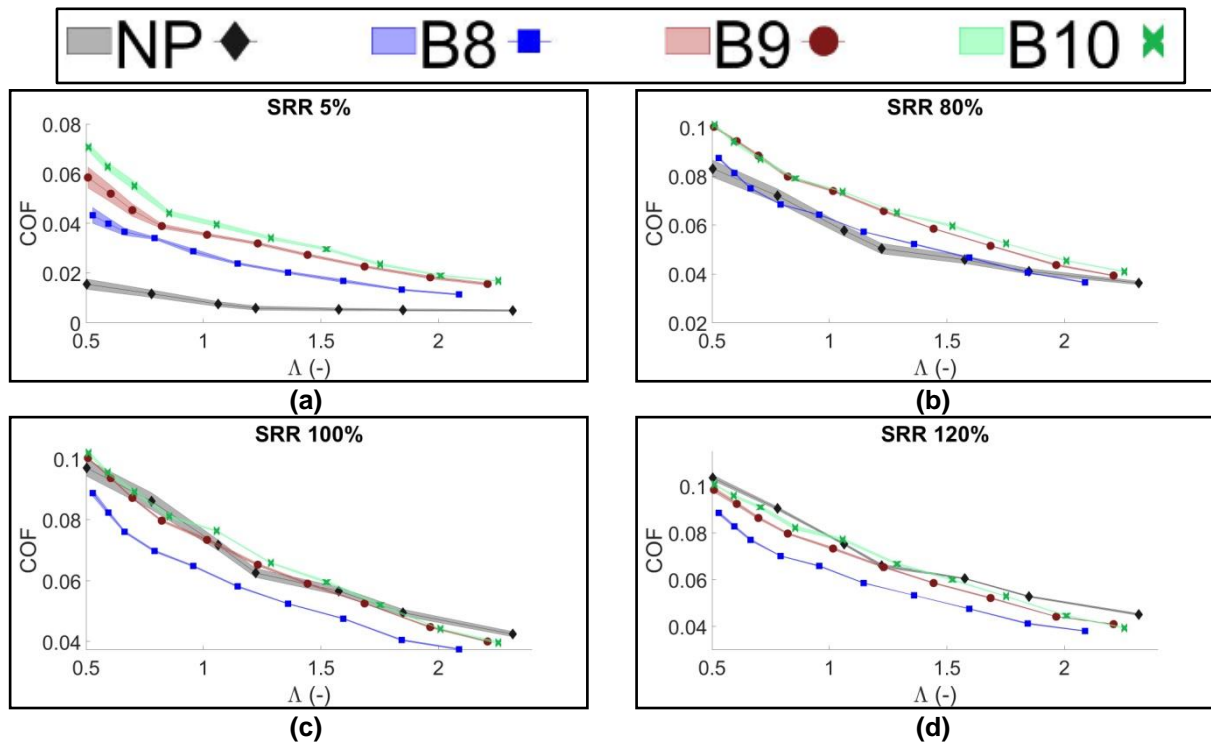


Figure 5.16 – COF x specific film thickness  $\Lambda$  for NP and sintered balls using (a) SRR 5%, (b) SRR 50%, (c) SRR 100% and (d) SRR 120%.

#### 5.4 Conclusions and final remarks of the chapter

The aspects surrounding PM tribology were evaluated within this chapter, both scrutinizing literature and experimental results obtained. Three different porosity features were applied both on ball and disks specimens. The following conclusion could be done:

- Surface porosity plays a crucial role in tribological performance, since surface pores represent micro valleys, alter simultaneously surface roughness and morphology and even mechanical properties (reduce hardness);
- The increase of surface porosity led to detrimental friction results. For instance, open and large surface porosity seemed to avoid film formations, causing film breakdown and friction increment;
- PM material with reduced porosity (around 2%) and more regular shape pores (high circularity index) reduced friction compared to reference wrought material (NP). Therefore, the beneficial effect of randomly distributed cavities can somehow compare to those obtained using textured dimples.

## **Chapter 6      Phenomenological model proposal**

### **6.1 Introduction**

The previous chapters explored the frictional effects of pores and laser surface texture under lubricated test conditions. The micro cavities studied presented different geometrical and morphological (dimples, grooves and pores) dimensions, consequently they yielded to different friction responses. In this chapter, surface features and main tribological effects were classified and summarized. After that, general trending was analysed to scrutinize if different surface features could bring to similar results and which are the physical phenomena involved. Finally, a surface parameter was proposed for obtaining friction response of surface micro irregularities from standard material (smooth, without irregularities).

### **6.2 Model**

Main effects of surface micro cavities (pores and texture) were summarized in Table 6.1. Note that these results were achieved using different tribometers (MTM2 and UMT-2 Bruker), samples and test conditions, thus this table help to classify and map the general behaviour of surface features. Furthermore, PM materials were classified here depending on pore dimensions (large, intermediate and small) rather than sintering parameters. Only dimples and perpendicular grooves were considered for textured materials, being that generally longitudinal configurations brought to friction increments.

Table 6.1 – Summary of surface micro feature effects depending on geometry, lubrication and test conditions. Friction result and main effects were compared with a reference wrought material (non-porous or untextured – NP). This table summarizes only results and test conditions that did not alter material surface integrity (reduced surface wear, maintaining the initial geometrical characteristics of micro cavities)

	Sintered material			Textured material		
	Large porosity (LP)	Intermediate porosity (IP)	Small porosity (SP)	Dimples (D)	Grooves	
					Shallow (SG)	Deep (DG)
<b>Main effects</b>	-Friction increase	-Friction do not change significantly	-Friction reduction -Micro bearing effect -Increase lubricant load support capacity	- Friction reduction -Decrease lift-off speed -Full film condition for lower speed	- Slight effects on friction reduction at low speeds	
<b>Depth (µm)</b>	2 to 20*	1 to 5*	1 to 3*	<0.5	<0.5	>1
<b>Width (µm)</b>	5 to 40	2 to 10	2 to 5	15-50	7-25	20
<b>f (area coverage)</b>	11 to 16%	6%	2-4%	1%-14%	12.5%-47%	10%
<b>Circularity</b>	0.5-0.6	0.6	0.75	1	/	/
<b>Directionality</b>	Random	Random	Random	Random	Perpend.	Perperd.
<b>Lubrication regime</b>	Boundary/Mixed	Boundary/Mixed	Boundary/Mixed	Boundary to Full film	Boundary to Full film	Boundary to Full film
<b>Contact type</b>	Conformal/ Concentrated	Conformal/ Concentrated	Conformal/ Concentrated	Concentrated	Concentrated	Concentrated
<b>Contact pressure** (GPa)</b>	0.6-1	1	0.6-1	0.6	0.6	0.6
<b>SRR</b>	0 to 131%	0-89-131%	0 to 131%	5 to 180%	5 to 180%	5 to 180%
<b>Lambda (Å)</b>	0.5 to 2.3	0.5 to 2.3	0.5 to 2.1	0.8 to 7	0.8 to 7	0.8 to 7
<b>Tribometer</b>	Bruker (pure sliding and SRR), MTM2	Bruker (pure sliding and SRR)	Bruker (pure sliding and SRR), MTM2	MTM2	MTM2	MTM2

\*estimated value

\*\*Hertzian contact pressure evaluated for concentrated point contact

Some principal results of surfaces with micro cavities (pores and texture) and standard reference material (NP) were selected to represent general results trend, see Figure 6.1. Tribological studies of sintered material were presented in case a) and b), whereas case c) was related to textured samples. For each sample with surface features, a parameter (*Delta*  $\Delta$ ) was defined to quantify friction differences compared to standard NP samples. *Delta* ( $\Delta$ ) results of friction are shown below each graph. *Delta* is the mean value of friction increment within different speeds, expressed in percentage, similarly to parameters used for textured material (see Equation (12)). This parameter was defined as follows:

$$Delta (\Delta) = \left( \frac{COF_{features} - COF_{NP}}{COF_{NP}} \right) \times 100 \quad (13)$$

$COF_{features}$  and  $COF_{NP}$  represent respectively the coefficient of friction related to samples with surface micro cavities (pores or texture) and standard reference material. Negative results of *Delta* indicate friction reduction compared to standard material NP (non-porous or untextured), whilst positive values represent friction increment, see Figure 6.1.

Results of case a) are related to roller-to-disk tests and of case b) to ball-on-disk configurations, see Section 5.3.2. Case c) studied textured material on ball-on-disk configuration, see Section 4.5.2.

As previously summarized in Table 6.1, small porosity (SP) material performed friction reduction within the range of speeds studied, approximately around 10% (see Figure 6.1a and b). Intermediate porosity did not change significantly friction results compared to NP ( $\Delta_{IP}=3\%$ ), whereas the increase of porosity (LP) led to friction increment ( $\Delta_{LP}=16\%$ ), see Figure 6.1a. Dimples configuration (D) presented friction reduction ( $\Delta_D$  around  $-20\%$ ), whereas deep grooves always brought drawbacks ( $\Delta_{DG}$  over  $30\%$ ), see Figure 6.1c. Shallower grooves configuration (SG) slightly improved tribological performances especially at low entrainment speeds ( $\Delta_{SG} = -4\%$ ), see Figure 6.1c. *Delta*  $\Delta$  results (% values) of all surface features considered in Figure 6.1 are summarized in Figure 6.2.

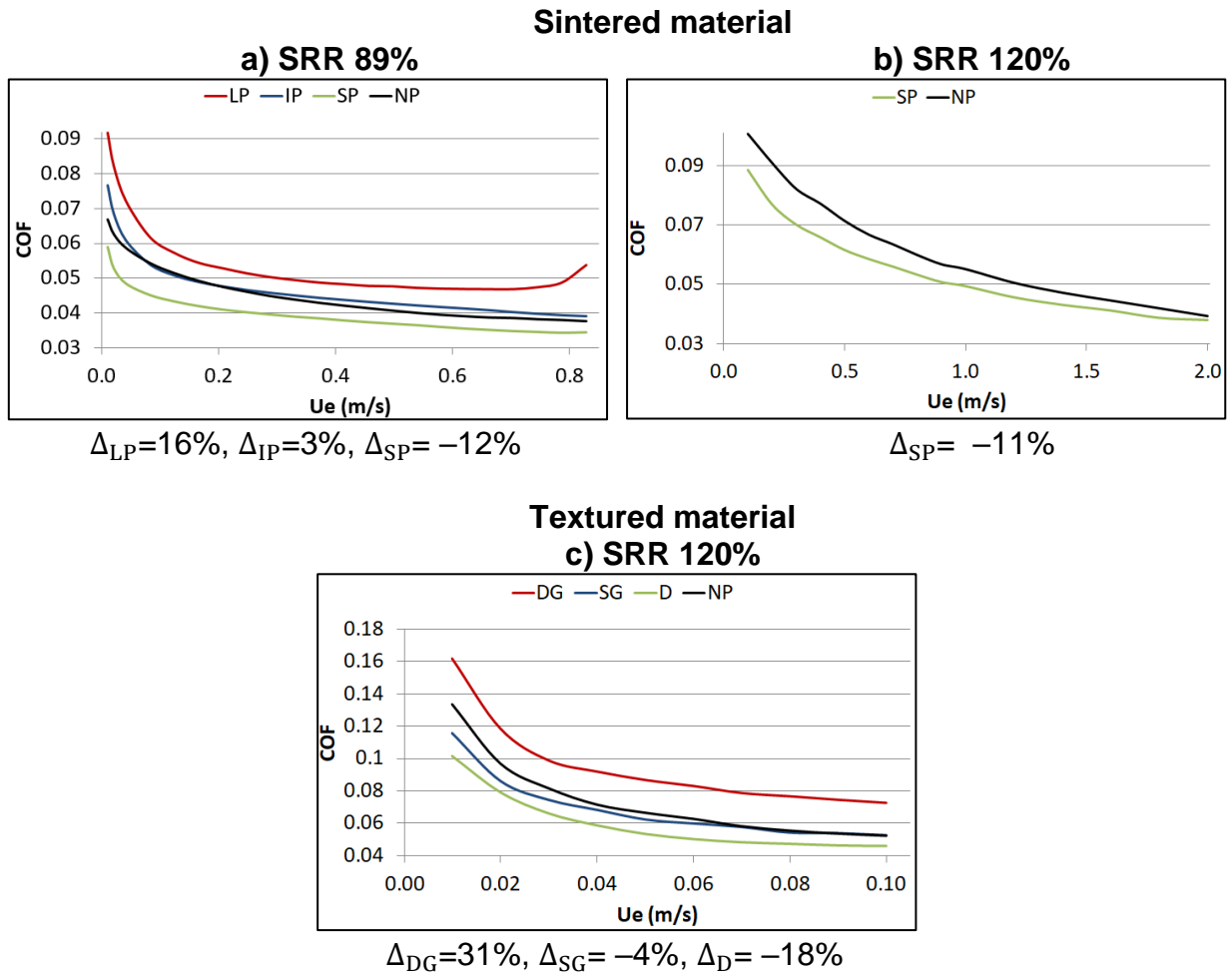


Figure 6.1 – Coefficient of friction results vs entrainment speeds ( $U_e$ ) for sintered (a) and (b) and textured material (c). Delta  $\Delta$  values (%) are expressed below each graph.

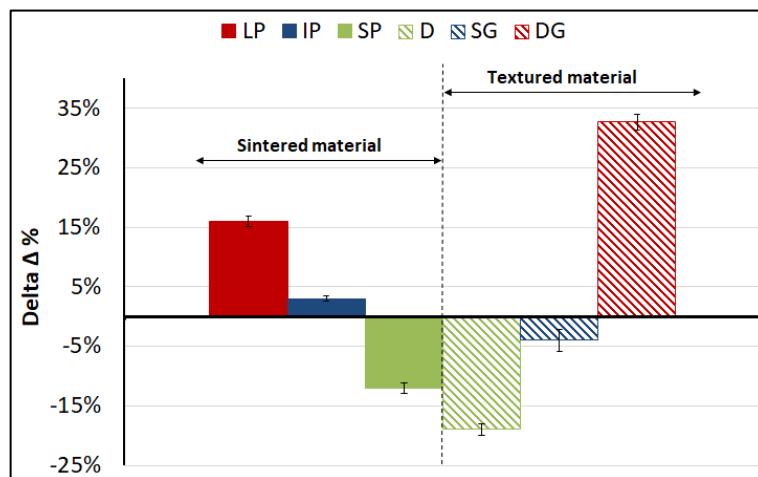


Figure 6.2 – Delta  $\Delta$  results (%) of sintered (LP, IP and SP) and textured (D, SG and DG) materials.

Rounded **shape** surface cavities of reduced dimensions (SP and D) improved frictional performances in different test conditions and especially using low entrainment speeds. As demonstrated in previous works [18,20], the micro bearing

effects of micro cavities with this size and morphology could increase lubricant load support capacity and consequently reduce friction between rubbing surfaces. The increase of pore dimensions and irregular shapes (IP and LP) led to detrimental tribological results when compared to non-porous material, see Figure 6.2. The hypothesis is that lubricant could squeeze within large open porosity, causing film breakdown and consequently increasing friction, as also reported in [113]. These factors could avoid micro bearings effects and even disturb hydrodynamic pressure distribution, causing worse results compared to untextured surfaces. Furthermore, more porous samples (IP and LP) also had rougher surfaces that negatively affected tribological performances [23].

Another crucial factor to be considered in concentrated contact test is the feature **depth** [18,95]. The counter-body passage on a textured surface could cause the increase of local pressure and viscosity. Using shallow features, if the pressure is sufficient to increment the local viscosity, the lubricant squeeze out the cavities and improves load carrying capacity [48]. Deep surface cavities did not increase local pressure and could potentially cause local viscosity drop and friction increment, as experienced in [48]. Assuming that larger pores in sintered samples were also deeper, it is possible to justify that the reduction of friction was significant using surfaces with pores of reduced dimensions and depth (SP) rather than with larger sizes (IP and LP). For these reasons, textured dimples and surface pores in sintered material could be somehow compared, even if surface pores can be seen as irregular-shaped micro cavities with random distribution.

Groove geometry (SG and DG) did not bring the same benefits as the rounded-shaped one. Shallow grooves (SG) generally behave similar to NP material, whereas the increase of **features deep** (DG) led to friction increments, see Figure 6.2. Grooves were oriented perpendicular to entrainment direction to maximize squeeze effects [5]. However, groove geometry could permit the lubricant to squeeze out the canal, probably avoiding the local viscosity increment and the improvement of load carrying capacity. As previously observed for rounded-shaped features, the decrease of cavity depth improved tribological performance, however even shallow groove configurations (SG) were not very effective in the tested configurations, see Figure 6.2.

The presence of shallow small micro cavities with rounded shape seemed to be the best geometry within those tested, especially for lower entrainment speeds. To better understand the trend presented in Figure 6.1, a phenomenological model was proposed. For this purpose, a surface parameter  $s$  was derived from geometrical and morphological characteristics of surface features (pores and texture). Firstly  $\Delta$  values were calculated to identify main trends. After that, a visual inspection of feature geometrical characteristics was made and principal tendencies were detected (i.e. for rounded features, depth and  $\Delta$  presented same trends, whereas circularity and  $\Delta$  opposite ones). Finally, the most significant parameters presenting coherent trends were selected for defining a mathematical formulation through several attempts using  $\Delta$  as target value, see Figure 6.3.

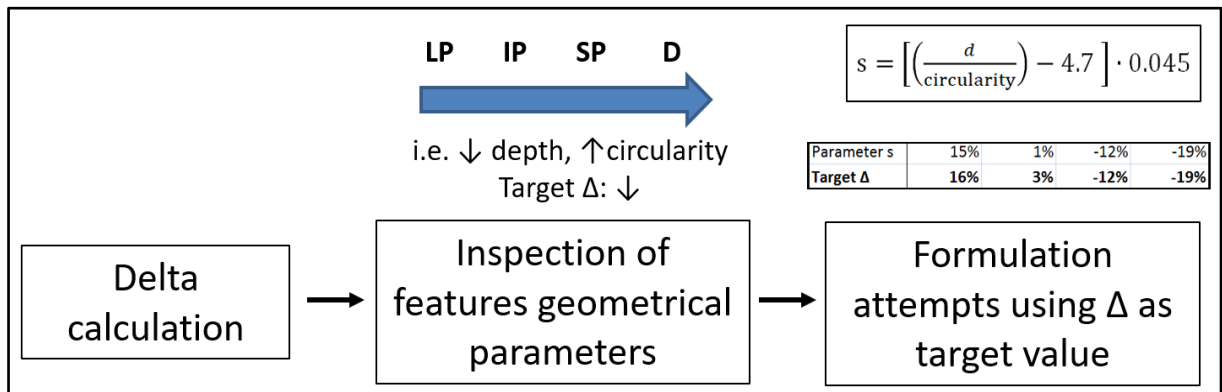


Figure 6.3 – Methodology adopted for the empirical definition of surface parameter  $s$ .

A schematic representation of the methodology used for obtaining numerical values is presented in Figure 6.4. Note that after defining  $\Delta$  values and selecting main geometrical parameters, a series of numerical attempts was made to obtain similar values of  $s$  and  $\Delta$ . This procedure was adopted separately for rounded and grooved-shape features.

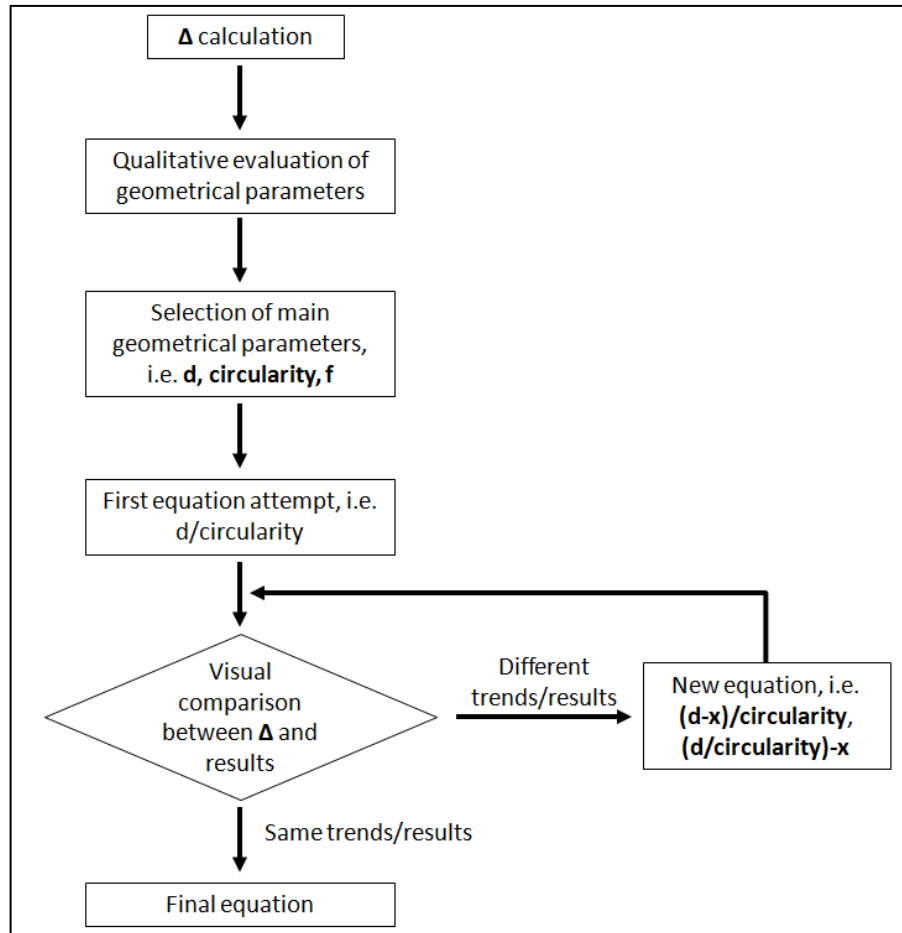


Figure 6.4 – Sequence of operations for obtaining a numerical definition of parameter s.

Parameter s was defined differently depending on feature shape (rounded or grooved shape).

For **rounded micro features**, the parameter of surface s was defined as follows:

$$s = \left[ \left( \frac{d}{\text{circularity}} \right) - 4.7 \right] \cdot 0.045 \quad (14)$$

Surface parameter s is linear dependent to features **depth** d (express in  $\mu\text{m}$ ) and inverse proportional to **circularity index** of surface micro irregularities. These two parameters (d and circularity) seemed to be the main factors influencing friction behaviour of rounded features, as shown previously. For the results selected, features width seemed not to be crucial for tribological response, since dimples presented friction reduction even if they are wider than mean dimensions of large porosity in samples that presented detrimental behaviour (LP and IP), see Table 6.2. It is however noteworthy that features width was selected to be much smaller than

contact diameter (around 170  $\mu\text{m}$ ) in all the tribological tests. Table 6.2 summarizes geometrical dimensions of rounded features and parameters  $\Delta$  and  $s$  expressed in percentage for the selected results.

Table 6.2 – Geometrical characteristics of rounded micro features presented in Figure 6.2. Average values of width were considered for surface pores in sintered material (LP, IP, SP).

	<b>Rounded micro cavities</b>			
	LP	IP	SP	D
<b>Depth (<math>\mu\text{m}</math>)</b>	<b>4*</b>	<b>3*</b>	<b>1.5*</b>	<b>0.5</b>
Width ( $\mu\text{m}$ )	8	6	3	15
R (d/w)	0.5	0.5	0.5	0.03
<b>Circularity</b>	<b>0.5</b>	<b>0.6</b>	<b>0.75</b>	<b>1</b>
<b>Delta <math>\Delta</math> (%)</b>	16%	3%	– 12%	– 19%
<b>Surface parameter <math>s</math> (%)</b>	15%	1%	– 12%	– 19%

\*estimated value

For **grooved shape micro features**, the parameter of surface  $s$  was defined as follows:

$$s = \left( \frac{d - 0.4}{0.29} \right) \cdot f \quad (15)$$

Surface parameter  $s$  is linear dependent to features **depth  $d$**  (express in  $\mu\text{m}$ ) and to **area coverage** of surface micro irregularities  $f$ . The parameter  $d$  was the main factor influencing friction behaviour of rounded features, as shown previously, whereas the coverage area  $f$  could potentially maximize tribological results as reported by [120]. Results of  $\Delta$  and  $s$  values and grooved features geometrical characteristics are collected in Table 6.3.

Table 6.3 – Geometrical characteristics of grooved shape micro features presented in Figure 6.2. Average values of width were considered for surface pores in sintered material (LP, IP, SP).

	<b>Groove shape micro cavities</b>	
	SG	DG
<b>Depth (<math>\mu\text{m}</math>)</b>	<b>0.35</b>	<b>1.35</b>
Width ( $\mu\text{m}$ )	25	20
R (d/w)	0.01	0.07
f (%)	12.5%	10%
<b>Delta <math>\Delta</math> (%)</b>	– 3%	33%
<b>Surface parameter <math>s</math> (%)</b>	– 2%	33%

Note that delta  $\Delta$  values was calculated from Equation (13) using experimental results, whilst surface parameters  $s$  were derived analytically from equation (14) and (15) respectively for rounded and grooved shape features.

The friction response of surface features could be expressed as a function of NP material experimental response using surface parameter  $s$ .  $COF_{NP}$  was used as reference bench and for each speed  $COF_{features}$  was calculated using the proper parameter  $s$  depending on surface conditions (type of cavities, dimensions and morphology). The friction response of surface with micro cavities could be expressed analytically by the following equation:

$$COF'_{features} = (1+s) \cdot COF_{NP} \quad (16)$$

Where the apex ' indicates values calculated through the analytical model, whereas  $COF$  without apex is related to experimental results. Figure 6.5 shows friction response of experimental (solid round markers) and analytical results (solid lines) of samples with surface features. In the same graph, experimental results of NP material were plotted using a solid black line. For all cases, the model proposed seemed to approximate correctly the general friction trend.

Note that this phenomenological model was developed considering just some principal results and main geometrical characteristics of features. The analysis should be extended to all test conditions (varying SRR and  $U_e$ ), also considering all geometrical feature parameters ( $R$ , circularity index, shape, directionality, area coverage). Furthermore, the  $s$  parameter was proposed here as an average value for a certain speed range, however all speeds should be considered.

This phenomenological model aimed at inspiring future works, using a more complete statistical and analytical approach.

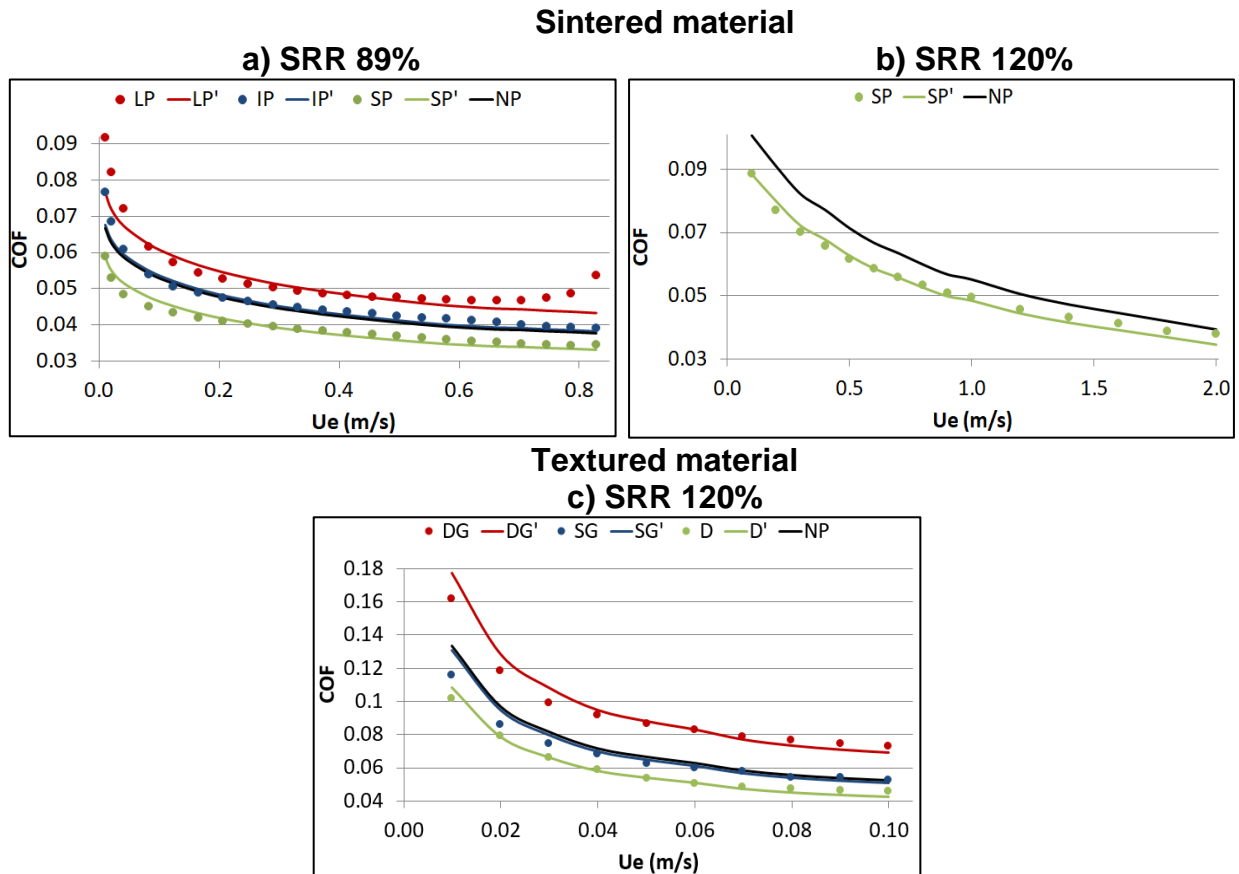


Figure 6.5 – Coefficient of friction results vs entrainment speeds ( $U_e$ ) for sintered (a) and (b) and textured material (c). Dashed markers represent experimental results of surface features, where the apex ' is related to the analytical response.

### 6.3 Conclusions and final remarks of the chapter

General tribological results of sintered and textured materials were organized and map in this chapter. Furthermore, some principal results were selected and a surface parameter  $s$  was proposed to obtain feature friction response from standard reference material. From that, the following conclusions could be drawn:

- Features depth and morphology seemed to be the principal parameters to be considered, being that rounded configurations (SM and D) performed better than irregular ones (IP and LP) and grooves ones (SG and DG). Shallow configurations reduced friction both for rounded and grooves shapes;
- Pores effect on frictional response can be compared to textured dimples, however only small and regular shape features could bring beneficial results. Dimples and pores presenting friction reduction also present very similar geometrical conditions;

- Friction behaviour of modified surfaces (with micro irregularities) was obtained from standard material response (smooth) using a surface parameter. This parameter should include all geometrical and morphological characteristics of surface features. The use of an analytical model could help researchers to design new surface configurations.

## **Chapter 7      Conclusions and future works**

### **7.1 Main conclusions**

In this experimentally thesis the aspects surrounding the tribological behaviour of surface micro cavities were explored during lubricated tests varying sliding-rolling conditions. Firstly, a significant amount of time was invested for manufacturing samples with different surface characteristics both for texturing and sintering processes. Standard dimensions were required for tribological tests, therefore specific procedures were developed. After that, several experimental test conditions using different tribometers were carried out to explore a wide range of operational conditions and parameters. Moreover, a novel technique for measuring film thickness of rough surfaces was applied for the first time on textured and sintered materials.

Specific conclusions were presented in the final part of each chapter, therefore some general remarks are reported here addressing the research questions stated in the text beginning:

#### **1) How porosity characteristics in PM can be precisely controlled and designed?**

Porosity is influenced by powder particles characteristics (mechanical properties, size and morphology) and sintering parameters (temperature, time and pressure). In this study only sintering parameters were varied using different sintering technique. Generally, the increase of sintering temperature and compacting pressure reduced total porosity and led to small pores with rounded shape. However, surface pores are randomly distributed and only general pore characteristics could be controlled.

#### **2) Can surface texture and porosity be compared in terms of geometrical characteristics and tribological performance? If so, which parameter can be used?**

Small porosity configuration and texture dimples can be easily compared due to similar shape and dimensional characteristics. Note that these porosity configurations were achieved using a non-conventional sintering technique

(SPS, disks D10) or by mechanical surface modification after the conventional process (machining, balls B8). Size, shape (circularity index) and coverage area parameters were used to compare different features.

**3) Do the pore size and morphology distribution influence the tribological behaviour in PM material? If so, which characteristics can improve tribological performances for non-conformal contacts?**

Tribological behaviour of PM material is strongly influenced by total porosity and pores characteristics. For the experimental conditions studied, the increase of porosity, pore size and irregular shape led to friction increment. This behaviour was probably due to insufficient film built-in close to large and irregular pores, consequently increasing asperities contact and friction. Small porosity on the contrary seemed to increase load support capacity, presenting micro bearing effects. Besides presenting best tribological performance between PM materials, less porous samples also decreased friction compared to reference smooth surfaces. These findings corroborate to the hypothesis of small surface pores micro bearing effects.

**4) In which tests conditions surface micro irregularities (texture and porosity) improve tribological performance?**

The surface micro irregularities designed in this study improved frictional performance especially in mixed and boundary lubrication (low entrainment speeds), generally presenting micro bearing effects and improving lubricant load support capacity. No significant effects were detected during full film conditions.

**5) Can surface porosity in PM materials lead to similar tribological effects of surface texture? If so, how results can be mapped and categorized as to produce a comprehensive phenomenological model?**

Surface pores could potentially bring to similar results of textured surfaces, especially considering similar geometrical and morphological configurations (dimples and rounded pores). However, successful PM configurations were achieved using non-conventional sintering techniques (SPS) or additional

machining process, causing cost increment. The utilization of PM material in real application for improving tribological performance should consider these additional costs. To conclude dimples and small porosity led to friction reduction, however both require additional operations or non-conventional manufacturing techniques.

Results were mapped based on geometrical characteristics of surface features, tribological results and test conditions for giving a comprehensive outcome of the experimental test developed.

**6) Is it possible to predict the friction response of surface with micro cavities from results of reference material using analytic tools?**

A surface parameter  $s$  was introduced for this purpose. The parameter was obtained from geometrical features characteristics and frictional behaviour of some selected configurations. This methodology could help in better understanding friction response of surface modification and even predict behaviours if correctly validated.

## **7.2 Contributions**

From a fundamental point of view, this thesis has contributed to understand how randomly distributed and tailored micro irregularities could change lubricant conditions, potentially increasing the efficiency of mechanical systems. Experimental tests were developed for textured and sintered surfaces to better scrutinize the effect of surface cavities under lubricated non-conformal contact. Furthermore, a preliminary methodology was proposed to predict friction behaviour of surface irregularities based on reference material response and features characteristics.

From a technological point of view, the sintering process was directly compared to surface texturing to provide superior tribological performances with reduced manufacturing costs. The work supported the exploration of the use of sintering in large scale manufacturing processes, aimed at reducing production costs.

Another contribution is to obtain PM materials with a controlled porosity leading to specific surface conditions with features similar to those obtained applying micro

cavities using conventional texturing techniques. Furthermore, the use of PM to manufacture both disks and balls and the applications of laser texture on balls for tribological tests is itself novel due to the added complexity in manufacturing balls within the tolerance required for the experimental tests.

Generally, this research helped increasing the understanding on surface modification and its tribological effects. For instance, papers, conference participations and collaborations with international recognized research groups stressed the goals achieved during this study.

### 7.3 Future work suggestions

In order to build on the understanding obtained in this study, several future work suggestions could be made:

- Perform experimental tests with different dimples configurations (varying width and depth) to obtain a more complete phenomenal behaviour;
- Design perpendicular grooves with reduced transversal dimensions for increase lubricant load support capacity;
- Improve the phenomenological model by considering the entire data generated from the experimental tests and surface conditions studies. Obtain a surface parameter dependent on more geometrical parameters, considering operational conditions and varying accordingly to a non-dimensional number, i.e.:

$$s = f(H_s, SRR, \Lambda, \text{circularity}, R, f)$$

Machine learning methods are suggested to analyse not only these experimental results but also results from literature to generate a complete and reliable predictive model.

- Utilize simulation tools for improving the design of surface texture configurations;
- Scrutinize the evolution of wear performance in PM materials. Porosity could be still present after wear tests (bulk porosity), differently from shallow surface texture.

## Bibliography

- [1] R.S. S.P.A. Wennber, J.L.; von Turkovich, B.F.; Roubik J.R.; Boulger, F.W.; Hahn, Review of Metal Processing Literature, *J. Engineering Ind.* (1965) 85–96.
- [2] D.B. Hamilton, J.A. Walowit, C.M. Allen, A Theory of Lubrication by Micro-irregularities, *J. Basic Eng.* 88 (1966) 177–185. doi:10.1017/CBO9781107415324.004.
- [3] K. Holmberg, P. Andersson, A. Erdemir, Global energy consumption due to friction in passenger cars, *Tribol. Int.* 47 (2012) 221–234. doi:10.1016/j.triboint.2011.11.022.
- [4] D. Gropper, L. Wang, T.J. Harvey, Hydrodynamic lubrication of textured surfaces: A review of modeling techniques and key findings, *Tribol. Int.* 94 (2016) 509–529. doi:10.1016/j.triboint.2015.10.009.
- [5] S.C. Vlădescu, A. V. Olver, I.G. Pegg, T. Reddyhoff, The effects of surface texture in reciprocating contacts - An experimental study, *Tribol. Int.* 82 (2015) 28–42. doi:10.1016/j.triboint.2014.09.015.
- [6] A. Kovalchenko, O. Ajayi, A. Erdemir, G. Fenske, I. Etsion, The Effect of Laser Texturing of Steel Surfaces and Speed-Load Parameters on the Transition of Lubrication Regime from Boundary to Hydrodynamic, *Tribol. Trans.* 47 (2004) 299–307. doi:10.1080/05698190490440902.
- [7] A. Kovalchenko, O. Ajayi, A. Erdemir, G. Fenske, I. Etsion, The effect of laser surface texturing on transitions in lubrication regimes during unidirectional sliding contact, *Tribol. Int.* 38 (2005) 219–225. doi:10.1016/j.triboint.2004.08.004.
- [8] U. Pettersson, S. Jacobson, Influence of surface texture on boundary lubricated sliding contacts, *Tribol. Int.* 36 (2003) 857–864. doi:10.1016/S0301-679X(03)00104-X.
- [9] C. Gachot, A. Rosenkranz, S.M. Hsu, H.L. Costa, A critical assessment of surface texturing for friction and wear improvement, *Wear.* 372–373 (2017) 21–41. doi:10.1016/j.wear.2016.11.020.
- [10] U. Sudeep, N. Tandon, R.K. Pandey, Performance of Lubricated Rolling/Sliding Concentrated Contacts With Surface Textures: A Review, *J. Tribol.* 137 (2015) 031501. doi:10.1115/1.4029770.
- [11] S. Carabajar, C. Verdu, A. Hamel, R. Fougères, Fatigue behaviour of a nickel alloyed sintered steel, *Mater. Sci. Eng. A.* 257 (1998) 225–234. doi:10.1016/S0921-5093(98)00846-6.
- [12] S. Carabajar, C. Verdu, R. Fougères, Damage mechanisms of a nickel alloyed sintered steel during tensile tests, *Mater. Sci. Eng. A.* 232 (1997) 80–87. doi:10.1016/S0921-5093(97)00100-7.

- [13] G. Straffelini, A. Molinari, H. Danninger, Impact notch toughness of high-strength porous steels, *Mater. Sci. Eng. A.* 272 (1999) 300–309. doi:10.1016/S0921-5093(99)00491-8.
- [14] G. Straffelini, V. Fontanari, A. Molinari, True and apparent Young's modulus in ferrous porous alloys, *Mater. Sci. Eng. A.* 260 (1999) 197–202. doi:10.1016/S0921-5093(98)00960-5.
- [15] F. Martin, C. García, Y. Blanco, Influence of residual porosity on the dry and lubricated sliding wear of a powder metallurgy austenitic stainless steel, *Wear.* 328–329 (2015) 1–7. doi:10.1016/j.wear.2015.01.025.
- [16] X. Li, U. Olofsson, A study on friction and wear reduction due to porosity in powder metallurgic gear materials, *Tribol. Int.* 110 (2017) 86–95. doi:10.1016/j.triboint.2017.02.008.
- [17] X. Li, M. Sosa, U. Olofsson, A pin-on-disc study of the tribology characteristics of sintered versus standard steel gear materials, *Wear.* 340–341 (2014) 31–40. doi:10.1016/j.wear.2015.01.032.
- [18] G. Boidi, I.S. Tertuliano, F.J. Profito, W. de Rossi, I.F. Machado, Effect of laser surface texturing on friction behaviour in elastohydrodynamically lubricated point contacts under different sliding-rolling conditions, *Tribol. Int.* (2019). doi:10.1016/j.triboint.2019.02.021.
- [19] G. Boidi, N.K. Fukumasu, I.F. Machado, Wear and friction performance under lubricated reciprocating tests of steel powder mixtures sintered by Spark Plasma Sintering, *Tribol. Int.* 121 (2018). doi:10.1016/j.triboint.2018.01.032.
- [20] G. Boidi, I.S. Tertuliano, I.F. Machado, Tribological effect of porosity in sintered steel varying sliding/rolling conditions, in: *Nord. 2018*, 2018: pp. 7–8.
- [21] G. Boidi, I.S. Tertuliano, L.G.B.S. Lima, F.J. Profito, I.F. Machado, Porosity effect of sintered steel on the frictional performance of conformal and non-conformal lubricated contacts, *Accept. Publ. Tribol. Trans.* Accepted f (2019). doi:10.1080/10402004.2019.1640917.
- [22] N.K. Fukumasu, G. Boidi, V. Seriacopi, G.A.A. Machado, R.M. Souza, I.F. Machado, Numerical analyses of stress induced damage during a reciprocating lubricated test of FeCMo SPS sintered alloy, *Tribol. Int.* 113 (2017). doi:10.1016/j.triboint.2016.12.025.
- [23] G. Boidi, I.S. Tertuliano, M.F. Cano, G.A.A. Machado, R.M. Souza, I.F. Machado, Tribological evaluation of sintered and conventional gear materials, *SAE Int.* 36 (2017) 1–9. doi:10.4271/2017-36-0153.
- [24] A. Upadhyaya, G.S. Upadhyaya, *Powder Metallurgy: Science, Technology and Materials*, First edit, Great Noida, India, 2011.
- [25] G. Boidi, *Sistemi sinterizzati a base Ferro a elevata resistenza ad impatto*, Bacherol's thesiso, Politecnico di Torino, Italia, 2012.
- [26] R.M. German, *Sintering Theory and Practice*, Ed. John Wiley and Sons, 1996.
- [27] ASM Handbook Committee, *Powder Metal Technologies and Applications*,

1998.

- [28] R.M. German, Coarsening in sintering: Grain shape distribution, grain size distribution, and grain growth kinetics in solid-pore systems, *Crit. Rev. Solid State Mater. Sci.* 35 (2010) 263–305. doi:10.1080/10408436.2010.525197.
- [29] R. Orrù, R. Licheri, A.M. Locci, A. Cincotti, G. Cao, Consolidation/synthesis of materials by electric current activated/assisted sintering, *Mater. Sci. Eng. R Reports.* 63 (2009) 127–287. doi:10.1016/j.mser.2008.09.003.
- [30] W. Chen, U. Anselmi-Tamburini, J.E. Garay, J.R. Groza, Z.A. Munir, Fundamental investigations on the spark plasma sintering/synthesis process, *Mater. Sci. Eng. A.* 407 (2005) 24–30. doi:10.1016/j.msea.2005.06.066.
- [31] F. Balima, A. Largeteau, Phase transformation of alumina induced by high pressure spark plasma sintering (HP-SPS), *Scr. Mater.* 158 (2019) 20–23. doi:10.1016/j.scriptamat.2018.08.016.
- [32] L. Fu, C. Wu, K. Grandfield, E. Unosson, J. Chang, H. Engqvist, W. Xia, Transparent single crystalline ZrO<sub>2</sub>-SiO<sub>2</sub> glass nanoceramic sintered by SPS, *J. Eur. Ceram. Soc.* 36 (2016) 3487–3494. doi:10.1016/j.jeurceramsoc.2016.05.016.
- [33] C.J. Xuan, Z. Zhao, P.G. Jönsson, Wettability and corrosion of spark plasma sintered (SPS) ZrN by liquid iron and steel, *J. Eur. Ceram. Soc.* 36 (2016) 2435–2442. doi:10.1016/j.jeurceramsoc.2016.03.006.
- [34] K. Zarebski, P. Putyra, Iron powder-based graded products sintered by conventional method and by SPS, *Adv. Powder Technol.* 26 (2015) 401–408. doi:10.1016/j.apt.2014.11.010.
- [35] G.D. Zhan, J. Kuntz, J. Wan, J. Garay, A.K. Mukherjee, A novel processing route to develop a dense nanocrystalline alumina matrix (< 100 nm) nanocomposite material, *J. Am. Ceram. Soc.* 86 (2003) 200–202. doi:10.1111/j.1151-2916.2003.tb03306.x.
- [36] M. Omori, Sintering, consolidation, reaction and crystal growth by the spark plasma system (SPS), *Mater. Sci. Eng. A.* 287 (2000) 183–188. doi:10.1016/S0921-5093(00)00773-5.
- [37] W. Li, L. Gao, Fabrication of HAp – ZrO<sub>2</sub> ( 3Y ) nano-composite by SPS, 24 (2003) 937–940.
- [38] M.W. Barsoum, *Fundamentals of ceramics*, The Mc Graw-Hill companies Inc., 2003.
- [39] W.D. Chiang, Y. M., Birnie, D. P., Kingery, *Physical Ceramics Principles for Ceramic Science and Engineering*, John Wiley & Sons, Inc., 1997.
- [40] A. Spencer, *Optimizing Surface Texture for Combustion Engine Cylinder Liners*, Lulea University of Technology, 2010.
- [41] I. Etsion, G. Halperin, V. Brizmer, Y. Kligerman, Experimental investigation of laser surface textured parallel thrust bearings, *Tribol. Lett.* 17 (2004) 295–300. doi:10.1023/B:TRIL.0000032467.88800.59.

- [42] I. Etsion, G. Halperin, A laser surface textured hydrostatic mechanical seal, *Tribol. Trans.* 45 (2002) 430–434. doi:10.1080/10402000208982570.
- [43] A. Ahmed, H.H. Masjuki, M. Varman, M.A. Kalam, M. Habibullah, K.A.H. Al Mahmud, An overview of geometrical parameters of surface texturing for piston/cylinder assembly and mechanical seals, *Meccanica.* 51 (2016) 9–23. doi:10.1007/s11012-015-0180-6.
- [44] I. Etsion, Y. Kligerman, G. Halperin, Analytical and experimental investigation of laser-textured mechanical seal faces, *Tribol. Trans.* 42 (1999) 511–516. doi:10.1080/10402009908982248.
- [45] V. Brizmer, Y. Kligerman, I. Etsion, A laser surface textured parallel thrust bearing, *Tribol. Trans.* 46 (2003) 397–403. doi:10.1080/10402000308982643.
- [46] B.J. Hamrock, S.R. Schmid, *Fundamental of Fluid Film Lubrication*, Second Edi, 2004.
- [47] J.H. Daniel, D.F. Moore, J.F. Walker, Focused ion beams and silicon-on-insulator - a novel approach to MEMS, *Smart Mater. Struct.* 9 (2000) 284–290. doi:10.1088/0964-1726/9/3/306.
- [48] L. Mourier, D. Mazuyer, A.A. Lubrecht, C. Donnet, Transient increase of film thickness in micro-textured EHL contacts, *Tribol. Int.* 39 (2006) 1745–1756. doi:10.1016/j.triboint.2006.02.037.
- [49] A.F. Lasagni, C. Gachot, K.E. Trinh, M. Hans, A. Rosenkranz, T. Roch, S. Eckhardt, T. Kunze, M. Bieda, D. Günther, V. Lang, F. Mücklich, Direct laser interference patterning, 20 years of development: from the basics to industrial applications, *Laser-Based Micro- Nanoprocessing XI.* 10092 (2017) 1009211. doi:10.1117/12.2252595.
- [50] L. Nánai, Z.I. Benkő, R.R. Letfullin, T.F. George, *Laser-Matter Interactions: Nanostructures, Fabrication and Characterization* University of Szeged, in: n.d.: pp. 1–36.
- [51] B.M. Duarte, A. Lasagni, R. Giovanelli, J. Narciso, E. Louis, F. Mücklich, Increasing Lubricant Film Lifetime by Grooving Periodical Patterns Using Laser Interference Metallurgy, *Adv. Eng. Mater.* 10 (2008) 554–558. doi:10.1002/adem.200700321.
- [52] P.G. Grützmacher, A. Rosenkranz, C. Gachot, How to guide lubricants - Tailored laser surface patterns on stainless steel, *Appl. Surf. Sci.* 370 (2016) 59–66. doi:10.1016/j.apsusc.2016.02.115.
- [53] A. Lasagni, C. Holzapfel, T. Weirich, F. Mücklich, Laser interference metallurgy: A new method for periodic surface microstructure design on multilayered metallic thin films, *Appl. Surf. Sci.* 253 (2007) 8070–8074. doi:10.1016/j.apsusc.2007.02.092.
- [54] A. Rosenkranz, S. Fleischmann, C. Gachot, F. Mücklich, Anisotropic Spreading Behavior of PAO Oil on Laser-Patterned Stainless Steel Surfaces, *Adv. Eng. Mater.* 17 (2015) 1645–1651. doi:10.1002/adem.201500115.

- [55] A. Lasagni, M. D'Alessandria, R. Giovanelli, F. Mücklich, Advanced design of periodical architectures in bulk metals by means of Laser Interference Metallurgy, *Appl. Surf. Sci.* 254 (2007) 930–936. doi:10.1016/j.apsusc.2007.08.010.
- [56] IPEN- Laboratórios CLA, IPEN- Laboratórios CLA, (2019). [https://www.ipen.br/portal\\_por/portal/interna.php?secao\\_id=589&campo=1785](https://www.ipen.br/portal_por/portal/interna.php?secao_id=589&campo=1785).
- [57] Saarland University Functional Materials, Saarland University\_2019.pdf, (2019). <https://www.fuwe.uni-saarland.de/institutsleitung/?lang=en>.
- [58] H. Kasem, O. Stav, P. Grützmacher, C. Gachot, Effect of Low Depth Surface Texturing on Friction Reduction in Lubricated Sliding Contact, *Lubricants*. 6 (2018) 62. doi:10.3390/lubricants6030062.
- [59] Anton-Paar, Anton-Paar, (2019). <https://www.anton-paar.com/corp-en/products/details/svm-2001/>.
- [60] X. Li, U. Olofsson, E. Bergseth, Pin-on-Disc Study of Tribological Performance of Standard and Sintered Gear Materials Treated with Triboconditioning Process: Pretreatment by Pressure-Induced Tribofilm Formation, *Tribol. Trans.* 60 (2017) 47–57. doi:10.1080/10402004.2016.1146379.
- [61] M. Dlapka, H. Danninger, C. Gierl, B. Lindqvist, Defining the pores in PM components, *Met. Powder Rep.* 65 (2010) 30–33. doi:10.1016/S0026-0657(10)70093-X.
- [62] A.F. Padilha, F.F. Ambrozio, *Técnicas de análise microestrutural*, São Paulo, 1985.
- [63] Seville J.P.K.;, C.Y. Wu, *Particle Technology and Engineering: an Engineer's Guide to Particles and Powders: Fundamentals and Computational Approaches*, 2016.
- [64] N. Kurgan, Effect of porosity and density on the mechanical and microstructural properties of sintered 316L stainless steel implant materials, *Mater. Des.* 55 (2014) 235–241. doi:10.1016/j.matdes.2013.09.058.
- [65] A. V. Manoylov, F.M. Borodich, H.P. Evans, Modelling of elastic properties of sintered porous materials, *Proc. R. Soc. A Math. Phys. Eng. Sci.* 469 (2013) 20120689–20120689. doi:10.1098/rspa.2012.0689.
- [66] N. Chawla, X. Deng, Microstructure and mechanical behavior of porous sintered steels, *Mater. Sci. Eng. A.* 390 (2005) 98–112. doi:10.1016/j.msea.2004.08.046.
- [67] M.S. Koval'chenko, Mechanical properties of sintered materials, 3 (1991) 257–261.
- [68] J.P. Panakkal, H. Willems, W. Arnold, Nondestructive evaluation of elastic parameters of sintered iron powder compacts, *J. Mater. Sci.* 25 (1990) 1397–1402. doi:10.1007/BF00585456.
- [69] J.A. Greenwood, J.B.P. Williamson, Contact of nominally flat surfaces, *Proc. R. Soc. London.* (1966) 300–319.

- [70] B. Bhushan, Principles and Applications of Tribology, 2013. doi:10.1115/1.3452952.
- [71] W. Grabon, P. Pawlus, S. Wos, W. Koszela, M. Wieczorowski, Effects of cylinder liner surface topography on friction and wear of liner-ring system at low temperature, Tribol. Int. 121 (2018) 148–160. doi:10.1016/j.triboint.2018.01.050.
- [72] R. Reizer, P. Pawlus, 3D surface topography of cylinder liner forecasting during plateau honing process, J. Phys. Conf. Ser. 311 (2011). doi:10.1088/1742-6596/311/1/012021.
- [73] W. Grabon, P. Pawlus, S. Wos, W. Koszela, M. Wieczorowski, Effects of honed cylinder liner surface texture on tribological properties of piston ring-liner assembly in short time tests, Tribol. Int. 113 (2017) 137–148. doi:10.1016/j.triboint.2016.11.025.
- [74] PCS Instruments, PCS Instruments London, (2019). <https://pcs-instruments.com/>.
- [75] B.J. Hamrock, D. Dowson, Isothermal Elastohydrodynamic Lubrication of Point Contacts: Part III—Fully Flooded Results, J. Lubr. Technol. 99 (1977) 264–275. doi:10.1115/1.3453074.
- [76] J. Echávarri Otero, P. Lafont Morgado, E. Chacón Tanarro, E. De La Guerra Ochoa, A. Díaz Lantada, J.M. Muñoz-Guijosa, J.L. Muñoz Sanz, Analytical model for predicting the friction coefficient in point contacts with thermal elastohydrodynamic lubrication, Proc. Inst. Mech. Eng. Part J J. Eng. Tribol. 225 (2011) 181–191. doi:10.1177/1350650111398848.
- [77] J.E. Otero, E. de la G. Ochoa, E.C. Tanarro, A.D. Lantada, J.M. Muñoz-Guijosa, Analytical model for predicting friction in line contacts, Lubr. Sci. 28 (2016) 189–205. doi:DOI: 10.1002/ls.1325.
- [78] M. Masjedi, M.M. Khonsari, Tribology International On the effect of surface roughness in point-contact EHL : Formulas for film thickness and asperity load, Tribology Int. 82 (2015) 228–244. doi:10.1016/j.triboint.2014.09.010.
- [79] G.J. Johnston, R. Wayte, H.A. Spikes, The measurement and study of very thin lubricant films in concentrated contacts, Tribol. Trans. 34 (1991) 187–194. doi:10.1080/10402009108982026.
- [80] P.M. Cann, H.A. Spikes, J. Hutchinson, The development of a spacer layer imaging method (slim) for mapping elastohydrodynamic contacts, Tribol. Trans. 39 (1996) 915–921. doi:10.1080/10402009608983612.
- [81] J. Luo, S. Wen, P. Huang, Thin film lubrication. Part I. Study on the transition between EHL and thin film lubrication using a relative optical interference intensity technique, Wear. 194 (1996) 107–115. doi:10.1016/0043-1648(95)06799-X.
- [82] R.S. Heemskerk, K.N. Vermeiren, H. Dolfsma, Measurement of lubrication condition in rolling element bearings, ASLE Trans. 25 (1982) 519–527. doi:10.1080/05698198208983121.

- [83] T. Reddyhoff, J.H. Choo, H.A. Spikes, R.P. Glovnea, Lubricant flow in an elasto-hydrodynamic contact using fluorescence, *Tribol. Lett.* 38 (2010) 207–215. doi:10.1007/s11249-010-9592-6.
- [84] T. Reddyhoff, R. Dwyer-Joyce, P. Harper, Ultrasonic measurement of film thickness in mechanical seals, *Seal. Technol.* 2006 (2006) 7–11. doi:10.1016/S1350-4789(06)71260-0.
- [85] Y. Qui, M.M. Khonsari, On the Prediction of Cavitation in Dimples Using a Mass-Conservative Algorithm, *J. Tribol.* 131 (2009). doi:10.1115/1.3176994.
- [86] S.C. Vlădescu, A. V. Olver, I.G. Pegg, T. Reddyhoff, Combined friction and wear reduction in a reciprocating contact through laser surface texturing, *Wear.* 358–359 (2016) 51–61. doi:10.1016/j.wear.2016.03.035.
- [87] F.J. Profito, S.C. Vlădescu, T. Reddyhoff, D. Dini, Transient experimental and modelling studies of laser-textured micro-grooved surfaces with a focus on piston-ring cylinder liner contacts, *Tribol. Int.* 113 (2017) 125–136. doi:10.1016/j.triboint.2016.12.003.
- [88] M. Fowell, A. V. Olver, A.D. Gosman, H.A. Spikes, I. Pegg, Entrainment and inlet suction: Two mechanisms of hydrodynamic lubrication in textured bearings, *J. Tribol.* 129 (2007) 336–347. doi:10.1115/1.2540089.
- [89] A. V. Olver, M.T. Fowell, H.A. Spikes, I.G. Pegg, “Inlet suction”, a load support mechanism in non-convergent, pocketed, hydrodynamic bearings, *Proc. Inst. Mech. Eng. Part J J. Eng. Tribol.* 220 (2006) 105–108. doi:10.1243/13506501JET168.
- [90] J. Graham, H. Spikes, S. Korcek, The Friction Reducing Properties of Molybdenum Dialkyldithiocarbamate Additives: Part I — Factors Influencing Friction Reduction, *Tribol. Trans.* 44 (2001) 626–636. doi:10.1080/10402000108982504.
- [91] J.S.R. Acero, Influência do acabamento superficial no desempenho de lubrificantes de motor novos e usados em automóveis abastecidos com E22 e E100, Master Thesis, Escola Politécnica da Universidade de São Paulo - EPUSP, São Paulo, Brazil, 2015.
- [92] L. Sabri, S. Mezghani, M. El Mansori, H. Zahouani, Multiscale study of finish-honing process in mass production of cylinder liner, 271 (2011) 509–513. doi:10.1016/j.wear.2010.03.026.
- [93] K.D. Lawrence, B. Ramamoorthy, Multi-surface topography targeted plateau honing for the processing of cylinder liner surfaces of automotive engines, *Appl. Surf. Sci.* 365 (2016) 19–30. doi:10.1016/j.apsusc.2015.12.245.
- [94] J. Schmid, Large Engine Cylinder Honing as a Contribution to Emission reduction, *MTZ Ind.* 3 (2013) 48–53.
- [95] X.. Wang, H.. Zhang, S.M. Hsu, The Effects of dimple size and depth on friction reduction under boundary lubrication pressure, (2007) 24–26.
- [96] A. Rosenkranz, T. Heib, C. Gachot, F. Mücklich, Oil film lifetime and wear

- particle analysis of laser-patterned stainless steel surfaces, *Wear*. 334–335 (2015) 1–12. doi:10.1016/j.wear.2015.04.006.
- [97] D. Braun, C. Greiner, J. Schneider, P. Gumbsch, Efficiency of laser surface texturing in the reduction of friction under mixed lubrication, *Tribol. Int.* 77 (2014) 142–147. doi:10.1016/j.triboint.2014.04.012.
- [98] H. Yu, X. Wang, F. Zhou, Geometric shape effects of surface texture on the generation of hydrodynamic pressure between conformal contacting surfaces, *Tribol. Lett.* 37 (2010) 123–130. doi:10.1007/s11249-009-9497-4.
- [99] I. Etsion, L. Burstein, A model for mechanical seals with regular microsurface structure, *Tribol. Trans.* 39 (1996) 677–683. doi:10.1080/10402009608983582.
- [100] A. Borghi, E. Gualtieri, D. Marchetto, L. Moretti, S. Valeri, Tribological effects of surface texturing on nitriding steel for high-performance engine applications, *Wear*. 265 (2008) 1046–1051. doi:10.1016/j.wear.2008.02.011.
- [101] A. Kovalchenko, O. Ajayi, A. Erdemir, G. Fenske, Friction and wear behavior of laser textured surface under lubricated initial point contact, *Wear*. 271 (2011) 1719–1725. doi:10.1016/j.wear.2010.12.049.
- [102] J.W. Choo, R.P. Glovnea, A. V. Olver, H. a. Spikes, The Effects of Three-Dimensional Model Surface Roughness Features on Lubricant Film Thickness in EHL Contacts, *J. Tribol.* 125 (2003) 533. doi:10.1115/1.1538617.
- [103] L. Gao, G. De Boer, R. Hewson, The role of micro-cavitation on EHL: A study using a multiscale mass conserving approach, *Tribol. Int.* 90 (2015) 324–331. doi:10.1016/j.triboint.2015.04.005.
- [104] S. Janakiraman, P. Klit, N.S. Jensen, J. Gronbaek, Observations on the effects of grooved surfaces on the interfacial torque in highly loaded rolling and sliding tests, *Tribol. Int.* 81 (2015) 179–189. doi:10.1016/j.triboint.2014.08.015.
- [105] A. Rosenkranz, A. Szurdak, C. Gachot, G. Hirt, F. Mücklich, Friction reduction under mixed and full film EHL induced by hot micro-coined surface patterns, *Tribol. Int.* 95 (2016) 290–297. doi:10.1016/j.triboint.2015.11.035.
- [106] J. Guegan, A. Kadiric, H. Spikes, A Study of the Lubrication of EHL Point Contact in the Presence of Longitudinal Roughness, *Tribol. Lett.* 59 (2015) 1–18. doi:10.1007/s11249-015-0549-7.
- [107] J. Guegan, A. Kadiric, A. Gabelli, H. Spikes, The Relationship Between Friction and Film Thickness in EHD Point Contacts in the Presence of Longitudinal Roughness, *Tribol. Lett.* 64 (2016) 1–15. doi:10.1007/s11249-016-0768-6.
- [108] J. Guegan, Experimental Investigation into the Influence of Roughness on Friction and Film Thickness in EHD Contacts, Doctoral Thesis, Imperial College London, 2015.
- [109] A. Kadiric, P. Rycerz, Influence of Contact Conditions on the Onset of Micropitting in Rolling-Sliding Contacts Pertinent to Gear Applications, AGMA Tech. Pap. (2016).
- [110] A. Cameron, R. Gohar, Theoretical and Experimental Studies of the Oil Film in

- Lubricated Point Contact, Proc. R. Soc. London. (1966) 520–536.
- [111] I. Krupka, M. Hartl, M. Zimmerman, P. Houska, S. Jang, Effect of surface texturing on elastohydrodynamically lubricated contact under transient speed conditions, Tribol. Int. 44 (2011) 1144–1150. doi:10.1016/j.triboint.2011.05.005.
- [112] N. Kurgan, R. Varol, Mechanical properties of P/M 316L stainless steel materials, Powder Technol. 201 (2010) 242–247. doi:10.1016/j.powtec.2010.03.041.
- [113] M. Ebner, M. Omasta, T. Lohner, P. Šperka, I. Krupka, M. Hartl, K. Michaelis, B.-R. Höhn, K. Stahl, Local Effects in EHL Contacts with Oil-Impregnated Sintered Materials, Lubricants. 7 (2019) 1. doi:10.3390/lubricants7010001.
- [114] M. Ebner, T. Lohner, K. Michaelis, B.-R. Höhn, K. Stahl, Self-lubricating gears with oil-impregnated sintered materials, Forsch. Im Ingenieurwes. 81 (2017) 175–190. doi:10.1007/s10010-017-0227-z.
- [115] A. Gama, T. Cousseau, B. Graça, J. Castro, J. Seabra, Experimental measuring set-up and procedure for traction coefficient on roller-on-disc contact, Lubr. Sci. (2016) 349–362. doi:10.1002/lis.
- [116] G. Pintaude, Introduction of the Ratio of the Hardness to the Reduced Elastic Modulus for Abrasion, Tribol. - Fundam. Adv. (2013) 217–230. doi:10.5772/55470.
- [117] S. Li, U. Parmar, The Effects of Microdimple Texture on the Friction and Thermal Behavior of a Point Contact, J. Tribol. 140 (2018) 041503. doi:10.1115/1.4039228.
- [118] A.F. Shamsul Baharin, M.J. Ghazali, J. A Wahab, Laser surface texturing and its contribution to friction and wear reduction : a brief review, Ind. Lubr. Tribol. 68 (2016) 57–66. doi:10.1108/ILT-05-2015-0067.
- [119] L. Mourier, D. Mazuyer, F.P. Ninove, A.A. Lubrecht, Lubrication mechanisms with laser-surface-textured surfaces in elastohydrodynamic regime, Proc. Inst. Mech. Eng. Part J J. Eng. Tribol. 224 (2010) 697–711. doi:10.1243/13506501JET771.
- [120] A. Codrignani, B. Frohnepfel, F. Magagnato, P. Schreiber, J. Schneider, P. Gumbsch, Numerical and experimental investigation of texture shape and position in the macroscopic contact, Tribol. Int. 122 (2018) 46–57. doi:10.1016/j.triboint.2018.02.001.